

Giacomo Melloni

Characterization of the downlink channel in the UHF band for LEO satellites

Graduate thesis in Digital Infrastructure and Cyber Security

Supervisor: David Palma

Co-supervisor: Roger Birkeland

August 2023

Giacomo Melloni

Characterization of the downlink channel in the UHF band for LEO satellites



Graduate thesis in Digital Infrastructure and Cyber Security
Supervisor: David Palma
Co-supervisor: Roger Birkeland
August 2023

Norwegian University of Science and Technology
Faculty of Information Technology and Electrical Engineering
Dept. of Information Security and Communication Technology



Norwegian University of
Science and Technology

Title: Characterization of the downlink channel in the UHF band for LEO satellites

Student: Melloni, Giacomo

Problem description:

The HYPSONO-2 mission is the follow-up to the HYPSONO-1 satellite, launched in January 2022. In addition to collecting hyperspectral data worldwide, HYPSONO-2 will have on board an SDR used for frequency monitoring, channel measurement and communication experiments (communication between remote sensor systems and the satellite). The SDR platform has been selected and integrated into HYPSONO's software architecture.

The UHF band (300-3000 MHz) is well-suited for satellite communication thanks to its relatively low path attenuation. According to the ITU Radio Regulations Number 5.282, parts of the UHF band are allocated for amateur use. As a heavily utilized band, one important consideration is studying the interference environment. So far no official resources are found for this purpose. Currently, there are studies related to the UHF band and LEO satellites in the uplink channel, but given the non-reciprocity property of the channel, the characteristics of the downlink channel must be considered independent. Other problems related to this band are fading and the multipath effect due to the presence of the Ionosphere. The ionospheric effects will be considered to have an accurate channel model.

This project will focus on mission development and payload operation, with a focus on channel characterisation, including the measurement of interference and the channel between the satellite and ground terminal. In this work, it will be considered a frequency within the band 430-440 MHz. The first problem to be taken into account is the selection of the most relevant channel effects that lead to reducing the quality of the signal. This is an important phase since the complexity and accuracy of the channel model are fundamental variables to weigh. The second problem is how to collect sufficient data for the characterisation of the channel. One of the primary foci of the project is to create an efficient method for gathering measurements, which will be used to compare the channel model with the real one.

Approved on: 2023-03-20

Main supervisor: Palma, David, NTNU

Co-supervisor: Birkeland, Roger, NTNU, Small Satellite Lab

Abstract

Channel characterization plays a vital role in various telecommunication domains, for instance, mobile radio networks and satellite communications. Understanding the behavior of the propagation channel is essential for implementing techniques to mitigate the time and location dependency of the medium on radio waves. This thesis aims at the development of a method for characterizing the Downlink (DL) channel, specifically tailored for Low Earth Orbit (LEO) satellites operating in the Ultra High Frequency (UHF) band. A simulator is designed to accommodate a universal architecture capable of recreating a wide range of scenarios, considering both satellite and ground station equipment. It incorporates various channel entities that can introduce distortion in the electromagnetic field, with a primary focus on the interaction between the transmitted signal and the ionosphere. In addition to the simulator's development, different methods for characterizing channel entities, including the channel sounder technique, are discussed. As expected, the Doppler shift estimation, the channel sounder and the Faraday estimation offer themselves as good methods, validating the implemented channel entities, while the S_4 parameter works under some assumptions. A Hardware-In-the-Loop (HIL) testing phase of these solutions is presented, using a dedicated testbed. The system topology and the implemented components are detailed, along with a general method for the calibration and characterization process of relevant entities. Finally, the analysis is completed by comparing the transmission performance of two Software Defined Radio (SDR) devices included in the testbed, showing that the Universal Software Radio Peripheral (USRP)-2901 outperforms the TOTEM SDR.

Preface

Prima di procedere con l'elaborato, vorrei ringraziare le persone che hanno contribuito alla realizzazione di questa tesi. Prima di tutto, un ringraziamento speciale va al mio relatore e professore David Palma. La ringrazio per la sua disponibilità e per l'aiuto che mi ha dato in questi mesi stupendi. Ringrazio il mio correlatore Roger Birkeland, il quale mi ha inserito nel suo gruppo di ricerca SmallSat lab durante questo periodo. Grazie per avermi dedicato tempo alla realizzazione di questa tesi, soprattutto nei momenti più difficili. Grazie anche al gruppo SmallSat lab per l'aiuto tecnico che mi è stato dato. Ringrazio profondamente il professor Torbjörn Ekman, il quale è stato di fondamentale aiuto nel fornire consigli a livello teorico. Un ringraziamento va anche alla mia famiglia, specialmente Giulia e Tobias, che mi ha supportato in ogni aspetto in questi mesi lontano da loro. Voglio ringraziare tutti i miei amici, soprattutto quelli conosciuti in Norvegia, con i quali ho condiviso i migliori momenti della mia vita. Un ringraziamento speciale va alla persona più importante che ho avuto il piacere di conoscere in Norvegia, Adelaide. Grazie per essermi sempre stata vicino, soprattutto nei momenti difficili.

Infine, un ringraziamento va al me di questi cinque anni. Grazie per non aver mai mollato.

Grazie, grazie, grazie.

Contents

List of Figures	ix
List of Tables	xv
List of Symbols	xvii
List of Acronyms	xix
1 Introduction	1
1.1 The HYPSON Mission	2
1.2 Research Question	3
1.3 Design Methodology	6
1.4 Outline	8
2 State-of-the-art	9
2.1 Propagation through the Ionosphere	9
2.1.1 Dispersion	11
2.1.2 Faraday Rotation	11
2.1.3 Ionospheric Scintillation	14
2.2 Channel Sounding technique	16
2.2.1 Pseudo-Random Binary Sequences	18
2.2.2 Galois Field	21
2.2.3 Galois Linear Feedback Shift Register	22
2.3 UL Interference Measurements through LUME-1 UHF Satellite	23
2.4 Optimal Sliding Correlator Channel Sounder Design	23
2.5 Investigation of the Ionosphere through AlfaCrux UHF Satellite	25
3 System Background and Tools	27
3.1 Docker	27
3.2 Software Defined Radio	28
3.3 GNU Radio Companion	28
3.3.1 TOTEM SDR	28
3.3.2 USRP-2901	30

4	Phase One: Matlab Simulator	33
4.1	The behaviour of the simulator	33
4.2	Chain flow	34
4.3	The GNU Radio application: PN sequence generator	35
4.4	Structure of the simulator	37
4.5	Transmitter implementation	38
4.6	Channel model entities	39
4.6.1	AWGN implementation	39
4.6.2	Free-space path loss	41
4.6.3	Doppler effect	46
4.6.4	Multipath effect	49
4.6.5	Faraday rotation	52
4.6.6	Ionospheric scintillation	54
4.7	Validation Processes and Results	55
4.7.1	Doppler shift estimation and compensation	55
4.7.2	Multipath effect analysis: the channel sounder technique	56
4.7.3	Ionospheric Scintillation: the S_4 parameter	61
4.7.4	Faraday rotation: the dual-frequency technique	62
5	Phase Two: SDR testbed	69
5.1	Testbed setup	69
5.2	Design and characterization of the communication lines	70
5.2.1	Design	70
5.2.2	Characterization	71
5.3	SDR: Characterization and Calibration procedures	74
5.3.1	USRP-2901 as receiver	74
5.3.2	TOTEM SDR as transmitter	85
5.4	Hardware-in-the-loop testing	88
5.4.1	Back-to-back measurement	89
5.4.2	HIL test with TOTEM SDR as a transmitter	89
5.4.3	HIL test with USRP-2901: comparison with TOTEM SDR	96
6	Conclusion	99
6.1	Contribution	100
6.2	Future work	100
	References	103
	Appendix	
A	Fundamentals of Radio Propagation Modeling	109
A.1	Channel Modeling	109
A.1.1	Deterministic channels	110

A.1.2	Stochastic channels	110
A.1.3	The Quasi-Stationarity condition	111
A.2	Antenna characterization	111
A.2.1	Power flux density and Radiation intensity	112
A.2.2	Gain	112
A.3	Thermal noise	115
A.3.1	Signal-to-Noise Ratio	116
A.3.2	Noise Figure	116
A.4	Friis Transmission Equation	116
B	Network Communication	119
B.1	Cubesat Space Protocol	120
B.2	Controller Area Network	120
B.3	Secure SHell	120
B.4	X11 Forwarding	121
C	Matlab Simulator code	123
C.1	Transmitter entity	123
C.2	Channel entities implementation	123
C.2.1	Thermal noise	124
C.2.2	Free-space path loss	125
C.2.3	Doppler shift	126
C.2.4	Multipath effect	126
C.2.5	Faraday rotation	128
C.2.6	Ionospheric scintillation	129
C.3	Validation process implementation	129
C.3.1	Doppler estimation and compensation	129
C.3.2	Cross-correlation for the channel sounding technique	130
C.3.3	S ₄ parameter computation	130
D	Connection configuration	131
D.1	TOTEM SDR connection	131
D.2	USRP-2901 connection	133
D.3	GNU Radio Companion Docker container	133
D.3.1	Build and run of the Docker container	134
D.3.2	SDR workstation configuration	135
D.3.3	Local machine configuration	135

List of Figures

1.1	Example of CubeSats: DEWA-SAT 1 (3U), Hyperspectral Small Satellite for Ocean Observation (HYPSO)-1 (6U) and ETV-A1 (12U). From [13].	2
1.2	The observation System-of-Systems (SoS). Each agent is selected for observing a target with different time, spatial and spectral resolution. From [17].	3
1.3	Operational concept for frequency monitoring. From [17].	4
1.4	Research design applied for the proposed thesis.	6
2.1	Example of ionospheric interactions with the electromagnetic wave. The effects that are shown are multipath effect, Faraday rotation and ionospheric scintillation. Inspired by [21].	10
2.2	Behaviour of the Total Electron Content (TEC) content along the altitude. The figure shows an idea of the altitude where HYPSO-2 will be deployed. Adapted from [22].	11
2.3	Example of <i>positive</i> dispersion. Two Gaussian pulses are generated at $t = 0$ s. Each pulse has a specific carrier frequency, i.e. $f_{c,1}$ and $f_{c,2}$, with $f_{c,1} > f_{c,2}$. The received signal $S_{RX}(\tau)$ is collected after a certain delay time. Since the medium is dispersive, the higher frequencies are faster than the lower ones. This proves why the pulse with carrier frequency $f_{c,1}$ arrives before the other pulse. In case of negative dispersion, the result is the opposite.	12
2.4	Example of how the time delay changes between lower and upper frequencies for a pulse of width τ transmitted through the ionosphere, with $TEC = 5 \times 10^{-17}$ el/m ² . From [18].	13
2.5	In Figure (a), we can observe the communication configuration that involves a CubeSat satellite. When the receiver is positioned at a low zenith angle θ_0 , we can utilize the depicted geometry in Figure (b) to derive Equation 2.3. This specific arrangement maintains a constant zenith angle θ_0 throughout the entire communication link, while the angle ψ is formed between the direction of signal propagation and the magnetic field direction denoted as B (as shown in the diagram by the arrow). From [24].	14

2.6	Faraday rotation as a function of TEC and frequency. From [18].	15
2.7	Example of a signal perturbed by the ionospheric scintillation.	16
2.8	Example of channel sounding technique. The main entities are a baseband signal $p_T(t)$ (known by the receiver entity) generated by the transmitter entity, a Local Oscillator (LO), a Power Amplifier (PA) and a Low Noise Amplifier (LNA). The received baseband signal $p_R(t)$ is used to characterise the propagation channel $H(f, t)$	16
2.9	Example of a Linear Feedback Shift Register (LFSR) configured as Simple Shift Register Generator (SSRG). From [37].	19
2.10	Example of autocorrelation function $C_x(\tau)$ of a pseudo-noise sequence.	20
2.11	Example of Fourier transform of a pseudo-noise sequence.	21
2.12	The common structure of a Galois Linear Feedback Shift Register (GLFSR) [39].	22
3.1	TOTEM SDR.	29
3.2	USRP-2901 SDR.	31
4.1	Example of a possible scenario for DL channel and LEO satellites.	33
4.2	The chain flow.	34
4.3	The GNU Radio application for generating the binary file.	36
4.4	Simplified communication chain.	37
4.5	The logical structure of the Matlab simulator.	38
4.6	Example of a receiver chain diagram, where L1 is the loss line from the antenna to the LNA, G_{LNA} is the LNA gain and L2 is the loss line from the LNA to the rest of the circuit.	41
4.7	Geometry problem of the distance between the ground station and the satellite, for $\theta \in [0, \pi/2]$. P_S , P_G and P_E are the satellite, ground station and Earth's center positions respectively.	42
4.8	Example of a triangle.	42
4.9	Geometry problem of the distance between the ground station and the satellite, for $\theta \in [\pi/2, \pi]$	44
4.10	Example of free-space path loss for $\theta \in [0, \pi]$ and satellite altitude $h = 500 \text{ km}$	45
4.11	Behavior of the Doppler shift and Doppler rate in function of the time and altitude of the satellite.	48
4.12	Example of discrete multipath scenario (a) and the corresponding Channel Impulsive Response (CIR) (b).	50
4.13	Example of refraction and reflection of a Transverse electromagnetic (TE) mode wave	50
4.14	Examples of Rician fading applied to the ionosphere channel.	51
4.15	a) Example of UHF antenna simulation result for HYPSON-2 from [66]; b) Example of how the polarization changes along different orientations.	53

4.16	Example of antenna diversity by using two crossed dipole.	54
4.17	Example of Doppler estimation and compensation by using the convolution method, considering a Doppler shift $f_D = 7267.9228$ Hz. (a) shows the signal before and after the compensation, and (b) shows the auto-convolution of the received signal in the frequency domain.	57
4.18	CIR result from discrete multipath simulation, considering $10\ \mu\text{s}$, $0.1\ \text{ms}$ and $0.2\ \text{ms}$ of exceed delays and $0\ \text{dB}$, $-1\ \text{dB}$ and $-5\ \text{dB}$ of average path gains.	58
4.19	CIR result from Rician fading multipath simulation, considering $10\ \mu\text{s}$, $0.1\ \text{ms}$ and $0.2\ \text{ms}$ of exceed delays and $0\ \text{dB}$, $-1\ \text{dB}$ and $-5\ \text{dB}$ of average path gains.	59
4.20	Example of two Rician fading multipath channel simulations, considering one (a) and ten (b) Pseudo-Noise (PN) sequences in series.	60
4.21	Visualization of the window method to compute the S_4 parameter. The pattern in blue represents the ten PN sequences that are sent in series.	61
4.22	Simulation result of ionospheric scintillation.	63
4.23	Windows method to compute the S_4 parameter. For this simulation, five different S_4 parameters are set and estimated.	64
4.24	Diagram illustrating the operation of dual-frequency technique.	64
4.25	Simulation results of Faraday rotation (FR) and use of dual-frequency technique, considering $f_{c2} = 436.25$ MHz.	67
4.26	Simulation results of FR and use of dual-frequency technique, considering $f_{c2} = 437.75$ MHz.	68
5.1	High-level view of the testbed.	70
5.2	Transmission chain between TOTEM SDR and USRP-2901.	71
5.3	General representation of a 4-port. From [73]	72
5.4	Representation of the connection lines of Figure 5.1.	72
5.5	Measured S_{21} and S_{31} parameters for both lines J1-J2 and J1-J3. The fuchsia and green lines represent the average of both S_{31} and S_{21} respectively.	73
5.6	Characterization and calibration setup for the USRP-2901 as a receiver.	74
5.7	USRP_Characterization_CARRIER.grc.	76
5.8	USRP_Characterization_CHIRP.grc.	77
5.9	Carrier at $437.05\ \text{MHz}$ read by USRP-2901, with center frequency of $437\ \text{MHz}$	78
5.10	Relation between received power by USRP-2901 and transmitted power by the signal generator. A LNA gain value (dB) is assigned for each pattern.	79
5.11	Frequency response of the LNA @ $40\ \text{dB}$	80
5.12	USRP_Calibration_RX.grc.	81

5.13	Example of In-phase (I)Quadrature (Q) imbalance (a) and Direct Current (DC) misalignment (b).	82
5.14	Visualization of the frequency setup for the LO calibration.	83
5.15	Constellation before (a) and after (b) 2 dBm of transmitted power. . . .	84
5.16	Fast Fourier Transform (FFT) magnitude of the baseband spectrum before the Rotator block and after the Low-Pass (LP) filter.	84
5.17	Setup for the characterization and calibration of the TOTEM SDR as a transmitter.	85
5.18	TOTEM_Calibration_CARRIER_TX.grc.	87
5.19	Relation between received power by the signal analyzer and transmitted power by TOTEM SDR.	88
5.20	Constellation before (a) and after (b) PA gain equal to 75 dB.	88
5.21	Interference due to the LO of TOTEM SDR captured by the signal analyzer. The PA gain is set to 15 dB.	89
5.22	a) Example of a real channel and the equivalent filters of transmitter and receiver; b) Example of back-to-back measurement, where only the filtering entities of receiver and transmitter are considered part of the system.	90
5.23	HIL_test_ChannelSounder_TOTEM_TX_v01.grc	91
5.24	HIL_test_ChannelSounder_USRP_RX_v01.grc	92
5.25	a)-b) Received samples by the USRP-2901. It is possible to notice 1) the presence of LO leakage and 2) a distortion with respect to the PN sequence generated by the GNU Radio application. Figure b) represents a close-up of figure a); c) Spectrum magnitude of the received signal. . .	94
5.26	a)-b) Received sample by the USRP-2901 after the Doppler compensation algorithm. The envelope of the received signal is more stable, meaning that the LO leakage is fairly compensated, even though the distortion is still present. Figure b) represents a close-up of figure a); c) CIR obtained by using the HIL test and TOTEM SDR as transmitter.	95
5.27	a)-b) Received samples by the USRP-2901. It is possible to notice the presence of LO leakage, but the shape of the PN sequence is visible. Figure b) represents a close-up of figure a); c) Spectrum magnitude of the received signal depicted in Figure 5.27.	97
5.28	a)-b) Received sample by the USRP-2901 after the Doppler compensation algorithm. The reduction of LO leakage is evident, without the distortion observed in Figure 5.26. Figure b) represents a close-up of figure a); c) CIR obtained by using the HIL test and USRP-2901 as transmitter. . .	98

A.1	Example of a deterministic channel model. The system is static and the transmitter generates a pulse signal at delay time $\tau = 0$ s (see right-up plot). Due to the reflection of the transmitted signal, the receiver perceives a set of pulses, defined by a certain delay and amplitude (see right-bottom plot)	110
A.2	An example of time-variant (a) and static (or time-invariant) channel (b).	111
A.3	Visualization of a solid angle. From [82].	112
A.4	Example of a dipole and spherical coordinates. Adapted from [83].	112
A.5	Examples of different aperture lobes for the ground station and incident waves.	113
A.6	Example of circularly polarized patch antenna radiation pattern. The simulation is performed with CST Studio Suite.	114
A.7	Additive White Gaussian Noise (AWGN).	115
B.1	High-level view of Secure SHell (SSH) message flow. From [88].	121
D.1	Bash output after running <code>hypso-cli</code>	131
D.2	Flatsat connection setup. From [90].	132
D.3	Output example of <code>uhd_find_devices</code> instruction.	133
D.4	High level connection scheme between the user and GNU Radio Companion.	133

List of Tables

2.1	Sliding Correlator Channel Sounder Design Equations	24
3.1	TOTEM SDR — RF Transmission characteristics.	29
3.2	TOTEM SDR — RF Reception characteristics.	30
3.3	RF characteristics of USRP-2901.	31
4.1	Simulation of ten elevation angles, considering center frequency $f_c = 436.5$ MHz and satellite altitude $h = 500$ km.	57
4.3	Parameters considered for the dual-frequency technique.	65
5.1	Chirp signal setting.	78
5.2	LP filter parameters.	83
5.3	Results from calibration and characterization procedures of the USRP-2901 as receiver, with LNA gain equal to 40 dB.	85
B.1	International Organization for Standardization (ISO)/Open Systems Interconnection (OSI) Model Layers.	119

List of Symbols

ϵ_0	permittivity in free-space: $8.8541878128 \times 10^{-12} \text{ F m}^{-1}$.
B_{av}	Average Earth's magnetic intensity.
B_{COH}	Coherence bandwidth.
c	speed of light in vacuum: $299\,792\,458 \text{ m s}^{-1}$.
dB	decibel: $x[\text{dB}] = 10\log_{10}(x)$.
G	constant of universal gravity: $6.6743 \times 10^{-11} \text{ m}^3 \text{ kg}^{-1} \text{ s}^{-2}$.
k	Boltzmann constant: $1.380\,649 \times 10^{-23} \text{ m}^2 \text{ kg s}^{-2} \text{ K}$.
M_E	Earth's mass : $5.972 \times 10^{24} \text{ kg}$.
N_0	power spectral density of the thermal noise.
R_E	Earth's equatorial radius: 6378 km.
R_{sample}	Sample rate.
R_{symbol}	Symbol rate.
S_4	S4 parameter.

T_A^{BL}	Antenna noise temperature due to the back-lobe.
T_A^{ML}	Antenna noise temperature due to the main-lobe.
T_A^{SL}	Antenna noise temperature due to the side-lobe.
T_A	Antenna noise temperature.
T_{COH}	Coherence time.
T_{comp}	Composite temperature.
T_m	Environment temperature.
T_{TX}	Time to transmit the signal.

List of Acronyms

ADC Analog-to-Digital Converter.

AOSN Autonomous Ocean Sampling Network.

APDP Average Power Delay Profile.

API Application Programming Interface.

ASV Autonomous Surface Vehicles.

AUV Autonomous Underwater Vehicles.

AWGN Additive White Gaussian Noise.

bps bits per second.

BPSK Binary Phase-shift Keying.

CAN Controller Area Network.

CD+AMP Collision Detection and Arbitration on Message Priority.

CIR Channel Impulsive Response.

CLI Command Line Interface.

COTS Commercial-Off-The-Shelf.

CSMA Carrier-Sense Multiple-Access.

CSP Cubesat Space Protocol.

CV Coefficient of Variation.

CW continuous wave.

DC Direct Current.

DL Downlink.

DSP Digital Signal Processing.

DSSS Direct Sequence Spread Spectrum.

EDF Empirical Distribution Function.

EO Earth Observation.

EPS Energy Power Supply.

FDTD Finite-Difference Time-Domain.

FFT Fast Fourier Transform.

FM Flight Model.

FR Faraday rotation.

GF Galois field.

GISM Global Ionospheric Scintillation Model.

GLFSR Galois Linear Feedback Shift Register.

GNSS Global Navigation Satellite System.

GRC GNU Radio Companion.

GUI Graphical User Interface.

HABs Harmful Algal Blooms.

HIL Hardware-In-the-Loop.

HSI Hyper Spectral Images.

HYPSONO Hyperspectral Small Satellite for Ocean Observation.

I In-phase.

I2C Inter-Integrated Circuit.

IFFT Inverse Fast Fourier Transform.

IoT Internet of Things.

IP Internet Protocol.

ISI InterSymbol Interference.

ISO International Organization for Standardization.

ITU International Telecommunication Union.

JTAG Joint Test Action Group.

LEO Low Earth Orbit.

LFSR Linear Feedback Shift Register.

LME Local Mean Envelope.

LNA Low Noise Amplifier.

LO Local Oscillator.

LoRa Long Range.

LOS Line of Sight.

LP Low-Pass.

MLS Maximum Length Sequence.

NTNU Norwegian University of Science and Technology.

OFDM Orthogonal Frequency-Division Multiplexing.

OS Operative System.

OSI Open Systems Interconnection.

PA Power Amplifier.

PDF Probability Density Function.

PDU Protocol Data Unit.

PLF Polarization Loss Factor.

PLL Phase Locked Loop.

PN Pseudo-Noise.

PSD Power Spectral Density.

PSNG Pseudo-Noise Sequence Generator.

Q Quadrature.

RF Radio Frequency.

RRC Root-Raised-Cosine.

SDR Software Defined Radio.

SI International System of Units.

SNR Signal-to-Noise Ratio.

SoC System On Chip.

SoS System-of-Systems.

sps Sample-per-Symbol.

SSH Secure SHell.

SSRG Simple Shift Register Generator.

TCP Transport Communication Protocol.

TDL Tapped Delay Line.

TE Transverse electromagnetic.

TEC Total Electron Content.

TLE Two-Line Element.

TT&C Telemetry, Tracking and Command.

TTY teletypewriter.

UART Universal Asynchronous Receiver / Transmitter.

UAV Unmanned Aerial Vehicles.

UHD USRP Hardware Driver.

UHF Ultra High Frequency.

UL Up Link.

USB Universal Serial Bus.

USRP Universal Software Radio Peripheral.

VHF Very High Frequency.

XOR eXclusive-OR.

Chapter 1

Introduction

Channel characterization is a crucial aspect in various telecommunications fields, including mobile radio networks [1], Internet of Things (IoT) [2], and satellite communications [3]. There are several methods available for channel characterization. This report focuses on one particular approach known as the *channel sounding technique* or *channel sounder*.

More concisely, this thesis aims at developing a transmission channel simulator for the Downlink (DL), specifically designed for Low Earth Orbit (LEO) satellites operating in the Ultra High Frequency (UHF) band. A transmission channel simulator is designed and implemented in a universal architecture to reproduce various scenarios, for instance by precisely considering the satellite and the ground station equipment. This artifact encompasses several factors that can introduce distortions in the electromagnetic field. Of particular interest is the interaction between the transmitted signal and the ionosphere, which serves as the primary source of channel distortion. This study explores various models found in the existing literature and evaluates their effectiveness in addressing this interaction.

After the development of the simulator, different solutions used to characterise the channel entities are discussed in Section 4.7, including the channel sounder technique. Subsequently, the testing phase of these solutions is explained, which involves the use of a dedicated testbed. The system topology and the various components are detailed, followed by the calibration and characterization phase of these components. Additionally, the utilized applications are presented. Finally, the correct functioning of the channel sounder is validated through rigorous testing using the aforementioned testbed.

Due to time constraints, this thesis emphasizes the development and validation processes concerning the simulator. Nonetheless, the work presented here provides a resource for future endeavours in planning in-orbit measurements, offering insights into the applications and other artifacts discussed within this thesis.

1.1 The HYPSO Mission

The Hyperspectral Small Satellite for Ocean Observation (HYPSO) project is the main initiative of Norwegian University of Science and Technology (NTNU) SmallSat Lab, with the mission of growing space-related knowledge at NTNU. To achieve this objective, the SmallSat Lab’s research primarily revolves around CubeSat design [4], [5].

A CubeSat [6] is a small, standardized platform that helps reduce the costs of technical developments and scientific investigations. The CubeSat comes in several sizes based on the standard CubeSat “unit”—referred to as a 1U. A 1U CubeSat is a 10 cm cube with a mass of approximately 1 to 1.33 kg. Figure 1.1 shows examples of CubeSats. Of special significance is HYPSO-1, as it represents the inaugural satellite developed by the SmallSat Lab.

Despite their small size, CubeSats have made significant contributions to space research. They have been used to monitor weather patterns [7], study the Earth’s atmosphere and climate [8], and even explore other planets [9]. Moreover, CubeSats enabled space programs for various major universities [4], [10]–[12].

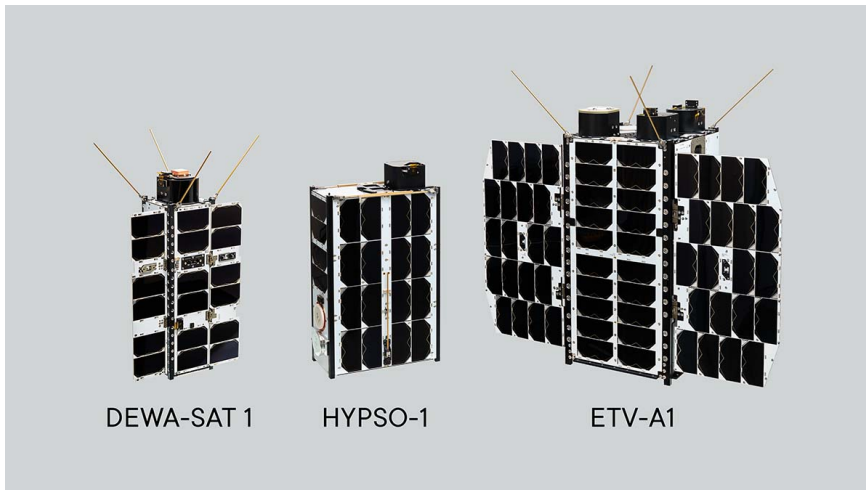


Figure 1.1: Example of CubeSats: DEWA-SAT 1 (3U), HYPSO-1 (6U) and ETV-A1 (12U). From [13].

After the success of the first mission HYPSO-1 [4], [5], SmallSat Lab started with the second and more challenging mission, HYPSO-2, which has the purpose to include a Software Defined Radio (SDR) as an additional payload. The objective of SDR is to create a payload design that can adjust to the demands of a system and environmental limitations. The mission aims at measuring radio frequency

interference and channel characteristics within the designated frequency range of 400 MHz (UHF band). Additionally, it intends to showcase communication capabilities between the satellite, terrestrial sensor nodes, and autonomous agents. The payload is based on a Commercial-Off-The-Shelf (COTS) SDR payload, the TOTEM SDR from Alén Space, Spain.

Monitoring the Earth's evolving climate requires implementing an onboard SDR. Especially the polar regions experience a remarkable impact of climate change. The northern and southern extremities of the planet are heating up at a more rapid pace than any other region on Earth, with temperatures of the Arctic ocean and atmosphere increasing twice as much as in other areas [14]. Nevertheless, obtaining comprehensive sampling coverage of environmental variables is challenging due to the vast, expanse, and limited infrastructure [15]. The HYPISO-2 satellite will be part of an Autonomous Ocean Sampling Network (AOSN). This network includes Autonomous Surface Vehicles (ASV), Autonomous Underwater Vehicles (AUV) and Unmanned Aerial Vehicles (UAV) [16]. Figure 1.2 shows the System-of-Systems (SoS) that enables the concept of AOSN.

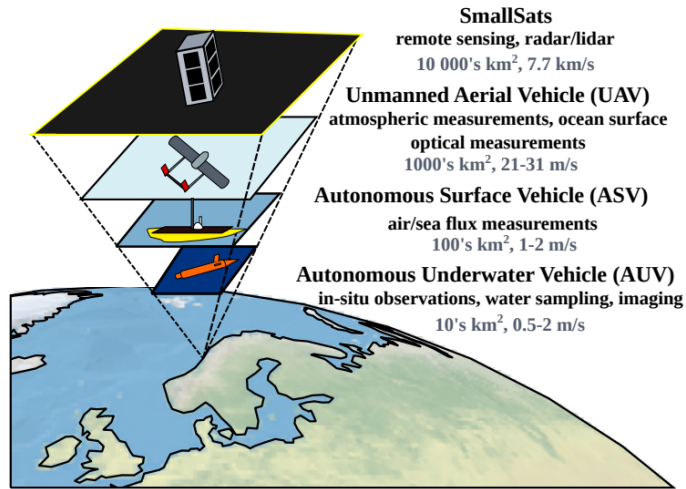


Figure 1.2: The observation System-of-Systems (SoS). Each agent is selected for observing a target with different time, spatial and spectral resolution. From [17].

1.2 Research Question

As previously indicated, the research team has identified the UHF frequency band as a well-suited choice for the mission. This choice stems from the favourable penetration properties exhibited by UHF frequencies, wherein electromagnetic waves

can effortlessly traverse obstacles. This phenomenon can be attributed to the relatively smaller values of the considered frequencies, since higher frequencies exhibit reduced coverage distances, as confirmed by the Friis formula. The Friis formula is presented in Section A.4. Moreover, the implementation of higher frequency systems requires the use of advanced antenna pointing systems and larger terminals, which may not be conducive to the requirements of small sensors and UAVs [17] (the idea of the frequency monitoring mission is shown in Figure 1.3).

The three main objectives of frequency monitoring are identified next:

1. *Upload measurement parameters and scheduling*: when the ground station has visibility with the satellite, it can send the parameters and scheduling to the satellite to perform measurements;
2. *Measurement campaign*: the satellite performs both time and frequency measurements and keeps them in memory;
3. *Downlink measurements result*: when all the measurements are carried out, the data are downlinked to the ground station using the S-band.

Given the current unavailability of measurements from HYPSON-2, it becomes imperative to proactively establish the groundwork for future acquisitions of information from the satellite.

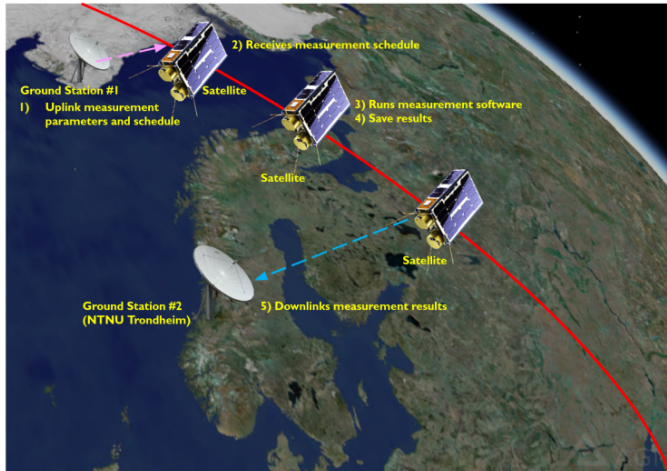


Figure 1.3: Operational concept for frequency monitoring. From [17].

This thesis seeks to answer the following research question: *How does the DL channel perform for LEO satellites and UHF bands?* The specific objective

is to study the relevant channel characteristics that need consideration and assess their influence on the transmitted signal. Despite the existing body of literature on the subject, there remains a significant research gap, preventing the construction of a comprehensive model for a universal downlink channel. Even the International Telecommunication Union (ITU) (see Recommendation ITU-R P.531-14 [18]) fall short of providing a comprehensive understanding about the topic.

The research group has already made significant work on the characterization of the uplink channel in the UHF band. For instance, the first result was obtained after a measurement campaign [10], where it was discovered that in defined areas, very high peak power values were detected due to the presence of ground radars. Moreover, Endresen et al. [19] aimed to measure the temporal properties of uplink interference and characterise the interference produced by the ground radars mentioned before.

The goal of the presented Master's thesis is to thoroughly examine the channel entities in detail in function of the findings offered by the literature, with the aim of creating a comprehensive model that can be universally applied. Universal means a channel model applicable in any scenario involving LEO satellite-to-ground station links, always considering the aforementioned UHF band. The outcome of this thesis are to:

- get a better understanding of the channel entities involved in the DL channel;
- study the possibility to test oriented communication protocols through the channel model;
- produce of useful applications to characterise the various channel entities. This leads to the development of algorithms capable of separating the various effects of the transmission channel and estimating their influence on the signal being transmitted.

Through the channel model proposed by this work, it is possible to exploit multiple channel model entities present in the downlink channel (e.g. the effects of the ionosphere on the electromagnetic field) and to apply them in the uplink channel as well. This is possible thanks to the reciprocity property [20]. In summary, the reciprocity property states that the channel's effect on a transmitted signal remains the same, regardless of whether we consider the forward or backward communication link between two points (A to B or B to A). For instance, the free-space path loss is a reciprocal phenomenon as the distance between points A and B remains constant, while the interference environment may differ based on their positions in space.

1.3 Design Methodology

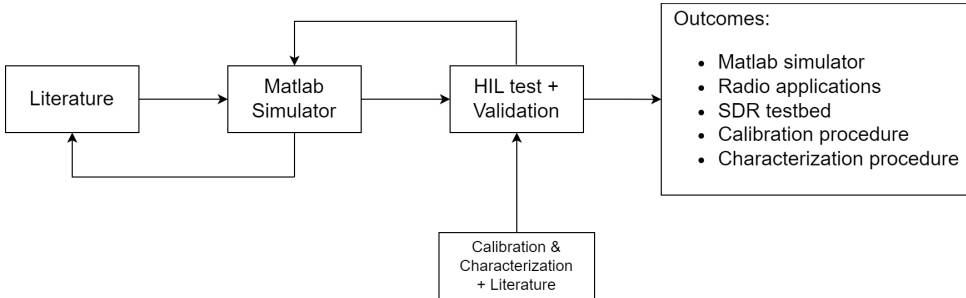


Figure 1.4: Research design applied for the proposed thesis.

A collection of artifacts and methodologies is defined to contribute to the investigation of the DL channel for LEO satellites. Figure 1.4 depicts the research design scheme.

The initial phase encompasses comprehensive research conducted through an extensive review of relevant literature sources. We conducted a thorough literature review to identify all the elements compatible with the aforementioned channel. We examined various research findings to compare the information and understand the key factors affecting the channel, such as latitude, longitude, bandwidth, altitude, daytime, and solar activity. The outcomes of this phase encompass the identification of channel entities along with the corresponding variables employed to modulate their influence on the channel.

Subsequently, the Matlab simulator artifact is obtained by implementing diverse models of the channel entities and utilizing the versatile capabilities of Matlab. Leveraging its robust and user-friendly functionality, Matlab emerges as a highly effective and dependable choice for conducting simulations across a wide range of fields. Due to its comprehensive documentation, the simulator enables the seamless application of every channel effect. In the event of any inconsistencies in the obtained results, it becomes imperative to revisit the preceding step accordingly, as depicted in Figure 1.4.

Following the simulation phase, the subsequent step involves setting up a testbed to validate the obtained results, employing a technique known as Hardware-In-the-Loop (HIL) testing. This approach encompasses the integration of real system components, such as various radio elements, with a computer-based simulation environment. By combining physical hardware with virtual simulations, HIL testing enables a comprehensive assessment of the system’s performance under realistic conditions.

During the testbed setup, careful selection of system components and tools for conducting calibrations is essential. The choice of calibration procedures is informed by expert guidance from professors and extensive research conducted in the literature. The primary objective of the testbed is to verify the efficiency of the propagation channel measurement system. By leveraging the HIL approach, the testbed facilitates the validation of the simulator's results and paves the way for future testing and experimentation with a real satellite system.

Finally, the system undergoes validation, wherein a generated signal is employed to characterise the channel effects. This signal is subsequently received by a dedicated receiver system that collects the data required for post-processing functions outlined within the simulator. Should the obtained data deviate from the expected outcomes, it becomes imperative to revisit either the calibration and characterization phase or the Matlab simulator artifact, depending on the problem's nature.

Upon concluding this study, a collection of artifacts is obtained, with the Matlab simulator being the primary one. This simulator is then subjected to validation using the testbed. Additionally, a series of radio applications are developed to control the radio components of the testbed. These applications embrace two distinct entities for channel modeling, alongside an assortment of applications intended for conducting calibration and characterization phases. The applications are integrated with the calibration and characterization procedure artifacts, which comprehensively documents the requisite operations for executing the aforementioned phases. In summary, the SDR testbed phase encompasses a streamlined toolchain, facilitating subsequent orbital testing of the system delineated within this study.

1.4 Outline

Chapter 2 provides an overview of the state-of-the-art related to the topic of this Master's thesis. It covers fundamental concepts related to the electromagnetic propagation through the ionosphere (see Section 2.1). The chapter delves into the channel sounding technique and emphasizes the significance of the Pseudo-Noise (PN) sequence in its operation (see Section 2.2). Lastly, previous works that form the foundation of the research conducted in this thesis are discussed (see Sections 2.3, 2.4 and 2.5).

Chapter 3 focuses on the tools utilized to support the thesis. Significantly, it introduces the concept of SDR (see Section 3.2) as the underlying technology for the testbed. Detailed specifications about the used SDRs are reported in Sections 3.3.1 and 3.3.2.

Chapter 4 presents a comprehensive overview of the Matlab simulator's operation. It discusses the channel models integrated into the simulator and elucidates the motivations and assumptions behind them (see Section 4.6). The chapter explores the structure of the simulator, starting with the GNU Radio application (see Section 4.3) and concluding with the validation processes and results (see Section 4.7). This phase highlights the crucial role of the channel sounder in characterizing the propagation channel. Other methods for the identification of channel entities such as the auto-convolution method for the Doppler shift and the S_4 parameter for the characterization of ionospheric scintillation amplitude are introduced.

Chapter 5 addresses the subsequent stage of the simulator, namely the SDR testbed. It delves into the system components and the design choices made. Detailed explanations of the setup process for enabling the communication with the SDR devices using the tools introduced in Chapter 3 are provided. For completeness, the connection configuration of the SDR testbed is detailed in Appendix D. The chapter covers the characterization and calibration procedures for both communication lines (see Section 5.2) and radio devices (see Section 5.3). Lastly, it concludes with the validation of the channel sounder and the simulator through the HIL testing phase (see Section 5.4), thus concluding the work presented in this report.

Finally, Chapter 6 discusses the conclusions of the thesis, encompassing the contributions and possible future work that can be performed to take the work forward.

Chapter 2

State-of-the-art

This Chapter describes the state-of-the-art of the proposed thesis. Initially, fundamentals related to channel propagation through the ionosphere in Section 2.1 are introduced and, subsequently, the channel sounding technique in Section 2.2. Finally, previous works are briefly discussed in Sections 2.3, 2.4 and 2.5. In Appendix A, some more basic theory concepts such as channel propagation, antennas and noise are detailed.

2.1 Channel entities in LEO satellites: propagation through the Ionosphere

The propagation of radio waves between a ground station and a satellite is affected by diverse environmental conditions and propagation phenomena. As the signal travels through the atmosphere and ionospheric layers, it undergoes “smearing”, causing variations and distortions in its amplitude, phase, polarization, and delay time along the path.

The frequency parameter is crucial in determining the effects on satellite-ground station links. The ionosphere, located approximately between 50 to 2000 km above the Earth’s surface, is divided into layers D, E, and F (see Figure 2.1), which vary in altitude. Below approximately 30 MHz, signal propagation is not possible due to absorption and reflection in the ionosphere [23]. As the frequency increases above 30 MHz, propagation becomes feasible, although the signal properties undergo modifications. Location and daytime introduce additional variables into the equation. For frequencies above 3 GHz, ionospheric effects have less influence [18].

The recommendation of the International Telecommunication Union (ITU) named ITU-R P.531-14 of the 08/2019 [18] describes three main ionospheric effects. The first is the rotation of polarization, called Faraday rotation (FR), which impacts the polarization plane of the arrivals, where arrival stands for a radio wave that crosses a particular propagation path. Ionospheric scintillation is another effect characterised

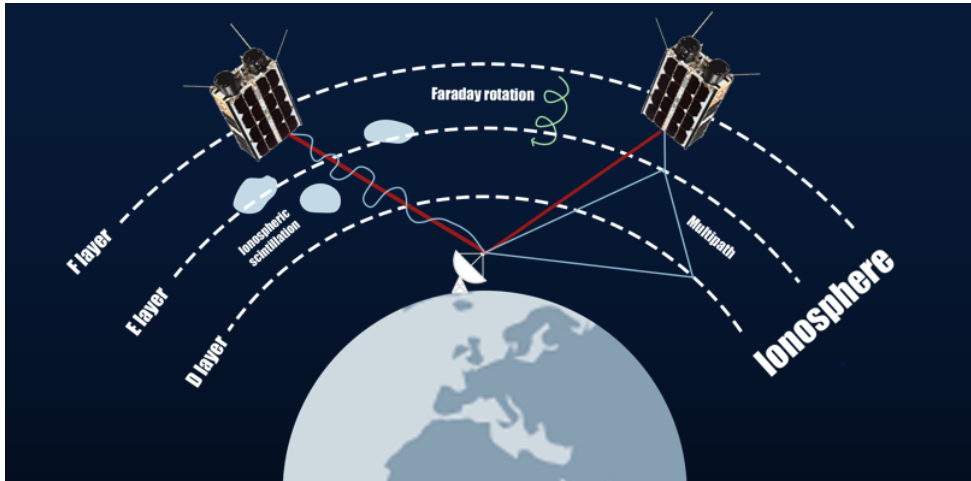


Figure 2.1: Example of ionospheric interactions with the electromagnetic wave. The effects that are shown are multipath effect, Faraday rotation and ionospheric scintillation. Inspired by [21].

by non-deterministic behavior. Finally, group velocity dispersion arises from the non-linear relationship between ionospheric electron content and frequency.

The ionosphere contains free electrons and positive ions, with ionization occurring primarily in the lower region. The electron concentration is a parameter that defines the degradation of the radio wave caused by the ionosphere. The electron density varies with altitude in each ionospheric layer, increasing at higher altitudes. It is also influenced by factors such as the sunspot cycle, solar activity, geomagnetic storms, and latitude [24] [25]. Mid latitudes exhibit more homogeneity, while high latitudes near the aurora region are more unpredictable. However, a method to determine the electron concentration has been proposed by [18].

The Total Electron Content (TEC) refers to the total number of electrons present along a column with cross-section of 1 m^2 . TEC is expressed in analytical form in Equation 2.1, where l is the propagation path in meter and n_e is the electron concentration in electron/ m^3

$$TEC = \int_l n_e(x) dx \quad (2.1)$$

Advancements in TEC estimation methods have been made to enhance the performance of Global Navigation Satellite System (GNSS) systems [26]–[28].

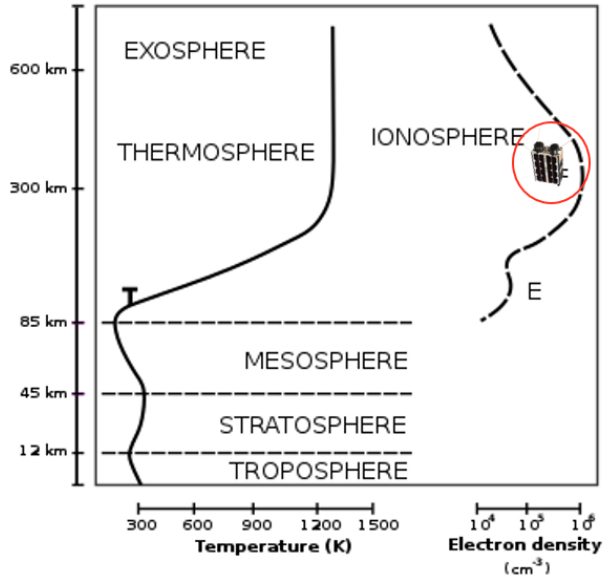


Figure 2.2: Behaviour of the Total Electron Content (TEC) content along the altitude. The figure shows an idea of the altitude where Hyperspectral Small Satellite for Ocean Observation (HYPSO)-2 will be deployed. Adapted from [22].

2.1.1 Dispersion

Dispersion is a channel characteristic resulting from the ionosphere’s dispersive nature as a medium. Dispersion causes different frequencies to travel at different speeds (see Figure 2.3), formally called *group velocities*, resulting in a spreading out or “smearing” of the signal over time. The differential delay quantifies the difference in arrival times between these frequency components. Hence, wideband transmission systems operating at Very High Frequency (VHF) and possibly Ultra High Frequency (UHF) must account for this phenomenon.

Figure 2.4 shows the behavior of the differential delay in function of TEC, pulse width τ of the transmitted signal and frequency. For instance, considering $\text{TEC} = 5 \times 10^{-17} \text{ el/m}^2$ and $\tau = 1 \mu\text{s}$, the perceived differential delay for 200 MHz and 600 MHz is $0.02 \mu\text{s}$ and $0.00074 \mu\text{s}$ respectively.

2.1.2 Faraday Rotation

CubeSats are equipped with either linearly or circularly polarized antennas, However, linearly polarized antennas require a proper antenna alignment for successful reception. Indeed, matching the transmitter and receiver antenna polarizations is a major challenge due to ionospheric effects, specifically for FR. This effect occurs when the

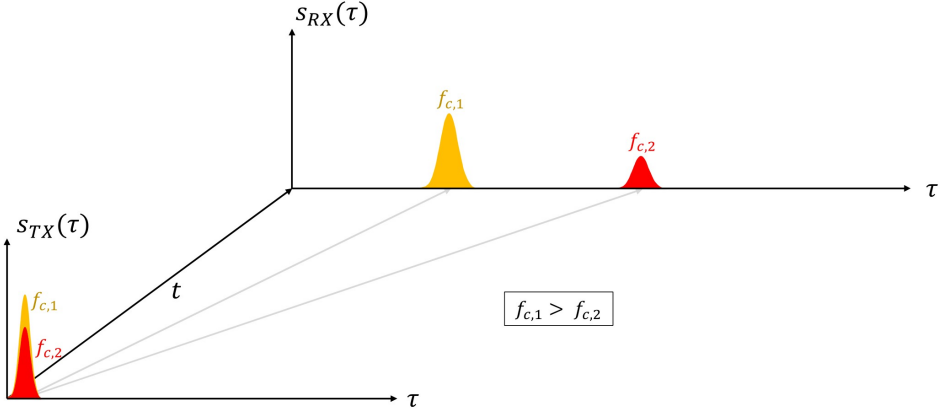


Figure 2.3: Example of *positive* dispersion. Two Gaussian pulses are generated at $t = 0$ s. Each pulse has a specific carrier frequency, i.e. $f_{c,1}$ and $f_{c,2}$, with $f_{c,1} > f_{c,2}$. The received signal $S_{RX}(\tau)$ is collected after a certain delay time. Since the medium is dispersive, the higher frequencies are faster than the lower ones. This proves why the pulse with carrier frequency $f_{c,1}$ arrives before the other pulse. In case of negative dispersion, the result is the opposite.

polarization plane of linearly-polarized radio waves is rotated during propagation through the ionospheric medium under the influence of the geomagnetic field and the TEC. The magnitude of the FR angle is inversely proportional to the squared frequency of the signal. Besides frequency, the magnitude of the FR angle is influenced by other physical quantities such as the geomagnetic field and the electron density in the ionosphere. The FR factor is written in the complete form in Equation 2.2, where c represents the light speed in vacuum, e is the electron charge, m is the electron mass, ϵ_0 is the permittivity of free-space, f is the frequency of the signal, N_e is the electron density, and B is the magnetic field. ψ represents the angle between the electromagnetic wave vector and the Earth's magnetic field vector. Furthermore, the integration is carried out along the propagation path with infinitesimal line element ds .

$$FR = \frac{e^3}{8\pi^2 m^2 c \epsilon_0 f^2} \int N_e B \cos(\psi) ds \quad (\text{rad}) \quad (2.2)$$

After some computations, Equation 2.2 can be rewritten as follow:

$$FR = \frac{K}{f^2} B \cos(\psi) \sec(\theta_0) \cdot TEC \quad (\text{rad}) \quad (2.3)$$

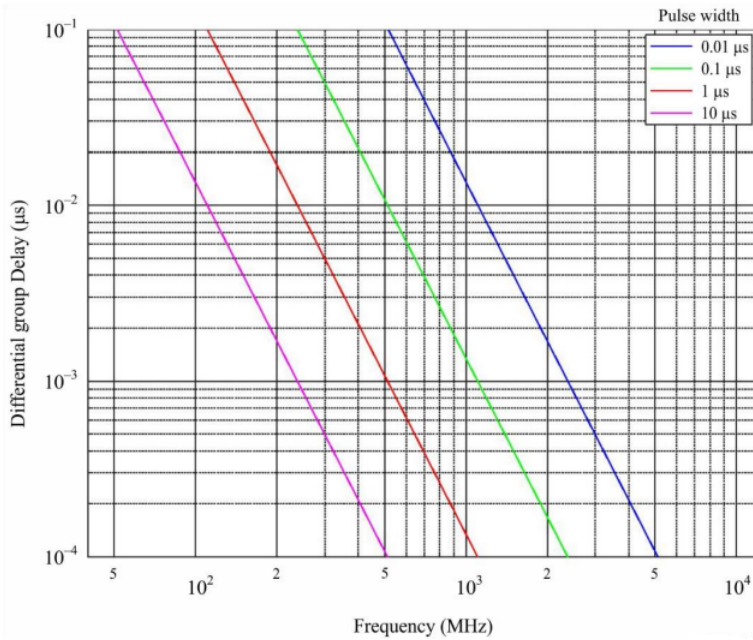


Figure 2.4: Example of how the time delay changes between lower and upper frequencies for a pulse of width τ transmitted through the ionosphere, with $TEC = 5 \times 10^{-17}$ el/m². From [18].

where the constant magnetic field factor K can be determined by assuming a fixed altitude of 400 km, as mentioned in reference [29]. In International System of Units (SI) units, K has a constant value of 2.365×10^4 A m²/kg. Lastly, TEC is obtained by Equation 2.1.

Another simplified formula for the FR is provided by [18] and it is shown hereafter:

$$FR = 2.36 \times 10^{-14} \frac{B_{av} TEC}{f^2} \quad (\text{rad}) \quad (2.4)$$

where B_{av} is the average Earth magnetic field measured in Wb m⁻² or T and f is the frequency in gigahertz. Figure 2.5 illustrates the interaction between the Earth's magnetic field and the transmitted signal. It is highlighted that the intensity of Faraday rotation depends on the zenith angle θ_0 and the intensity of the Faraday rotation, as depicted by Equation 2.3. Figure 2.6 shows FR in function of the frequency and the TEC. As it can be noticed, the higher the frequency, the lower the rotation of the polarization plane due to FR.

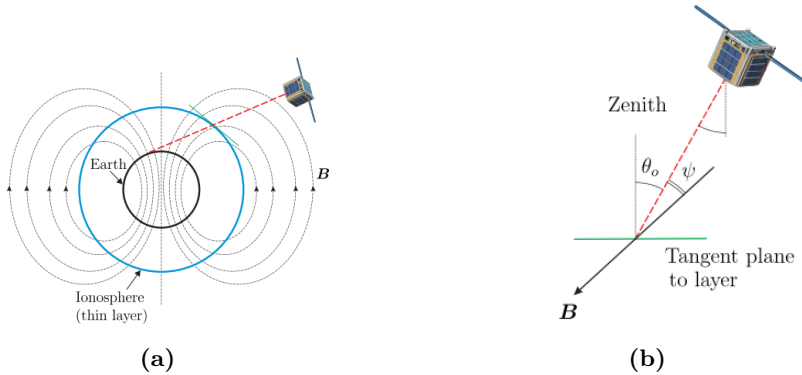


Figure 2.5: In Figure (a), we can observe the communication configuration that involves a CubeSat satellite. When the receiver is positioned at a low zenith angle θ_0 , we can utilize the depicted geometry in Figure (b) to derive Equation 2.3. This specific arrangement maintains a constant zenith angle θ_0 throughout the entire communication link, while the angle ψ is formed between the direction of signal propagation and the magnetic field direction denoted as B (as shown in the diagram by the arrow). From [24].

Another possibility to estimate the FR values is by using the Global Ionospheric Scintillation Model (GISM) [30]. GISM provides a global view of ionospheric scintillation events, considering factors like solar activity, geomagnetic conditions, and geographic locations to model electron density variations affecting satellite-based communication systems. Due to the lack of time, the aforementioned model is not considered in this thesis.

2.1.3 Ionospheric Scintillation

The refractive index of the ionospheric medium can experience rapid and random fluctuations due to the presence of plasma irregularities, which can range from centimeters to hundreds of kilometers in scale. These fluctuations can result in the amplitude and phase of the trans-ionospheric signal being rapidly and randomly modulated, a phenomenon known as *scintillation*. For trans-ionospheric signals with frequencies below 3 GHz, scintillation is one of the most severe disruptions that can occur. In equatorial regions, this phenomenon is more likely to occur during post-sunset hours, with particularly high activity during equinoxes [24].

Different models were proposed to represent the ionospheric scintillation. There are some analytical models such as the Fremouw and Rino models and the Aarons model [31] that give an understanding of how the fluctuation behaves in the presence of a radio wave. Nowadays, the most important model is GISM [30] that is exploited in many applications [24], [32], [33].

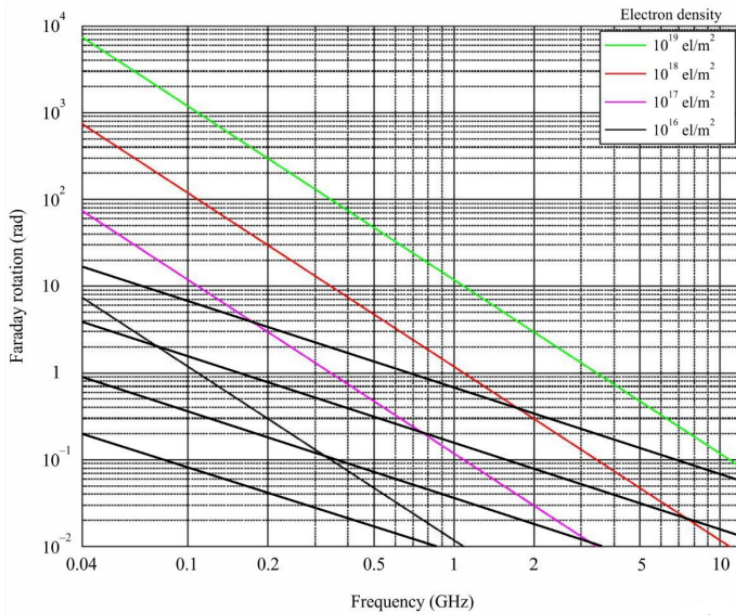


Figure 2.6: Faraday rotation as a function of TEC and frequency. From [18].

The magnitude and phase scintillation levels are often characterised by two indices: S_4 and σ_ψ , respectively. S_4 is calculated as the standard deviation of the normalized signal power over a specified period and is classified into three levels: weak ($S_4 < 0.3$), moderate ($0.3 \leq S_4 \leq 0.6$), and severe ($S_4 > 0.6$). The formula of S_4 is shown in Equation 2.5.

$$S_4 = \sqrt{\frac{\langle I^2 \rangle - \langle I \rangle^2}{\langle I \rangle^2}} \quad (2.5)$$

In the given context, the symbol I represents the intensity of the signal, which is directly proportional to the square of the signal amplitude. The notation $\langle \cdot \rangle$ stands for the averaging of the received intensity over time, with the assumption that the received intensity is a random process that satisfies the ergodic principle [18].

Given the ionospheric index S_4 , it is possible to have an estimation of the peak-to-peak fluctuation of the signal intensity by means of the following empirical formula [18]:

$$P_{fluc} = 27.5 \cdot S_4^{1.26} \quad (\text{dB}) \quad (2.6)$$

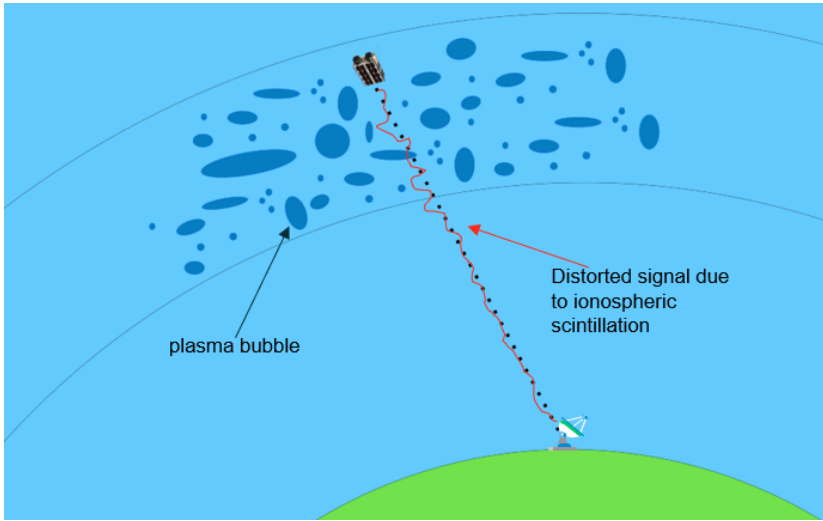


Figure 2.7: Example of a signal perturbed by the ionospheric scintillation.

where S_4 is bounded between 0 and 1. The limitation with Equation 2.6 is the absence of the stochastic behaviour of the fluctuation.

2.2 Channel Sounding technique

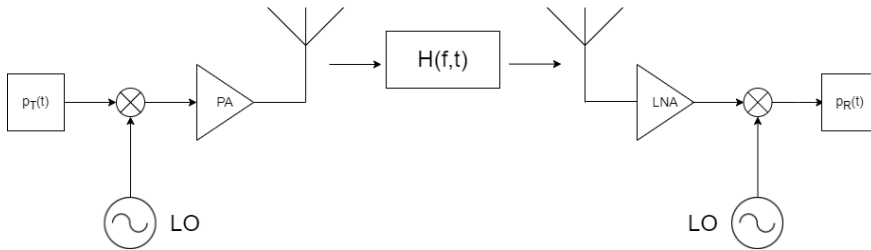


Figure 2.8: Example of channel sounding technique. The main entities are a baseband signal $p_T(t)$ (known by the receiver entity) generated by the transmitter entity, a Local Oscillator (LO), a Power Amplifier (PA) and a Low Noise Amplifier (LNA). The received baseband signal $p_R(t)$ is used to characterise the propagation channel $H(f, t)$.

As previously discussed, the focus of this thesis is the channel characterization. Nowadays, many techniques are available to achieve that. One of these is the so-called channel sounding technique (see Figure 2.8). Channel sounding is a technique used in wireless communication systems to assess the characteristics of the communication channel between the transmitter and the receiver. It involves the transmission of known signals, which propagate through the channel and are collected by the receiver.

By analyzing the received signals, valuable information about the channel's properties can be extracted, for instance, signal strength, delay spread, Doppler spread, and frequency response.

Channel sounding can be classified into two categories: narrowband channel sounding and wideband channel sounding [34].

- *Narrowband Channel Sounding*: the transmitted signals have a narrow bandwidth compared to the overall frequency range of interest. In general, the coherence bandwidth is considered as a reference. In brief, the coherence bandwidth, also indicated by B_{COH} , is the frequency range over which the channel can be interpreted constant [35]. Typically, narrowband channel sounding techniques involve transmitting continuous wave (CW) signals or tone-like signals at a single frequency or a few closely spaced frequencies. Narrowband channel sounding is commonly used in applications where the channel characteristics vary slowly with frequency (meaning that the coherence bandwidth is very large) or when the band availability is limited;
- *Wideband Channel Sounding*: it utilizes signals with a wide bandwidth, spanning a considerable portion of the frequency spectrum. The transmitted signals in wideband channel sounding are often designed to have broadband characteristics, for example pulse-like waveforms or wideband frequency sweeps. This allows for the simultaneous estimation of channel parameters across a broader range of frequencies, leading to a finer temporal resolution of the channel entity.

Both narrowband and wideband channel sounding techniques have their respective advantages and applications. Narrowband techniques are typically simpler to implement and suitable for scenarios where the channel behavior is relatively constant over small bandwidths. On the other hand, wideband techniques offer a more detailed and accurate characterization of the channel, enabling the design and optimization of communication systems that can efficiently mitigate the effects of time-varying and frequency-selective channel impairments.

Nevertheless, both solutions use the same approach to model a wireless communication channel, i.e. by using random pulses [36]. The random pulses are used to estimate the Channel Impulsive Response (CIR), under the quasi-stationary condition.

Hereafter, a general process for modeling a wireless communication channel using random pulses based on Figure 2.8 is presented:

1. Generate a known baseband pseudo-noise signal $p_T(t)$ that represents the transmitted signal;
2. Transmit the pulse over the channel $H(f, t)$;
3. Measure the received signal at the receiver $p_R(t)$;
4. Estimate the channel impulse response by correlating $p_R(t)$ and $p_T(t)$;

2.2.1 Pseudo-Random Binary Sequences

A Pseudo-Random Binary Sequence [37], also known as a Pseudo-Noise (PN) sequence, is a binary sequence that appears to be random but is actually deterministic and generated by a well-defined algorithm. A Pseudo-Noise Sequence Generator (PSNG) is normally obtained by a Tapped Delay Line (TDL) and a combination logic, as shown in Figure 2.9. The output sequence depends on the connections between the tapped outputs and the logic.

Let us consider a pseudo-random binary sequence ($a_i \in \{0, 1\}$) described by the Equation 2.7 [36], where a_i is periodic with period L (i.e. $a_{i+L} = a_i$) and $c_i \in \{0, 1\}$ is the *feedback coefficient*.

$$a_n = \sum_{i=-1}^N c_i a_{n-i} \quad (2.7)$$

In a nutshell, a pseudo-noise sequence is obtained by a linear combination of the previous N terms. Let us assume $c_N = 1$, so that a_{n-N} is used to compute a_n . The *characteristic polynomial* $f(x)$ [36] is defined in Equation 2.8.

$$f(x) = 1 - \sum_{i=1}^N c_i x^i \quad (2.8)$$

and the *generating function* $G(x)$ [36] is defined in function of $f(x)$, and it can be proven that the coefficients of the polynomial function $G(x)$ are in function of a_i :

$$G(x) = \frac{1}{f(x)} = \sum_{i=1}^{\infty} a_i x^i \quad (2.9)$$

A significant category of pseudo-random binary sequences is referred to as *maximal sequences* [36], commonly known as *m-sequences*. This class is defined by having the longest period L that can be produced by Equation 2.7. The period L of an

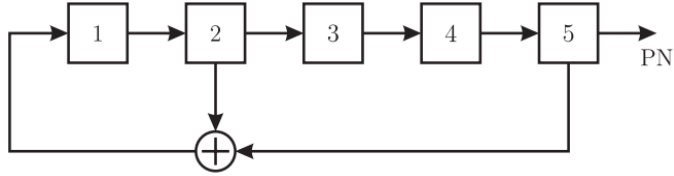


Figure 2.9: Example of a Linear Feedback Shift Register (LFSR) configured as Simple Shift Register Generator (SSRG). From [37].

m-sequence is given by Equation 2.10, where N is the number of terms a_i used to obtain a_N , as depicted in Equation 2.7. Hence, the length of the m-sequence L is computed as shown in Equation 2.10.

$$L = 2^N - 1 \quad (2.10)$$

A possible logical circuit that can generate a pseudo-random binary sequence is the so-called Linear Feedback Shift Register (LFSR).

The LFSR is a hardware implementation of the algorithm described by Equation 2.7 [37]. It utilizes an N -bit shift register to store the previous N terms of the m-sequence. The current term a_n is determined by weighting and summing the terms in the i -th registers using their respective feedback coefficients c_i , followed by a modulo 2 operation using eXclusive-OR (XOR) gates. This implementation is commonly known as Simple Shift Register Generator (SSRG).

Let us consider a N -bit LFSR configured as SSRG with m-sequence capabilities. The shift registers have a clock with a frequency f_c , called *chip rate*. Each generated *chip* has an amplitude of $\pm V_0$, where $+V_0$ corresponds to $a_i = 1$ and $-V_0$ to $a_i = 0$. The *PN sequence* $x(t)$ [37] can be written as depicted in Equation 2.11.

$$\begin{cases} x(t) = \sum_{i \in \mathbb{Z}} V_0(2a_i - 1) \Pi(t/T_c - i - 1/2) \\ \Pi(y) = u(1/2 - |y|), \text{ rectangular function} \\ u(\cdot), \text{ Heaviside step function} \end{cases} \quad (2.11)$$

PN Autocorrelation

The *autocorrelation function* $C_x(\tau)$ of a pseudo-noise sequence is depicted in Equation 2.12, where $T_c = 1/f_c$ is the *chip time*.

$$\begin{cases} C_x(\tau) = V_0^2 [\sum_{i \in \mathbb{Z}} \{(1 + \frac{1}{L}) \Lambda(\frac{\tau - iLT_c}{T_c})\} - \frac{1}{L}] \\ \Lambda(y) = (1 - |y|)u(1 - |y|), \text{ triangle function} \end{cases} \quad (2.12)$$

Equation 2.12 describes a train of triangular pulses, where the base width is equal to $2T_c$, a maximum amplitude of T_0^2 , a period of LT_c and a Direct Current (DC) offset of $-V_0^2/L$. An example of autocorrelation function is shown in Figure 2.10.

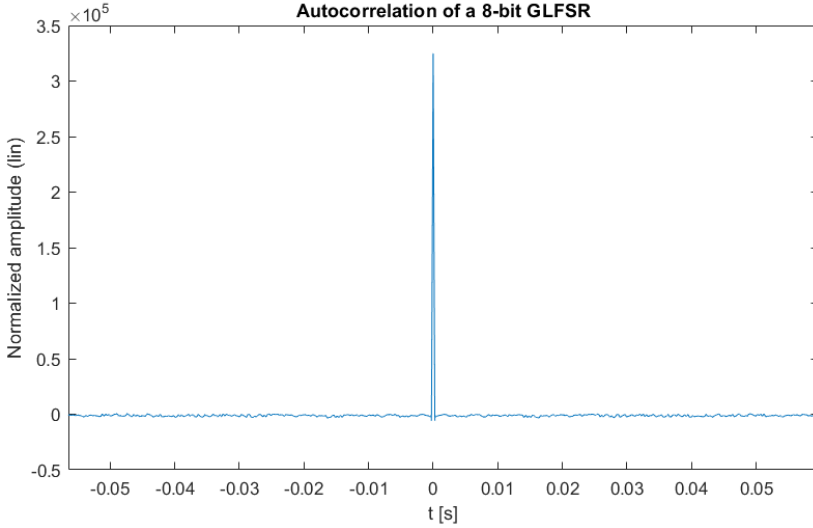


Figure 2.10: Example of autocorrelation function $C_x(\tau)$ of a pseudo-noise sequence.

PN Frequency Spectrum

From Equation 2.11, it is possible to obtain the Fourier transform $X(f)$ of the signal $x(t)$ as depicted in Equation 2.13.

$$\begin{cases} X(f) = F[x(t)] = \frac{V_0}{L} \sum_{k \in \mathbb{Z}} \text{sinc}(\frac{k}{L}) \delta(f - \frac{f_c k}{L}) e^{j \frac{k\pi}{L}} \sum_{i=1}^L [(2a_i - 1) e^{-j \frac{2k\pi}{L} i}] \\ \text{sinc}(y) = \frac{\sin(\pi y)}{\pi y} \\ \delta(\cdot), \text{ Dirac delta function} \\ F[\cdot], \text{ Fourier transform} \end{cases} \quad (2.13)$$

From Equation 2.13, it is evident that the spectrum of a PN signal consists of a series of Dirac delta functions located at integer multiples of f_c/L . Moreover, the amplitude of the spectrum is limited by the value of $\text{sinc}(k/L)$. Figure 2.11 exhibits

the spectrum amplitude of a PN signal, which has been produced from an m-sequence of length $L = 2^8 - 1 = 255$. It is important to note that the majority of the signal's power is concentrated between $-f_c$ and f_c .

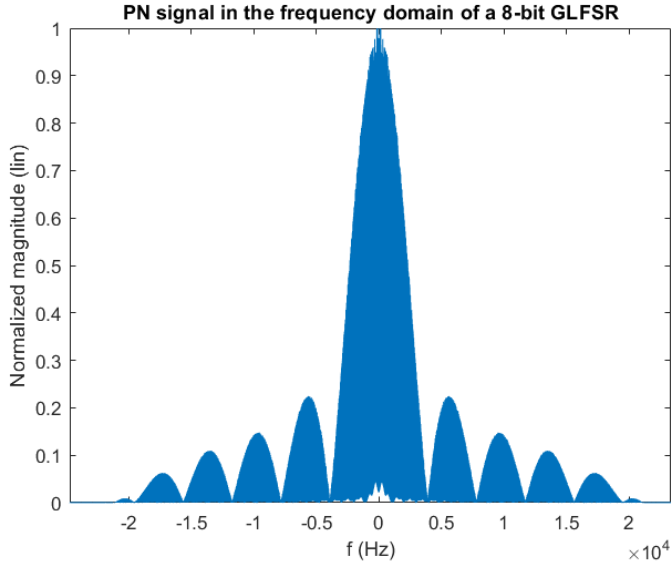


Figure 2.11: Example of Fourier transform of a pseudo-noise sequence.

2.2.2 Galois Field

A Galois field (GF) [38], also known as a finite field, is a mathematical structure that consists of a finite set of elements along with two operations: addition and multiplication.

In a Galois field, the number of elements, denoted as q , is always a prime power ($q = p^\delta$), where p is a prime number and δ is a positive integer. The elements of the field can be represented by integers from 0 to $q - 1$.

The addition operation in a Galois field follows modular arithmetic, where the result of adding two elements is taken modulo q . Similarly, the multiplication operation is performed modulo q , but with additional rules specific to Galois fields.

Galois fields are often denoted as $GF(q)$, where q represents the number of elements in the field. For example, $GF(2^8)$ denotes a Galois field with $2^8 = 256$ elements.

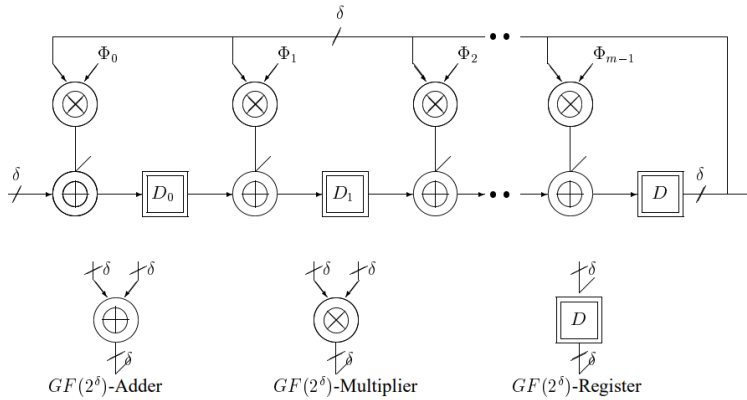


Figure 2.12: The common structure of a GLFSR [39].

2.2.3 Galois Linear Feedback Shift Register

A Galois Linear Feedback Shift Register (GLFSR) is a type of pseudo-random number generator widely used in digital systems. It is a type of LFSR that is defined over Galois fields $GF(2^\delta)$, where $\delta \leq 1$. Consequently, GLFSRs encompass LFSRs as a superset, where $\delta = 1$ [39].

The main property of GLFSR is that the output sequence is repeated after a maximum of $2^\delta - 1$ clock cycles, where δ is the number of bits of the shift register (or flip-flop). The output sequence exhibits good statistical properties, making it suitable for many applications where random numbers are required. The structure of a GLFSR, as shown in Figure 2.12, encompasses register stages, adders, multipliers, and interconnections.

GLFSRs are widely used in many applications, including cryptography [40], digital communications [41], and simulations. Their simplicity and reactivity make them an attractive choice for generating pseudo-random numbers in digital systems.

2.3 Satellite Uplink Interference Measurements in the 437 MHz UHF Amateur Radio Band Onboard LUME-1

The solution proposed by Gara Quintana-Diaza et al. [42] for measuring interference in the uplink is based on the Local Mean Envelope (LME) to characterise the time and frequency behavior of the uplink channel. The measurements are conducted using LUME-1 satellite. The satellite is equipped by the TOTEM Software Defined Radio (SDR) (see Section 3.3.1) from Alén Space, focusing on the UHF band with center frequency of 437.28 MHz.

The research analyzes the time and frequency characteristics of the interference. The analysis reveals that the channel's behavior is highly non-Additive White Gaussian Noise (AWGN) in nature, which challenges the application of error correction codes and link budgets assuming AWGN in this band.

The findings presented in [42] have significantly contributed to the development of the methodology outlined in this thesis and presented in Section 1.3. Indeed, a three-step process is applied in order to achieve the interference characterization. Firstly, Matlab simulations are conducted to gain insights into the interaction of various interference types with the LME algorithm. Secondly, the LME algorithm is converted into C++ language and executed on a computer, gathering raw IQ samples from the TOTEM SDR through a remote connection over Internet Protocol (IP). Finally, the algorithm undergoes thorough testing on a dedicated SDR testbed, serving as the ultimate validation.

2.4 Optimal Sliding Correlator Channel Sounder Design

The sliding correlator channel sounder is a cost-effective, versatile method for radio propagation engineers. Researchers studying CIR methods can benefit from this approach, as it can be built using off-the-shelf components. In this paper, proposed by Ryan J. Pirkl et al. [37], a set of mathematical tools are defined in order to design an optimal sliding correlator channel sounder. The outcomes of this paper are used to design the channel sounder outlined in Section 2.2.

The sliding correlator channel sounder utilizes cross-correlation to detect the original transmitted signal at the receiver. The cross-correlation $C_{rx}(\tau)$ between the received signal $r(t)$ and a known signal $x(t)$ is defined by Equation 2.14. Assuming a static multipath environment without AWGN, the CIR $h(\tau)$ can be represented as depicted in Equation 2.15. The received signal $r(t)$ is given by Equation 2.16, and the cross-correlation $C_{rx}(\tau)$ can be expressed as shown in Equation 2.17. By relating this to the band-limited CIR $h_{BL}(\tau)$ in Equation 2.18, the sliding correlator channel sounder can extract valuable information about the channel's characteristics.

$$C_{rx}(\tau) = \int_{-\infty}^{+\infty} \overline{x(t)} \cdot r(t) dt \quad (2.14)$$

$$h(\tau) = \sum_{i=1}^N \alpha_i \delta(\tau - \tau_i) \quad (2.15)$$

$$r(t) = \sum_{i=1}^N \alpha_i x(t - \tau_i) \quad (2.16)$$

$$C_{rx}(\tau) \Big|_{multipath} = \sum_{i=1}^N \alpha_i C_x(\tau - \tau_i) \quad (2.17)$$

$$h_{BL}(\tau) = \frac{1}{V_0^2} C_{rx}(\tau) \quad (2.18)$$

The paper in [37] defines a set of design parameters. Table 2.1 reports only the mathematical tools used for the channel sounder design presented in this thesis. In the next sections, a brief introduction to these mathematical tools is provided.

Table 2.1: Sliding Correlator Channel Sounder Design Equations

Capability	Equation	Dependencies
Dynamic Range	$D_R \approx 16 \log_{10}(L)$ (dB)	$\gamma \geq 1.41L^{1.09}$, L
Temporal Resolution	$T_{res} = 1/f_c$	f_c
Maximum Multipath Delay	$\tau_{max} = L/f_c$	f_c , L
Maximum Path Length	$d_{max} = cL/f_c$	f_c , L

The sliding correlator function produces a distortion signal that leads to a degradation of its performance. In order to quantify the level of degradation, the *Dynamic Range* is used. The dynamic range is defined as the ratio between the clean signal and the distorting signal in dB scale. The ideal dynamic range $D_{R,ideal}$ is depicted in Equation 2.19, where L is the PN sequence length (see Section 2.2.1). $D_{R,ideal}$ represents the upper bound of the real dynamic range, and it is a useful tool as a reference.

$$D_{R,ideal} = 20 \log_{10}(L) \text{ dB} \quad (2.19)$$

The *Temporal Resolution* T_{res} provides information about how accurate the relative delay of a given multipath component can be resolved. T_{res} represents a lower bound, which means that it is not possible to measure two consecutive tones (see Section A.1) that have a time spacing shorter than T_{res} . Table 2.1 shows that T_{res} is equivalent to the chip time.

The *Maximum Resolvable Multipath Delay* is defined as an upper bound, assuming the speed of light c under a vacuum environment as the speed of the electromagnetic wave.

2.5 Investigation of Ionospheric Effects in the Planning of the AlfaCrux UHF Satellite Communication System

CubeSats have become a promising avenue for space research among universities due to their compact and cost-effective nature, utilizing cutting-edge Commercial-Off-The-Shelf (COTS) technologies. The University of Brasília's AlfaCrux mission showcases CubeSat telecommunications expertise, aiming to enable data exchange in remote areas through narrowband communication in the UHF amateur band, as for the proposed thesis. The article proposed by Arthur Amaral Ferreira et al. [24] analyzes how the ionosphere and space weather affect UHF satellite communication systems, particularly focusing on the AlfaCrux mission as a case study. It explores the effects of ionization levels on radio communication, such as Faraday rotation and ionospheric scintillation, and emphasizes the importance of understanding these phenomena for successful satellite missions, especially during transient space weather events like geomagnetic storms.

The article in [24] examines the effects of different factors on the UHF downlink channel for Low Earth Orbit (LEO) satellites, emphasizing the influence of the satellite's orbit. It shows that phenomena such as Faraday rotation and ionospheric scintillation are more intense in the equatorial zone than in the Arctic region.

Chapter 3

System Background and Tools

This Chapter covers all the aspects related to the Hyperspectral Small Satellite for Ocean Observation (HYPSO) FlatSat. Figure 5.1 depicts a high-level view of the deployed testbed for this project. In Appendix B, some basic concepts related to network theory are detailed.

3.1 Docker

The HYPSO group has to deal with various applications to handle each payload of the FlatSat. This often poses the problem of application compatibility with the platform. For example, an application may require specific dependencies on a Linux-based machine, which may necessitate updating the operating system to a compatible version. *Docker* [43] is a solution that can solve this issue to some extent by allowing the separation of the application from the platform on which it runs. This eliminates the need for developers to worry about configuring the dependencies for applications on different platforms, thereby reducing the time between code development and production.

Docker offers several objects such as images, containers, networks, volumes, and plugins. An *image* is a read-only template that provides instructions for creating a Docker container. A *Dockerfile* can be used to define the steps needed to create and run an image. Each instruction in the Dockerfile creates a layer in the image, and only the changed layers are rebuilt when the Dockerfile is modified and the image is rebuilt.

A *container* is a runnable instance and is defined by its image and any configuration options provided while creating or starting it. The isolation and security provided by Docker allow multiple containers to run simultaneously on a single host. The integration in this thesis of Docker is discussed in Appendix D.3, in which the building phase of the container used to create and run GNU Radio applications is detailed.

3.2 Software Defined Radio

The goal of the designers is to simplify the implementation of communication protocols [44], and measurement applications [11], [42] while providing researchers with the opportunity to test prototypes on distributed networks [45], [46]. To meet these specifications, it is necessary to design a transceiver capable of handling different scenarios. To accomplish this task, a framework with the following characteristics is required: *flexibility*, *reconfigurability* and *programmability* [47]. To this end, Software Defined Radio (SDR) is the technology that meets these requirements today. It is uncommon that universities and companies use SDRs in their satellites [10], [48].

SDR is a programmable transceiver with the capability of operating various wireless applications without the need to change or update the hardware. The main advantage of SDR is that radio components traditionally perform modulation, demodulation, filtering, and other signal processing tasks. The latter ones are implemented using software running on a general-purpose computer or specialized embedded system. This approach allows the radio to be reprogrammed and reconfigured using software, making it more flexible and adaptable to different communication protocols and environments. SDRs can operate over a wide range of frequencies, making them suitable for use in a variety of applications, such as Orthogonal Frequency-Division Multiplexing (OFDM) and Long Range (LoRa).

3.3 GNU Radio Companion

GNU Radio Companion (GRC) [49] is a Graphical User Interface (GUI) tool used for creating signal processing flowgraphs and designing Digital Signal Processing (DSP) systems, including SDR, using the GNU Radio framework. GNU Radio is a free and open-source software development toolkit that provides signal processing blocks to implement software-defined radios and other signal processing systems. The versatile nature of GNU Radio Companion has led to its adoption in various solutions pertaining to satellite communications, wherein it serves as an instrumental tool for managing the communication aspect [50]–[52].

With GNU Radio Companion, users can design and implement complex signal processing systems without writing extensive amounts of code. The tool can generate code in either Python or C++, to accommodate each application to its framework.

3.3.1 TOTEM SDR

The SDR selected for this project is the TOTEM Motherboard [53], [54] from Alén Space. It is composed of one unique board and its architecture is based on the Xilinx Zynq 7020 System On Chip (SoC) and the AD9364 Radio Frequency (RF) Wideband



Figure 3.1: TOTEM SDR.

Transceiver [55] from Analog Devices, with a tunable Low Noise Amplifier (LNA) gain from 0 to 73 dB in manual mode. The TOTEM SDR includes an embedded Linux system, leading to the possibility to remote access via Secure Shell (SSH) [10]. The RF frequency can be tuned between 70 MHz and 6 GHz, capable to handle up to 56 MHz of bandwidth. Furthermore, the board is equipped with three RX ports and two TX ports. It is equipped with Ethernet, Universal Asynchronous Receiver / Transmitter (UART) and Joint Test Action Group (JTAG) interfaces for debugging and testing. For communication with the satellite bus, it can be used either Controller Area Network (CAN) or Inter-Integrated Circuit (I2C) interface. In Tables 3.2 and 3.1 are shown the front-end capabilities [53].

Table 3.1: TOTEM SDR — RF Transmission characteristics.

Symbol	Description	Min	Typical	Max	Unit
P_{IN_TX}	Power input (TX)	-	5	13	dBm
P_{OUT_TX}	Power output (ANT)	-	30	-	dBm
Frequency	Frequency range (v. 402 MHz)	395	-	410	MHz
Frequency	Frequency range (v. 435 MHz)	430	-	440	MHz

Due to the implementation of an embedded Linux system, different programming languages can be used, for instance C, C++ and Python [54]. GNU Radio was chosen for creating new applications. Applications, also known “flowgraphs”, created using GNU Radio can be tested either in a simulation environment or with real RF hardware. To enable the use of transceivers in flowgraphs, a set of blocks has been developed. These blocks can receive or transmit samples and are referred to as source

Table 3.2: TOTEM SDR — RF Reception characteristics.

Symbol	Description	Min	Typical	Max	Unit
P _{IN_RX}	Power input (RX)	-	-	-15	dBm
Gain	Power gain	-	19	-	dB
Frequency	Frequency range (v. 402 MHz)	395	-	410	MHz
Frequency	Frequency range (v. 435 MHz)	430	-	440	MHz
NF	Noise Figure	1.28	1.60	1.92	dB
P _{OUT_1dB}	Output 1 dB Compression	-	11.5	-	dBm

and sink blocks. The blocks are designed to interface with the transceiver hardware through the underlying SoapySDR client API.

SoapySDR

SoapySDR [56] is an open-source framework for interfacing various SDR hardware platforms. It provides a consistent Application Programming Interface (API) that allows one to build software applications without the need to know the specifics of each device’s hardware or software interface.

SoapySDR provides a set of drivers and libraries that abstract the low-level details of different SDR hardware platforms, making it easier for developers to write SDR applications that can work with multiple devices. It supports a wide range of SDR platforms, including popular devices such as the Universal Software Radio Peripheral (USRP), HackRF, RTL-SDR and TOTEM Motherboard [54], and was used in different contexts such as mobile radio networks [57], [58].

3.3.2 USRP-2901

USRP-2901 [59] is a high-performance SDR platform developed by the National Instruments Corporation. It features a high-speed Universal Serial Bus (USB) 3.0 interface and supports a wide range of frequency bands. In Tables 3.3b and 3.3a are shown the characteristics related to the front-end.

Both the SDR devices are used and discussed in this thesis. Instead of the TOTEM SDR, the USRP-2901 is not standardised for satellite implementations, which makes it only applicable for terrestrial applications. In Chapter 5, the implementation in the testbed of both the SDRs is detailed. Moreover, it is discussed the calibration and characterization of the devices. The last step concerns the comparison between TOTEM SDR and USRP-2901, which unexpectedly shows a better performance of the latter.



Figure 3.2: USRP-2901 SDR.

(a) USRP-2901 - RF Transmission characteristics.

Symbol	Description	Min	Typical	Max	Unit
Frequency	Frequency range	0.07	-	6	GHz
Frequency	Frequency step	-	-	1	kHz
P_{OUT}	Maximum output power	-	-	20	dBm
Gain	Gain range	-	-	89.75	dB
Gain	Gain step	-	0.25	-	dB
BW	Maximum bandwidth	-	-	56	MHz

(b) USRP-2901 - RF Reception characteristics.

Symbol	Description	Min	Typical	Max	Unit
Frequency	Frequency range	0.07	-	6	GHz
Frequency	Frequency step	-	-	1	kHz
Gain	Gain range	-	-	76	dB
Gain	Gain step	-	1	-	dB
P_{IN}	Maximum input power	-	-	-15	dBm
NF	Noise Figure	5	-	7	dBm
BW	Maximum bandwidth	-	-	56	MHz

Table 3.3: RF characteristics of USRP-2901.

Chapter 4

Phase One: Matlab Simulator

The initial phase of the project encompasses the creation of a dedicated Matlab simulator tailored for the Downlink (DL) channel in Low Earth Orbit (LEO) satellites operating within the Ultra High Frequency (UHF) band. The objective is to provide a comprehensive understanding of the simulator's functionality, its overall structure, the flow of information within the simulation chain, and the inclusion of various models. All the implemented models and data are sourced from relevant literature, and the obtained results are presented and analyzed. In Appendix C, the Matlab code of the simulator is detailed.

4.1 The behaviour of the simulator

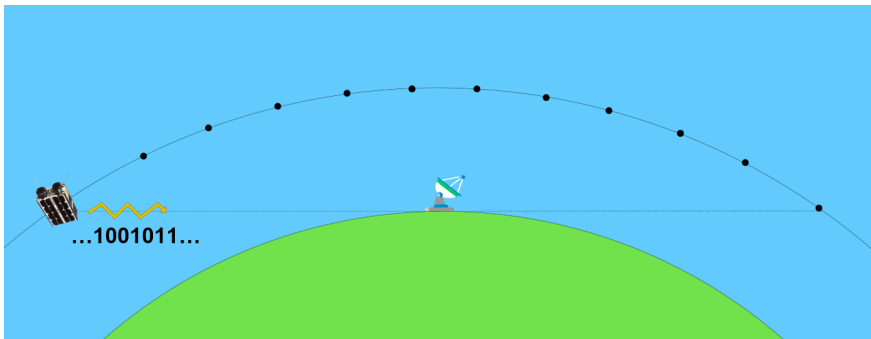


Figure 4.1: Example of a possible scenario for DL channel and LEO satellites.

Figure 4.1 shows a possible scenario for downlink channel and LEO satellites that is implemented with the Matlab simulator. The two main components are the satellite and the ground station. The satellite has visibility with the ground station in a range of elevation angles from 0° to 180° degrees. The elevation angle is defined as the angle between the astronomical horizon (i.e. the horizontal plane where the satellite is either at 0° or 180°) and the satellite. For instance, when the satellite is at elevation angle equal to 0° , the scenario is the one shown in Figure 4.1. Assuming the

height of the ground station h_{GS} is negligible ($h_{GS}/R_E \ll 1$, R_E Earth’s radius), we can assume that astronomical and real horizons are the same. From now on, the visibility region is referred to as a *pass*.

In Figure 4.1, black points highlighted along the pass correspond to satellite positions where a measurement phase is carried out, i.e. where the satellite transmits a known signal towards the ground station. These positions are associated with a value of elevation angle. It is worth noting that the satellite is “static” during the measurement phase. This is an important assumption since the whole simulator is based on that. To do so, both the time needed to transmit the signal T_{TX} and the *coherence time* T_{COH} (see Section A.1.3) must be considered. Analytically, the relation that must be guaranteed is depicted in Equation A.1. The coherence time describes how fast the channel varies in time. It is not possible to determine a single coherence time for all the LEO satellites, because of the different orbits that can be chosen. Moreover, it is not known a priori the distribution of the bubble of plasma around the ionosphere, how fast they change over time and how big they are. For an effective channel sounder capable of detecting channel variability, two key factors need to be tailored: the time interval required to send the signal to the ground station and the number of measurement phases needed along the pass. The more measurement phases, the better the precision in time.

4.2 Chain flow

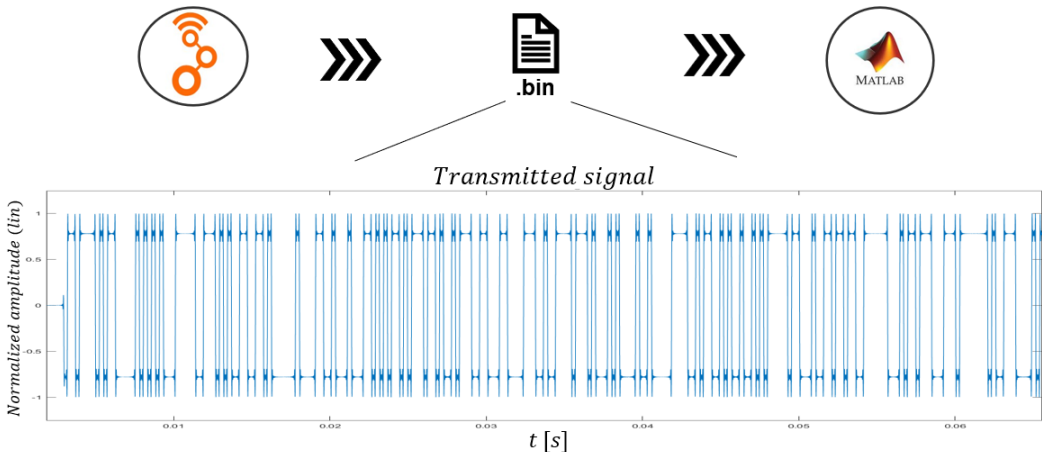


Figure 4.2: The chain flow.

The chain flow is shown in Figure 4.2. The main components are the GNU Radio application and the Matlab simulator.

The GNU Radio application is responsible to generate the baseband signal. The output is a binary file that is manually forwarded to the Matlab simulator.

4.3 The GNU Radio application: PN sequence generator

Figure 4.3 shows the GNU Radio application used for the Matlab simulator. In summary, the objective of the application is to generate a baseband signal that represents a Binary Phase-shift Keying (BPSK)-modulated pseudo-noise maximal sequence. Each sample generated by the program is stored in a binary file until the program concludes. Positioned in the upper-left side of Figure 4.3, a collection of variables and parameters is defined. The following list provides an introduction to the various blocks involved in the application:

1. **Galois Linear Feedback Shift Register (GLFSR) Source:** it is used to generate a binary GLFSR (see Section 2.2.3). The *Degree* of the shift register is 8, meaning that the maximum length of the pseudo-noise sequence is $L = 2^8 - 1 = 255$ bits (a bit corresponds to a chip);
2. **Throttle:** it is used as a rate regulator, keeping the chip rate of the GLFSR at a specified value.
3. **Head:** it is used to limit the execution of the application. Indeed, it ends the program after receiving 255 items as input, i.e. the whole sequence length;
4. **Constellation Modulator:** it is used to BPSK-modulate the sequence as input. The chosen Sample-per-Symbol (sps) is 16, in order to have a more accurate reproduced waveform and reduce the occupied bandwidth. The relation between sample rate (R_{sample}) and symbol rate (R_{symbol}) is $R_{\text{symbol}} = R_{\text{samples}}/sps$. The GNU Radio block has incorporated a Root-Raised-Cosine (RRC) filter, with a roll-off factor (named *Excess BW* inside the block) of 0.35;
5. **File Sink:** it is used to store each sample into a binary file. The name of the file includes the main features of the virtual transmitter. An example of file name is `tx_100k_500k_437M_20dBm_30dB_16_10.bin`, where:
 - 100k: chip rate;
 - 500k: sample rate;
 - 437M: carrier frequency
 - 20dBm: Radio Frequency (RF) power;
 - 30dB: Low Noise Amplifier (LNA) gain;
 - 16: sps;
 - 10: number of repetitions (window) of the same sequence in a row.

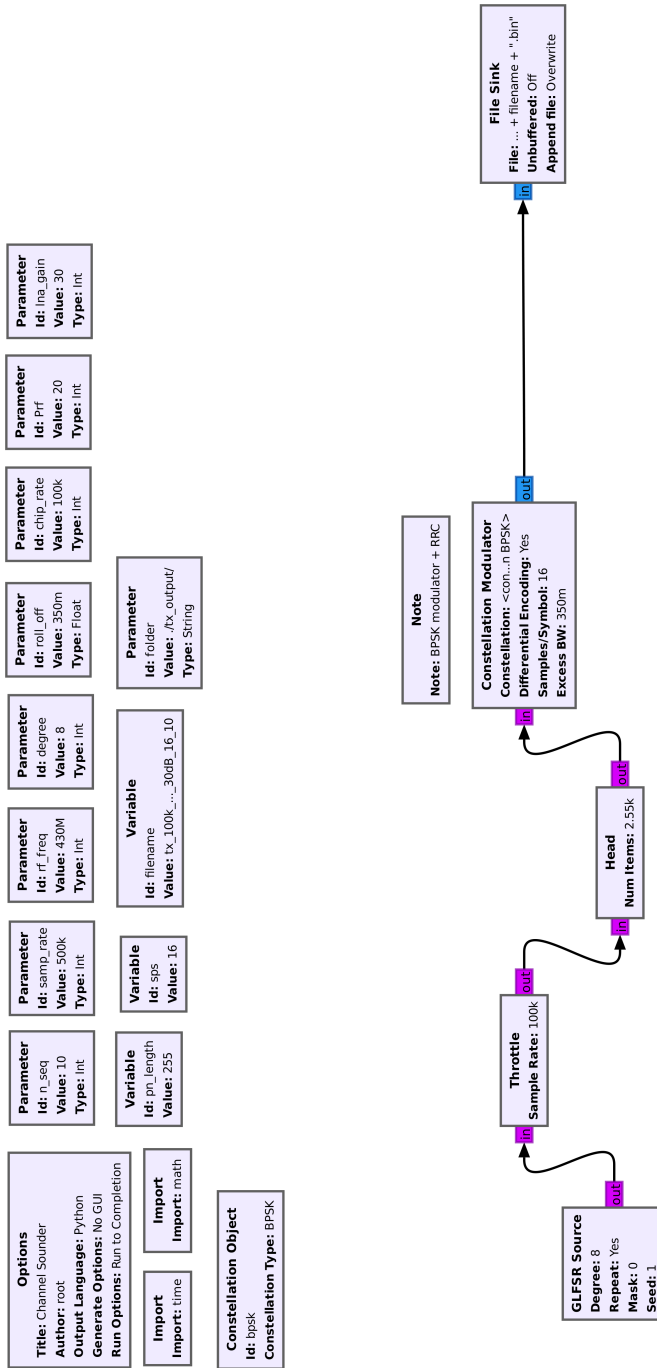


Figure 4.3: The GNU Radio application for generating the binary file.

4.4 Structure of the simulator

Figure 4.4 shows a high-level representation of the transmission chain performed by the simulator. Moreover, Figure 4.5 shows the logical structure of the Matlab simulator. Each entity will be discussed in a dedicated section.



Figure 4.4: Simplified communication chain.

The structure is described as follows. *config.m* and *main.m* are located in the main directory, which are described shortly. The five folders have the following purposes:

- **config/**: it contains system variable configurations;
- **Transmitter/**: it contains the simulation of the transmitter entity (i.e. the satellite), including attenuation and gain values of the signal generated by the GNU Radio application (see Section 4.3);
- **Channel/**: it contains the DL channel entities considered for the UHF band and LEO satellites;
- **Receiver/**: it contains the simulation of the receiver entity (ground station), including attenuation values, amplification, and post-processing functions;
- **utils/**: it contains common functions utilized by the transmitter, channel and receiver.

In *config.m*, a user is able to set the system variables, such as the height of the satellite, the carrier frequencies and the elevation angles for each measurement campaign. The variables are organized into groups based on their relevance to either the transmitter (satellite), channel, or receiver (ground station) entities. These are saved permanently into three separated MAT-files under the directory **config/**, i.e. *Transmitter_config.mat*, *Channel_config.mat* and *Receiver_config.mat*.

Once the system variables have been appropriately stored, the user can execute the *main.m* program. This program is responsible for reading the MAT-files located within the **config/** directory. Furthermore, the *main.m* program sequentially executes *mainTX.m*, *mainChannel.m*, and *mainRX.m* programs, which are located under **Transmitter/**, **Channel/**, and **Receiver/** directories, respectively. The resulting outputs are saved in dedicated MAT-files, namely *TX.mat*, *CH.mat*, and *RX.mat*, which are stored in the aforementioned directories.

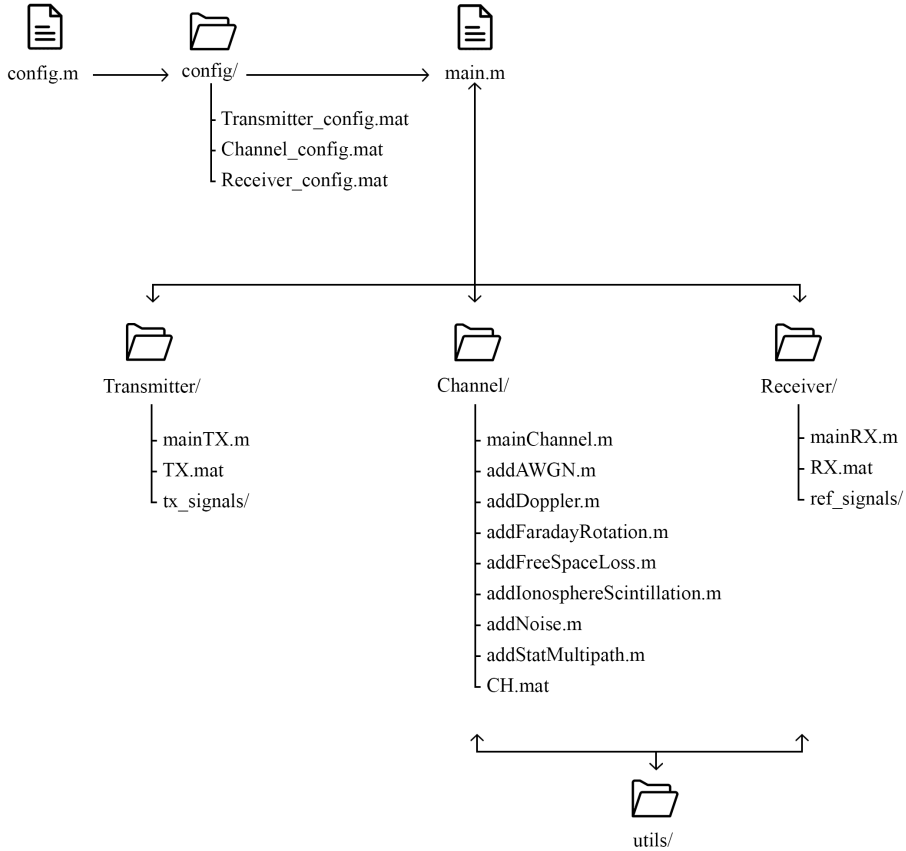


Figure 4.5: The logical structure of the Matlab simulator.

4.5 Transmitter implementation

This entity is responsible to read the samples from one of the outputs of the GNU Radio application and convert them into a readable format for Matlab. A cell array contains the baseband signals that is forwarded to the channel entity. Since the signal that is generated by the GNU Radio application is normalized, the RF power and the LNA gain are included. Each cell of the array corresponds to a signal with a well-defined carrier frequency. In this scenario, users are granted the freedom to determine the allocation of bands and select the specific signals to transmit within each allocated band. More details can be found in Listing C.1.

4.6 Channel model entities

This Section focuses on the implementation of the various channel entities. Initially, a concise overview is provided, referencing previous sections where detailed discussions on relevant topics have taken place. Subsequently, the implementation methodology is delineated. The entities that are considered are the following:

- Additive White Gaussian Noise (AWGN);
- Free-space path loss;
- Doppler effect;
- Multipath effect;
- Faraday rotation;
- Ionospheric scintillation.

The main program is responsible to include the channel entities in the transmitted signal. The algorithm has two for-loop. The main one is used to iterate for each elevation angle decided by the user (one elevation angle corresponds to a measurement phase). The inner for-loop is used to iterate for each carrier frequency defined by the user. All the allocated carrier frequencies are stored in the array `fcs`. The final result is stored in the cell array and sent to the receiver entity. More information can be found in Listing C.2.

4.6.1 AWGN implementation

Two algorithms are developed in order to add thermal noise to the transmitted signal: `addNoise.m` and `addAWGN.m`. The first one is simple and it needs just the Signal-to-Noise Ratio (SNR) as input to derive the noise power. This is used when the user knows a priori the quality of the signal, without knowing all the noise figures and temperatures of the system. The code is discussed in Section 4.6.1. The second one is more sophisticated and it is based on [60]. It is discussed in Section 4.6.1.

addNoise.m

The algorithm receives the SNR as input and it computes the noise power level, depending if the signal is complex or real. The user can check whether the passed SNR corresponds to the one obtained by the function. Listing C.3 shows the Matlab implementation.

addAWGN.m

The code adds the thermal noise quantity to the transmitted signal. The function holds for the downlink only.

The first element that is computed is the antenna noise temperature T_A and it is a result of losses incurred in the radio path and associated with the physical structure of the device. This noise temperature is obtained by convolving the brightness temperature of a radiating body in a specific direction with the radiation pattern of the antenna, which incorporates its gain. The complete formula for the antenna noise temperature [61] is shown in Equation 4.1, where T_b and G are the brightness temperature and radiating pattern of the antenna in a certain direction (θ, ϕ) .

$$T_A = \frac{1}{4\pi} \int \int T_b(\theta, \phi) G(\theta, \phi) \sin(\theta) d\theta d\phi \quad (4.1)$$

An approximated formula can be found on [62]. Upon assuming an antenna efficiency of η equal to 70%, Equation 4.1 can be simplified as a sum of three different antenna noise temperatures (see Equation 4.2). These terms represent the noise contributions stemming from the main lobe T_A^{ML} , side lobes T_A^{SL} , and back lobe T_A^{BL} of the antenna.

$$\begin{cases} T_A = T_A^{ML} + T_A^{SL} + T_A^{BL} \\ T_A^{ML} = T_{sky} \cdot \eta \\ T_A^{SL} = T_{sky} \cdot 2/3 \cdot (1 - \eta) \\ T_A^{BL} = T_O \cdot 1/3 \cdot (1 - \eta) \end{cases} \quad (4.2)$$

Then, the environment temperature T_m is computed by considering the approximated formula in Equation 4.3 formulated by [63], where T_s is the surface temperature.

$$T_m = 1.12 \cdot T_s - 50 \text{ K} \quad (4.3)$$

Moreover, let us consider the composite temperature T_{comp} . The composite temperature represents the superposition of all the noise entities of the system. Figure 4.6 shows the reference receiver diagram. Assuming a signal bandwidth B , the composite noise power can be derived as follows:

$$N = \frac{kT_{L2}B}{Loss_2} + \frac{kT_{LNA}BG_{LNA}}{Loss_2} + \frac{k(T_{L1} + T_A)BG_{LNA}}{Loss_1 Loss_2} \quad (4.4)$$

And can be written in the new form:

$$\begin{aligned}
 N &= kB \left(T_{L2} \cdot \frac{Loss_1}{G_{LNA}} + T_{LNA} Loss_1 + T_{L1} + T_A \right) \frac{G_{LNA}}{Loss_1 Loss_2} \\
 &= k \cdot B \cdot T_{SYS} \cdot G_{TOT} \\
 &= N_0 \cdot B
 \end{aligned} \tag{4.5}$$

where T_{SYS} is the system temperature $T_{SYS} = T_{comp} + T_A$, N is the spectral noise power and N_0 is the spectral noise power density. Subsequently, the SNR is evaluated by computing the power of the passed signal to this algorithm by using the function *powerCalculator.m* present under the folder *utils/*. Finally, the SNR is passed to the function *addNoise.m* explained in Section 4.6.1. Listing C.4 shows the code in detail.

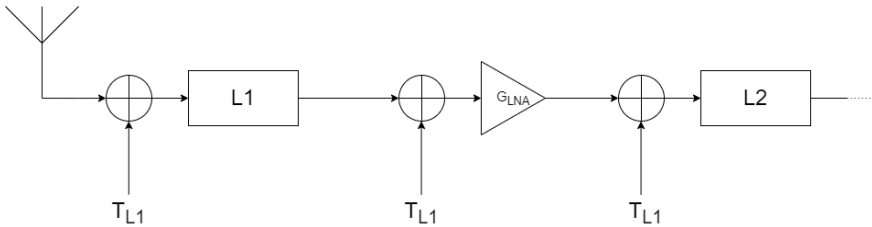


Figure 4.6: Example of a receiver chain diagram, where L1 is the loss line from the antenna to the LNA, G_{LNA} is the LNA gain and L2 is the loss line from the LNA to the rest of the circuit.

4.6.2 Free-space path loss

The algorithm adds the amount of attenuation to a generic input signal. The final formula in Equation 4.14 is derived by referring to the geometry problem shown in Figure 4.7, and the solution is discussed shortly. It is assumed that the Earth is a perfect sphere and the satellite's orbit is a perfect circle. For more details, Listing C.5 depicts the implemented Matlab code.

The objective is to find a formula for the distance between the ground station and the satellite in the function of the elevation angle θ , the Earth radius R_E and the satellite height h , i.e. $r = r(\theta, R_E, h)$, where r is the satellite-to-ground station distance (see the red vector in Figure 4.7).

By applying the cosine rule to the triangle formed by the points P_E , P_G and P_S , it is possible to write Equation 4.6.

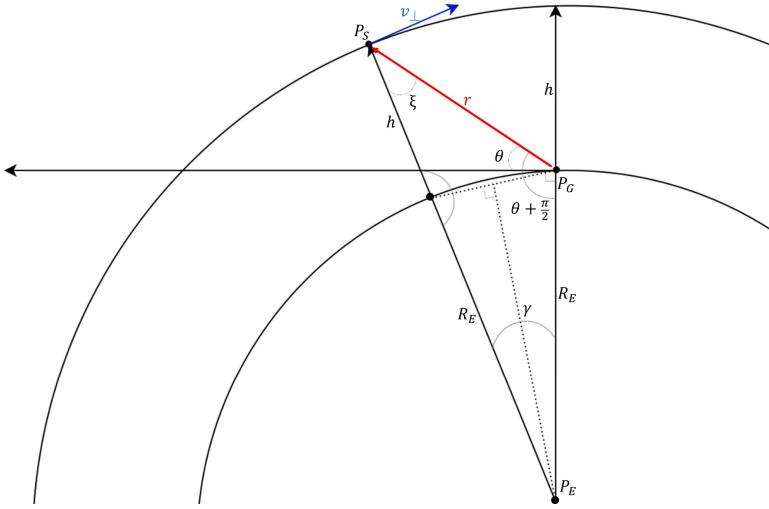


Figure 4.7: Geometry problem of the distance between the ground station and the satellite, for $\theta \in [0, \pi/2]$. P_S , P_G and P_E are the satellite, ground station and Earth's center positions respectively.

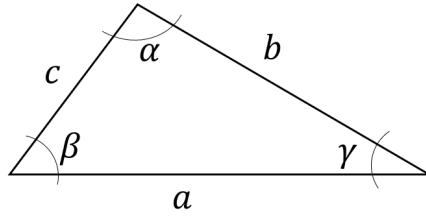


Figure 4.8: Example of a triangle.

$$a^2 = b^2 + c^2 - 2 \cdot b \cdot c \cdot \cos(\alpha) \quad (4.6)$$

By using the variables in Figure 4.7, it yields Equation 4.7.

$$\begin{cases} a = r \\ b = R_E \\ c = R_E + h \\ \alpha = \gamma \end{cases} \Rightarrow r^2 = R_E^2 + (R_E + h)^2 - 2R_E(R_E + h)\cos(\gamma) \quad (4.7)$$

Now, the problem is to find $\gamma = \gamma(R_E, h, \theta)$. It can be assumed that when the elevation angle θ increases, then γ decreases. Moreover, when the satellite is at the zenith (i.e. when $\theta = 90^\circ$), then $\gamma = 0$. The sum of all the internal angles of the highlighted triangle is the following:

$$\xi + [\pi/2 + \theta] + \gamma = \pi \Leftrightarrow \xi + \theta + \gamma = \pi/2 \quad (4.8)$$

Equation 4.9 shows the sine rule:

$$\frac{b}{\sin(\beta)} = \frac{c}{\sin(\gamma)} = \frac{a}{\sin(\alpha)} \quad (4.9)$$

By applying Equation 4.9 to the same triangle in Figure 4.8, it yields:

$$\begin{aligned} \frac{R_E}{\sin(\xi)} = \frac{R_E + h}{\sin(\theta + \pi/2)} &\Rightarrow \sin(\xi) = \frac{R_E}{R_E + h} \sin(\theta + \pi/2) \\ &= \frac{R_E}{R_E + h} \cos(\theta) = \beta(\theta, R_E, h) \end{aligned} \quad (4.10)$$

Hence, by using the result in Equation 4.10 with Equation 4.8, it yields Equation 4.11.

$$\begin{aligned} \xi + \theta + \gamma = \pi/2 &\Rightarrow a \sin(\beta(\theta, R_E, h)) + \theta + \gamma = \pi/2 \\ &\Rightarrow \gamma = \pi/2 - [\theta + a \sin(\beta(\theta, R_E, h))] \end{aligned} \quad (4.11)$$

By using Equation 4.11 in Equation 4.7, it yields:

$$\begin{cases} r = \sqrt{R_E^2 + (R_E + h)^2 - 2R_E(R_E + h)\sin(B(\theta, R_E, h))} \\ B(\theta, R_E, h) = \theta + a \sin\left(\frac{R_E}{R_E + h} \cos(\theta)\right) \\ \theta \in [0, \pi/2] \end{cases} \quad (4.12)$$

To validate Equation 4.12 for $\theta \in [\pi/2, \pi]$, let us consider the similar scenario shown in Figure 4.9. Let us define $\theta' = \pi - \theta$, $\theta \in [\pi/2, \pi]$ shown in Figure 4.9.

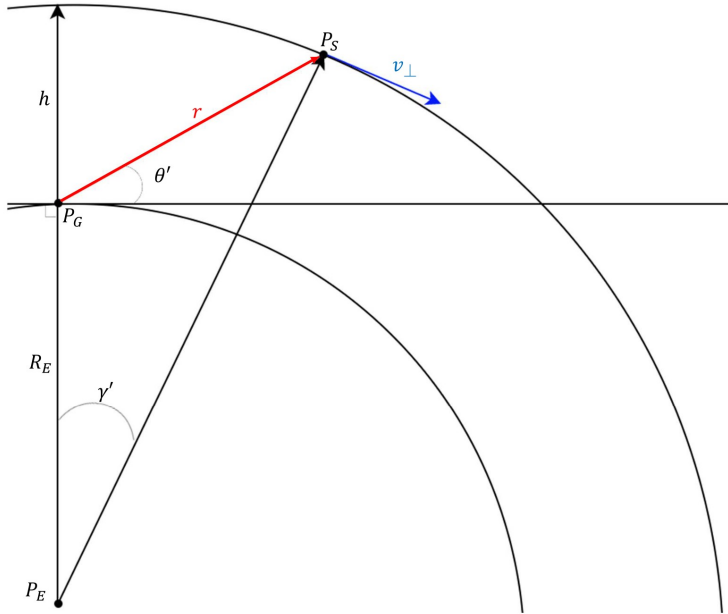


Figure 4.9: Geometry problem of the distance between the ground station and the satellite, for $\theta \in [\pi/2, \pi]$.

$$\begin{aligned}
 B(\theta', R_E, h) &= B(\pi - \theta, R_E, h) \\
 &= \pi - \theta + a \sin \left(\frac{R_E}{R_E + h} \cos(\pi - \theta) \right) \\
 &= \pi - \left[\theta + a \sin \left(\frac{R_E}{R_E + h} \cos(\pi - \theta) \right) \right] \\
 &= \pi - B(\theta, R_E, h)
 \end{aligned} \tag{4.13}$$

Since $B(\theta, R_E, h)$ is inside a sine function, it is possible to write $\sin(\pi - B(\theta, R_E, h)) = \sin(B(\theta, R_E, h))$, and this proves that Equation 4.12 holds for $\theta \in [0, \pi]$. The final result is shown in Equation 4.14.

$$\begin{cases} r = \sqrt{R_E^2 + (R_E + h)^2 - 2R_E(R_E + h)\sin(B(\theta, R_E, h))} \\ B(\theta, R_E, h) = \theta + a \sin \left(\frac{R_E}{R_E + h} \cos(\theta) \right) \\ \theta \in [0, \pi] \end{cases} . \tag{4.14}$$

Now, the derivation of the free-space path loss is trivial and it is shown in

Equation 4.15, where $Loss_{FS}$ is the free-space path loss (see Section A.4) and λ is the wavelength equal to $\lambda = c/f_c$, c is the speed of light in vacuum and f_c is the carrier frequency.

$$Loss_{FS} = \left(\frac{4\pi r}{\lambda} \right)^2 \quad (4.15)$$

Figure 4.10 shows an example of free-space path loss for elevation angle $\theta \in [0, \pi]$ and satellite altitude $h = 500 \text{ km}$. The x-axis represents the time instant. Indeed, it is possible to correlate θ and t . This proof is discussed in Section 4.6.3. It is visible how strong the impact of the free-space path loss is on the signal power. In fact, when the elevation angle is either 0 or π , the path loss is at its maximum, with an attenuation in the order of 300 dB. For this reason, the link budget design is an important aspect to take into account.

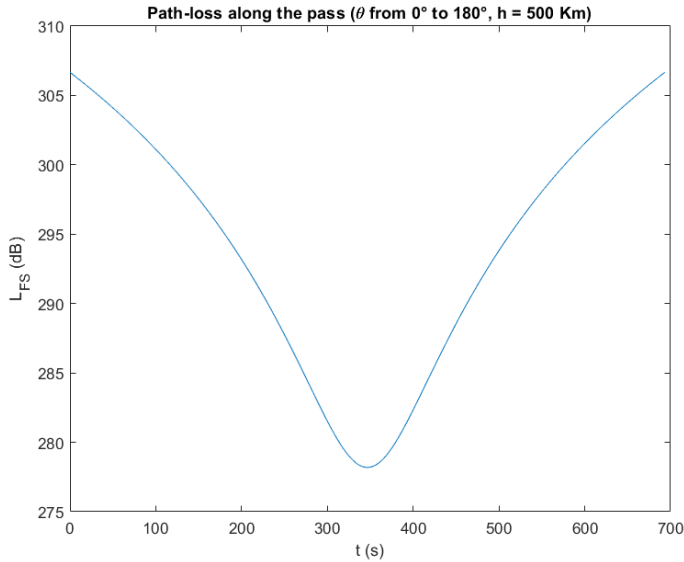


Figure 4.10: Example of free-space path loss for $\theta \in [0, \pi]$ and satellite altitude $h = 500 \text{ km}$.

4.6.3 Doppler effect

The algorithm generates the Doppler shift to a generic input signal. The resulting formula is obtained starting from Equation 4.12, and the implemented algorithm is shown in Listing C.6. The general Doppler shift formula is shown hereafter:

$$f_D = -f_c \cdot \frac{v_{rel}}{c} \quad (4.16)$$

where f_D is the Doppler shift, f_c is the carrier frequency and v_{rel} is the relative speed between the satellite and the ground station. This speed can be obtained by applying the derivative over time to the satellite-ground station distance, shown in Equation 4.17.

$$v_{rel} = \frac{d}{dt}r(t) \quad (4.17)$$

Let us consider the usual scenario depicted in Figure 4.7. v_{\perp} is the satellite speed, and it is known a priori.

$$v_{\perp} = \sqrt{\frac{G \cdot M_E}{R_E + h}} \approx 7.4 \text{ km/s} \quad (4.18)$$

The angular speed ω can be expressed as depicted in Equation 4.19.

$$\omega = \frac{v_{\perp}}{R_E + h} \quad (4.19)$$

Let us define a new angle ϵ such that the sum with ϵ and γ gives γ_{max} , i.e. the maximum value of γ when the satellite starts the visibility region.

$$\begin{cases} \epsilon + \gamma = \gamma_{max} \\ \epsilon = \epsilon(t) = \epsilon_{in} + \omega t = \omega t, \epsilon_{in} = 0 \end{cases} \quad (4.20)$$

It yields:

$$\gamma = \gamma_{max} - \omega t, \theta \in [0, \pi/2] \quad (4.21)$$

So, it is possible to merge Equation 4.11 and 4.21, and it produces:

$$\gamma = \pi/2 - [\theta + a \sin(\beta(\theta, R_E, h))] = \gamma_{max} - \omega t \quad (4.22)$$

This means that by knowing the elevation angle θ , it is possible to derive the instant of time t of the satellite's position. It is possible to include the result in Equation 4.22 into Equation 4.12, and the outcome is shown in Equation 4.23.

$$\begin{aligned} r &= \sqrt{R_E^2 + (R_E + h)^2 - 2R_E(R_E + h) \sin(\gamma_{max} - \omega t)} \\ &\downarrow \\ \frac{dr}{dt} &= \frac{-2R_E(R_E + h)(-\sin(\gamma_{max} - \omega t))(-\omega)}{2\sqrt{R_E^2 + (R_E + h)^2 - 2R_E(R_E + h) \sin(\gamma_{max} - \omega t)}} \end{aligned} \quad (4.23)$$

The final equation for the Doppler shift is depicted in Equation 4.24.

$$\left\{ \begin{aligned} f_D &= \frac{f_c}{c} \cdot \frac{\omega R_E(R_E + h) \sin(\gamma_{max} - \omega t)}{\sqrt{R_E^2 + (R_E + h)^2 - 2R_E(R_E + h) \sin(\gamma_{max} - \omega t)}} \\ \omega &= \frac{v_{\perp}}{R_E + h} \\ v_{\perp} &= \sqrt{\frac{G \cdot M_E}{R_E + h}} \approx 7.4 \text{ km/s} \\ \gamma_{max} &= \gamma(\theta_{min}) = \pi/2 - [\theta_{min} + a \sin(\beta(\theta_{min}, R_E, h))] \\ \theta &\in [0, \pi/2] \end{aligned} \right. \quad (4.24)$$

The user makes the choice of θ_{min} . As for the free-space path loss, it must be verified that the formula holds for all the elevation angle values. The scenario is the same depicted in Figure 4.9. When $\gamma_{max} = \omega t$, the elevation angle $\theta = \pi/2$. In case $\theta > \pi/2$, then $\gamma' = \omega t - \gamma_{max} > 0$, where $\gamma' = -\gamma$, $\gamma, \gamma' \in [0, \pi/2]$.

Therefore, it is quite obvious that for $\gamma' \in [0, \pi/2]$, the sine in Equation 4.24 becomes negative since it is an odd function, and the cosine remains the same since it is an even function. Referring to Figure 4.1, it is possible to conclude that when the elevation angle is between 0 and $\pi/2$, the signal frequency experience a blue-shift (i.e. the f_D is positive. The result is an increase of the signal frequency), since the source goes closer to the receiver. Instead, when the elevation angle is between $\pi/2$ and π , the signal frequency experience a red-shift (i.e. the f_D is negative. The result is a decrease in the signal frequency).

It is possible to derive the pass time interval $[0, t_{max}]$ by using Equations 4.21 and 4.11.

$$\begin{cases} \gamma_{max} = \pi/2 - [\theta_{min} + \text{asin}(\beta(\theta_{min}, R_E, h))] \\ \gamma_{min} = \pi/2 - [\theta_{max} + \text{asin}(\beta(\theta_{max}, R_E, h))] \\ \gamma(t) = \gamma_{max} - \omega t \end{cases} \quad (4.25)$$

It yields:

$$t_{max} = \frac{1}{\omega} [\theta_{max} - \theta_{min} + \text{asin}(\beta(\theta_{max}, R_E, h)) - \text{asin}(\beta(\theta_{min}, R_E, h))] \quad (4.26)$$

Figure 4.11 shows the results of Equation 4.24 for different satellite altitudes h . The results are compliant with the scenario taken into consideration. Indeed, the Doppler shift remains positive until it reaches the azimuth position with respect to the ground station, and after it starts to be negative. The decreasing behavior tells us that the satellite comes closer to the ground station, but this approach tends to be slower and slower until the elevation angle is $\pi/2$. The Doppler rate is an important parameter because it describes how fast the Doppler shift changes. This influences the coherence time, as discussed in Section A.1.3.

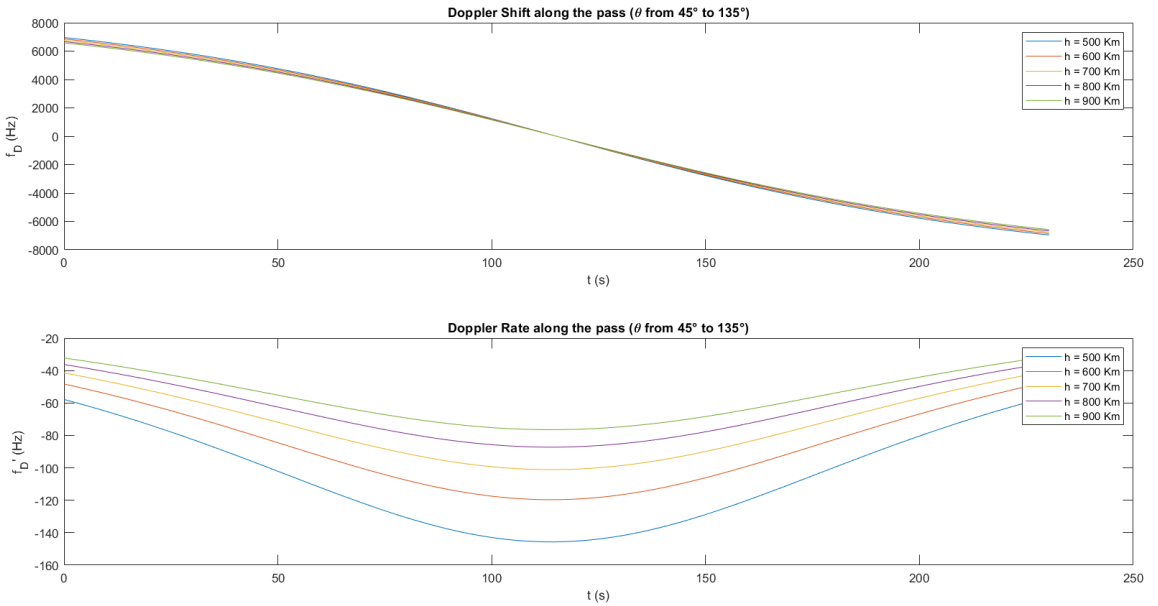


Figure 4.11: Behavior of the Doppler shift and Doppler rate in function of the time and altitude of the satellite.

After estimating the Doppler shift, it is necessary to apply it to the passed signal. Line 15 of Listing C.6 shows how the frequency shift is performed. The formula that is applied is depicted in Equation 4.27.

$$x(t)_{f.s.} = x(t) \cdot e^{j2\pi f_{shift}t} \quad (4.27)$$

where $x(t)$ is the non-frequency-shifted signal, f_{shift} is the amount of shift and $x(t)_{f.s.}$ is the frequency shifted signal. This means that a frequency shift is nothing more than multiplying a phasor to the passed signal, changing its phase in time. In the context of Matlab, the time is represented by the array $(0:\text{length}(X) - 1)/\mathbf{fs}$ as depicted in line 15 of Listing C.6, where \mathbf{fs} is the sample rate f_s . Hence, a general instant of time t_i can be written as reported in Equation 4.28, where n_i takes values between 0 and the length of the passed vector X minus 1 (i.e. $(0:\text{length}(X) - 1)$).

$$t_i = n_i/f_s \quad (4.28)$$

4.6.4 Multipath effect

The algorithm is responsible to generate the multipath effect. It is divided into two parts: the first one is responsible to make a discrete multipath channel and the second one to make a Rician fading channel model. In Sections 4.6.4 and 4.6.4, the choices of the two models are motivated. Listing C.7 shows the Matlab implementation.

Firstly, the propagation delay in vacuum is computed in function of each elevation angle passed inside the function. This delay is added to the excess delay array, and it takes into account both the group delay of each multipath due to the electron content inhomogeneity (see Section 2.1.1) and the length of each path. The excess delays are manually chosen and defined in *config.m* file.

Discrete multipath effect

Figure 4.12a shows a possible scenario of discrete multipath effect for the downlink channel. Even though this effect is not caused by the ionosphere interaction, it must be considered as part of the channel. For example, the ground station has the potential to receive signals that are reflected from objects, for example airplanes and mountains. The different composition and shape of these objects affect the way the radio wave is split into reflected and refracted components (see Figure 4.13)

The electromagnetic characteristics of a medium are determined by three entities: permittivity ϵ , conductivity γ and permeability μ . Given that the medium under consideration is air, its conductivity is zero. Instead, μ and ϵ can change along the

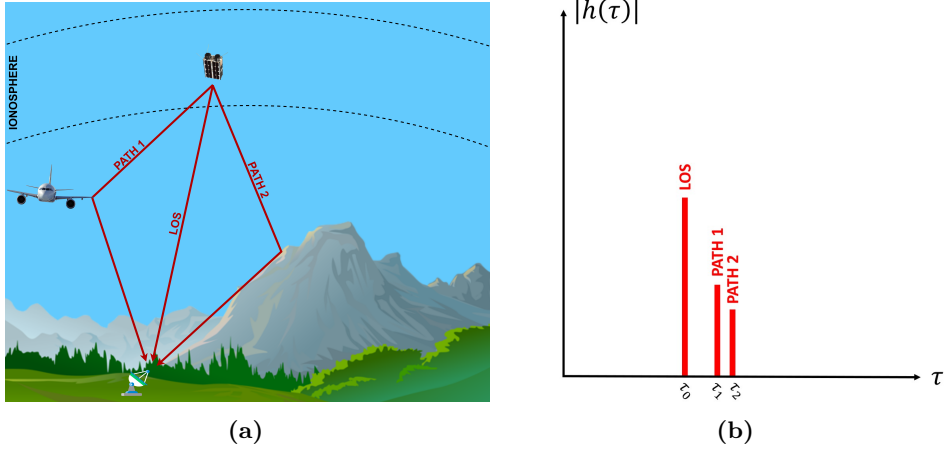


Figure 4.12: Example of discrete multipath scenario (a) and the corresponding Channel Impulsive Response (CIR) (b).

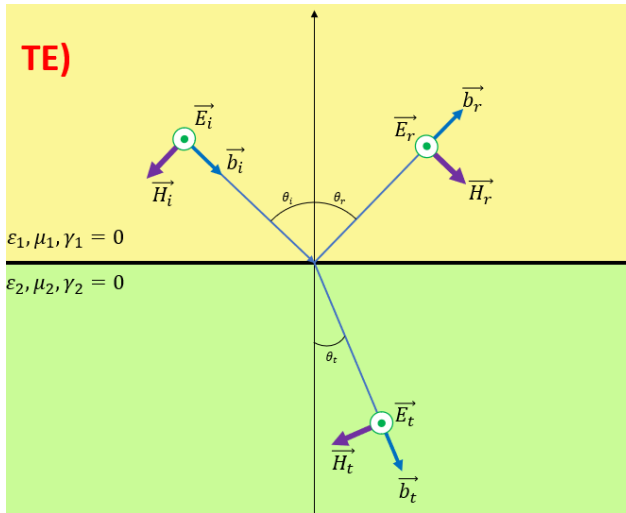


Figure 4.13: Example of refraction and reflection of a Transverse electromagnetic (TE) mode wave .

propagation path. When the radio wave passes through a medium with different permittivity and permeability values, the signal is split into reflected and refracted components. These are indicated with r and t respectively in Figure 4.13. Different mediums can be present along the path. The capability of a ground station to detect different secondary paths depends on its radiation pattern as well (see Section A.2.2). Indeed, the aperture of the main lobe is important to know how efficient the ground station antenna is: the more directive is the antenna, the lower the probability to

detect secondary paths, as shown in Figure A.5.

Considering the scenario depicted in Figure 4.12a, a possible CIR is shown in Figure 4.12b. Each spike represents a path received by the ground station. The first spike represents the Line of Sight (LOS), which is the strongest and fastest signal that reaches the ground. The others are the secondary paths, generated by reflection against bodies with different refraction indexes. In this scenario, the multipath effect causes destructive interference due to signal overlap, impacting the useful signal.

The algorithm for the discrete multipath is divided into two components. Thus, it takes as input a set of delays and a set of gains. A pair $(delay, gain)$ refers to a specific spike in the CIR. The multipath effect in the output signal is included by convolving the built CIR with the passed signal to the function. For the sake of simplicity, changes in the phase and frequency are not considered for any paths. For more details, Listing C.7 depicts the implemented algorithm.

Rician fading channel

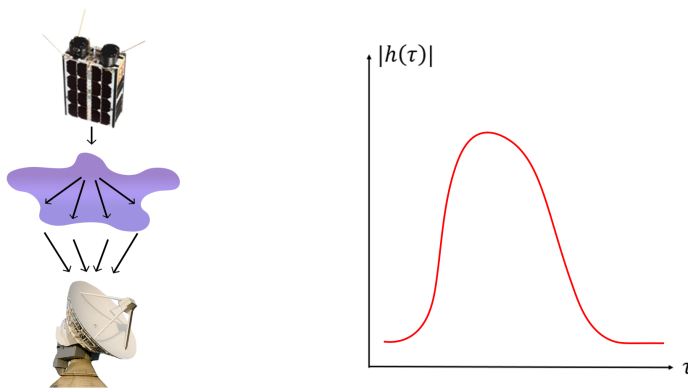


Figure 4.14: Examples of Rician fading applied to the ionosphere channel.

The choice of including the Rician fading channel is supported by the presence of random bubbles of electrons around the ionosphere. An example is shown in Figure 4.14. The density of these volumes is not homogeneous, making the multipath effect different from the one discussed in Section 4.6.4. This inhomogeneity leads the incoming signal to be separated into many different scatterers close to each other. This phenomenon is called “lensing effect” [64]. A possible CIR is shown in Figure 4.14. The Rician fading model is chosen since it is commonly used in scenarios where the LOS component is stronger than the secondary paths.

Line 38 of Listing C.7 shows how to build a Rician fading channel instance in Matlab. The parameters to include are the following:

- `SampleRate`: the sample rate. It defines how fine the resolution of the CIR is;
- `PathDelays`: the delays in seconds for each path;
- `AveragePathGains`: the average gain value in dB;
- `MaximumDopplerShift`: the maximum Doppler shift that can be applied for a path;
- `KFactor`: the K factor that represents the ratio between the power of the main path and the secondary path. The higher the K factor, the stronger the LOS path.

All these parameters are defined in the *config.m* file already introduced. Due to lack of knowledge, it was not possible to define all these parameters to replicate a real scenario. Indeed, the tail length of spikes in the CIR depends on how big the inhomogeneous electron volumes are, and the maximum Doppler shift depends on the direction in which the scatterers reach the ground station.

4.6.5 Faraday rotation

This algorithm implements the Faraday rotation (FR). As already mentioned in Section 2.1.2, the Faraday rotation is the phenomenon that leads to a change in the polarization of the transmitted signal. The complete analytical form of FR is shown in Equation 2.2 and the complete code is depicted in Listing C.8.

To include the presence of FR, the Polarization Loss Factor (PLF) is taken into consideration. [65] gives a complete formula of the PLF for any polarization pattern, shown in Equation 4.29.

$$PLF = 10 \cdot \log \left(\frac{1 + \rho_w^2 \rho_A^2 + 2\rho_w \rho_A \cos(2 \cdot FR)}{(1 + \rho_w^2)(1 + \rho_A^2)} \right) \text{ (dB)} \quad (4.29)$$

where ρ_w and ρ_A are the circular polarization ratio of the transmitted wave and receiving antenna, respectively. Assuming linear polarization of the transmitted signal and the receiving antenna and the absence of mismatching between the receiver and the transmitter radiators, Equation 4.29 can be simplified as shown in Equation 4.30.

$$PLF = \cos^2(FR) \quad (4.30)$$

If the polarization planes are completely misaligned, the PLF will be zero. It is important to underline that 1) the FR is frequency-dependent and 2) Equation 4.30

takes into account only the FR, assuming perfect pointing between the antennas. In the *config.m* file, the values of Total Electron Content (TEC) and B_{av} are fixed. In a future development of this Matlab simulator, it may be advantageous to introduce randomness into these parameters, taking into account various factors such as altitude, latitude, longitude, and time.

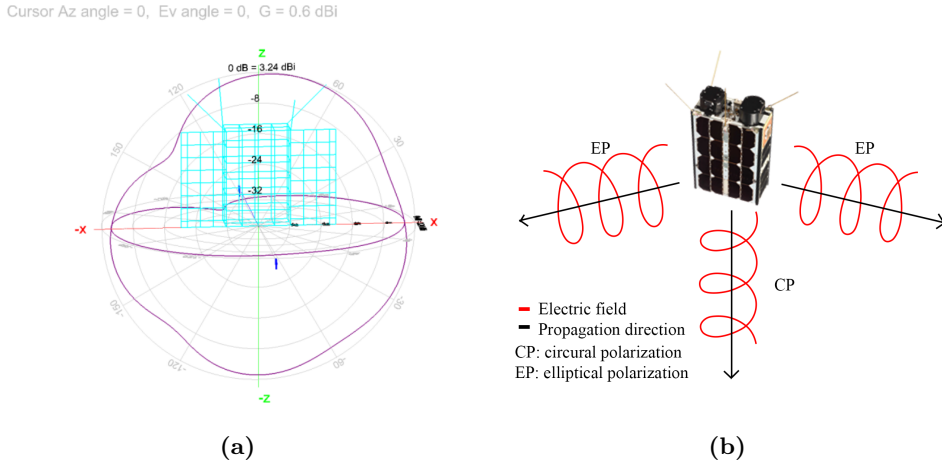


Figure 4.15: a) Example of UHF antenna simulation result for Hyperspectral Small Satellite for Ocean Observation (HYPSO)-2 from [66]; b) Example of how the polarization changes along different orientations.

The UHF antenna of HYPSO-2, a quad turnstile antenna [66], exhibits a non-linearly polarized radiation pattern. Figure 4.15b illustrates the distribution of the radiation pattern around the antenna and the variation in polarization throughout the satellite. While the model assumes knowledge and compensation of the antenna alignment, imperfect pointing can result in power fluctuations due to the emitter’s radiation pattern (see Figure 4.15a). To maximize power collection at the receiver, both the satellite and the ground station antennas are commonly designed to be circularly polarized, limiting power loss to a maximum of 3 dB. Despite the antenna mismatch, power reception is still possible, albeit with challenges in estimating Faraday rotation since Equation 4.30 no longer applies.

A solution to reduce the impact of the mismatch and detect FR is to use the antenna diversity. The scenario is depicted in Figure 4.16: two dipole antennas are rotated by a factor of 90° , so that it becomes possible to collect power by the ground station at any time. When one branch experiences a reduction of the receiver power, the other branch perceives a gain due to the rotation of the received signal polarization plane.

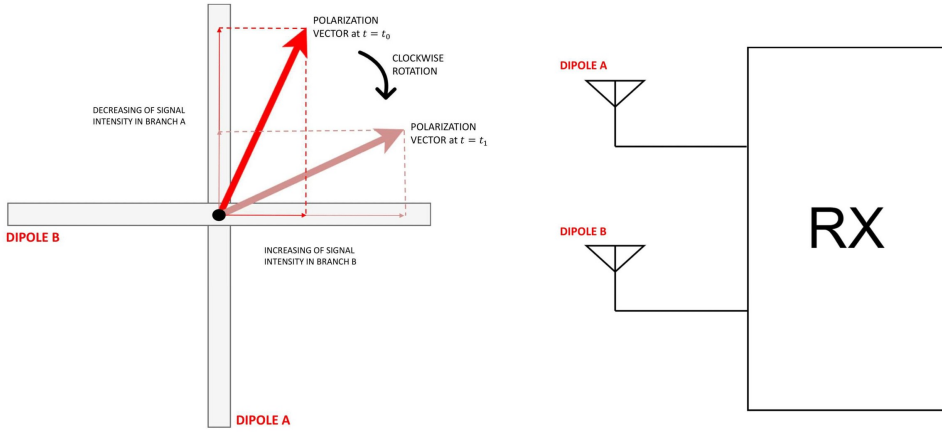


Figure 4.16: Example of antenna diversity by using two crossed dipole.

In this algorithm, an Inverse Fast Fourier Transform (IFFT) is performed to the PLF. This is used in order to apply FR in the time domain to the passed signal.

4.6.6 Ionospheric scintillation

This code shows how ionospheric scintillation (see Section 2.1.3 for the definition) is implemented in the Matlab simulator. Equation 4.31 shows how the scintillation effect is applied to an incoming signal $x(t)$:

$$y(t) = a_{peak-to-peak}(t) \cdot x(t)e^{j\rho(t)} \quad (4.31)$$

where $a_{peak-to-peak}(t)$ and $\rho(t)$ are fluctuation and phase scintillation, respectively. From [18], the intensity distribution follows a Nakagami distribution for a wide range of S_4 values. Regarding the phase scintillation, it follows a Gaussian zero-mean distribution, where the standard deviation σ_ψ characterizes how strong the randomness phase is. The Nakagami Probability Density Function (PDF) is given by:

$$p(I) = \frac{2m^m}{\Omega^m \Gamma(m)} I^{2m-1} e^{-m(I^2/\Omega^2)} \quad (4.32)$$

where Ω is the spreading factor, I is the intensity and $\Gamma(\cdot)$ is the gamma function. The Nakagami m -coefficient is shown in Equation 4.33.

$$m = 1/S_4^2 \quad (4.33)$$

Moreover, the Gaussian zero-mean PDF for the phase scintillation is given by Equation 4.34, with standard deviation σ_ψ .

$$p(\rho) = \frac{1}{\sigma_\psi \sqrt{2\pi}} e^{-\frac{x^2}{2\sigma_\psi^2}} \quad (4.34)$$

The implementation of the two distributions is depicted in Listing C.9. The functions *gaussian_phaseshift()* and *nakagami_fading()* generate \mathbb{N} numbers following a Gaussian distribution with zero mean and a Nakagami distribution respectively.

4.7 Validation Processes and Results

The implemented models are validated by applying techniques to detect and quantify the effects discussed, including the channel sounding technique explained in Section 2.2. This section presents the methods implemented and the corresponding results obtained during the post-processing phase. The post-processing algorithms can be found in the `Receiver/` folder, as illustrated in Figure 4.5.

4.7.1 Doppler shift estimation and compensation

The first post-processing function that is implemented is the Doppler estimation and compensation, by using a convolution method in the frequency domain. The algorithm is depicted in Listing C.10. The signal is passed to the function (in the case of this thesis, the sequence Pseudo-Noise (PN) received by the ground station) and the Fast Fourier Transform (FFT) is calculated through the custom function *continuousFTsamples()*. Subsequently, the auto-convolution in the frequency domain to the received signal is performed.

To understand the aforementioned process, it is necessary to discuss how this phenomenon affects the transmitted signal. Equation 4.27 shows the analytical form of a frequency-shifted signal and Equation 4.35 [67] the same signal in the frequency domain:

$$F[x(t) \cdot e^{j2\pi f_{shift}t}] = X(f - f_{shift}) \quad (4.35)$$

where $F[\cdot]$ is the Fourier transform operator and $X(f)$ is the Fourier transform of the signal $x(t)$. The auto-convolution of the function $X(f)$ is shown in Equation 4.36.

$$(X * X)(f) = \int_{-\infty}^{+\infty} X(\rho)X(f - \rho)d\rho \quad (4.36)$$

Let us consider the property of the convolution [68] shown in Equation 4.37. This relationship indicates that the convolution of two time-shifted functions f_1 and f_2 by t_1 and t_2 respectively leads to the function f shifted by $t = t_1 + t_2$.

$$f_1(t - t_1) * f_2(t - t_2) = f(t - (t_1 + t_2)) \quad (4.37)$$

By considering the frequency instead of the time, Equation 4.36 can be written as reported in Equation 4.38.

$$X(f - f_{shift}) * X(f - f_{shift}) = \tilde{X}(f - 2 * f_{shift}) \quad (4.38)$$

Considering the shape of the PN function in the frequency domain shown in Figure 2.11, it is possible to assume that by looking at the magnitude of the function \tilde{X} , the maximum value of the function lies exactly at twice the frequency shift f_{shift} . The result of this method is depicted in Figures 4.17. Figure 4.17b shows the auto-convolution of the received signal, and it can be inferred that the maximum peak lays on twice the Doppler shift considered for the simulation, i.e. 7267.9228 Hz. Figure 4.17a shows before and after the compensation. The compensation of the Doppler shift is shown in line 8 of Listing C.10. As expected, the resulting signal is centred on the origin, validating the adopted method. Table 4.1 presents the simulation results for ten different elevation angles, with a center frequency of 436.5 MHz and a satellite altitude of 500 km. The evaluated maximum error on the estimation is 23.7256 Hz, meaning that the evaluation process has a high accuracy in approximating the frequency shift. Indeed, it is necessary to have good compensation for the Doppler shift in order not to degrade the performance of the channel sounder.

Another observation of the Doppler effect and the PN sequence is presented. The Doppler rate, as already mentioned, is the rate of the Doppler shift to change in time (see Section 4.6.3). The higher the Doppler rate, the lower the coherence time, since the channel changes fast. Then, it is mandatory to design the length L of the PN sequence in order to maintain the condition of quasi-stationarity. In conclusion, the higher the Doppler rate, the smaller the PN sequence length.

4.7.2 Multipath effect analysis: the channel sounder technique

This Section provides a description of the channel sounder's design and the validation process of the technique employed. Table 2.1 [41] shows a set of relations for the

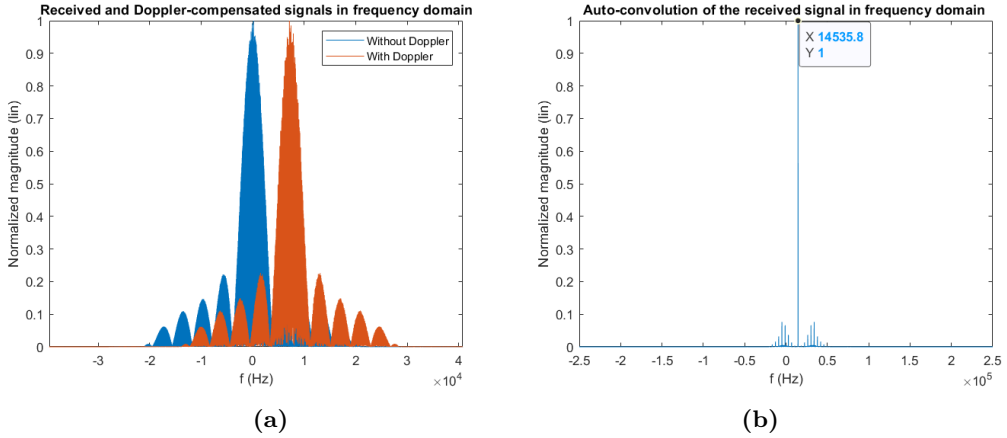


Figure 4.17: Example of Doppler estimation and compensation by using the convolution method, considering a Doppler shift $f_D = 7267.9228$ Hz. (a) shows the signal before and after the compensation, and (b) shows the auto-convolution of the received signal in the frequency domain.

Table 4.1: Simulation of ten elevation angles, considering center frequency $f_c = 436.5$ MHz and satellite altitude $h = 500$ km.

#	Elevation angle ($^\circ$)	Evaluated f_D (Hz)	Estimated f'_D (Hz)
1	0	10301.7587	10278.0331
2	10	10122.0627	10121.7831
3	20	9658.3598	9658.3946
4	30	8901.1926	8900.8885
5	40	7873.5671	7873.7745
6	50	6606.7072	6606.924
7	60	5139.1059	5139.3995
8	70	3515.3555	3515.625
9	80	1784.7928	1784.6201
10	90	7.8486×10^{-12}	0

design of a channel sounder. Considering a sample rate of $f_s = 500$ kS/s, it is possible to compute the temporal resolution $T_{res} = 1/f_s = 2 \mu\text{s}$. Since it is difficult to predict the maximum multipath delay, it is assumed a maximum value in the order of milliseconds. Indeed, the maximum multipath delay depends on the altitude of the satellite, the TEC amount, the elevation angle and the aperture of the radiation pattern of the ground station. Considering the length PN sequence $L = 255$, the

maximum resolvable multipath delay is $\tau_{max} = L/f_s = 510 \mu\text{s}$.

Instead of sending just one PN sequence, it is decided to send the same sequence ten times in series. The advantage of this approach can be seen by looking at the dynamic range in Table 2.1. Indeed, the higher the length of the transmitted signal, the higher the dynamic range. This can be seen by performing the cross-correlation function in order to obtain the impulsive response of the channel (see Equation 2.18).

Figure 4.18 depicts the simulation result under discrete multipath regime discussed in Section 4.6.4. The result of this simulation considers all the channel entities in the received signal. Clearly, the graph at the bottom shows the reference CIR that was created by the simulator and applied to the received signal, while the graph at the top shows the result obtained by the *ChannelSounder()* function in Listing C.11. Both graphs are nearly identical, with negligible differences in the spike positions and magnitudes on the delay axis. The triangle-shaped spikes arise from the cross-correlation function of the PN sequence, illustrated in Figure 2.10.

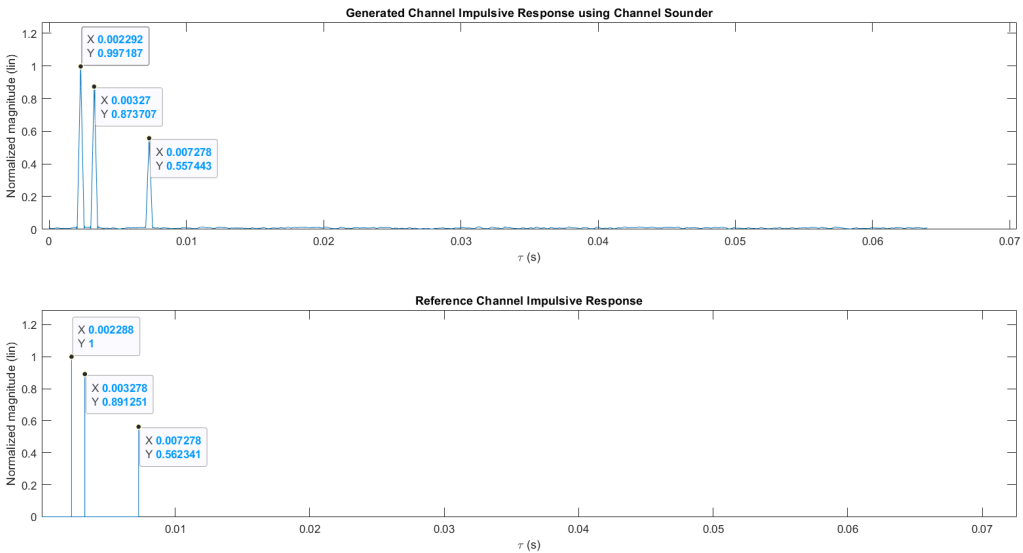


Figure 4.18: CIR result from discrete multipath simulation, considering $10 \mu\text{s}$, 0.1 ms and 0.2 ms of exceed delays and 0 dB , -1 dB and -5 dB of average path gains.

The second simulation involves the utilization of the Rician fading channel model to account for the multipath effect. The post-processing, even under Rician fading, led to an expected result.

Some considerations are found in both iterations, i.e. in case of discrete multipath

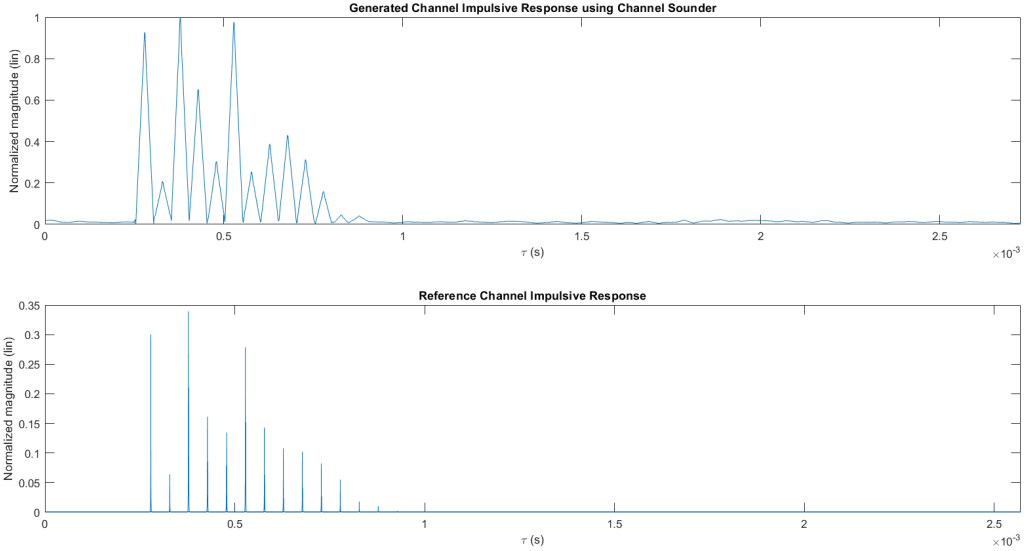
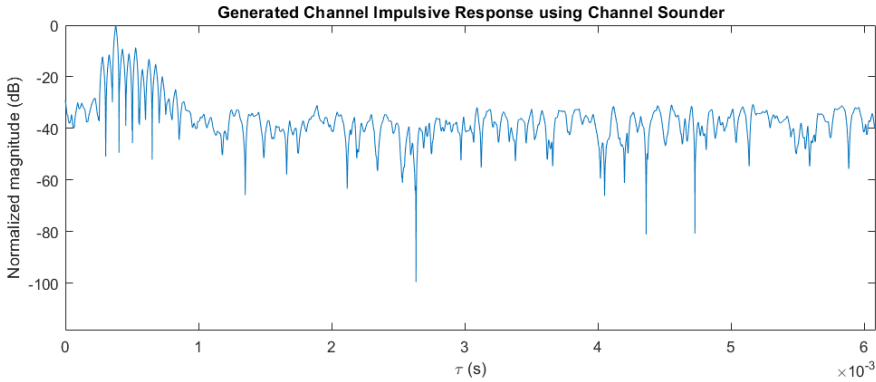


Figure 4.19: CIR result from Rician fading multipath simulation, considering $10 \mu\text{s}$, 0.1 ms and 0.2 ms of exceed delays and 0 dB , -1 dB and -5 dB of average path gains.

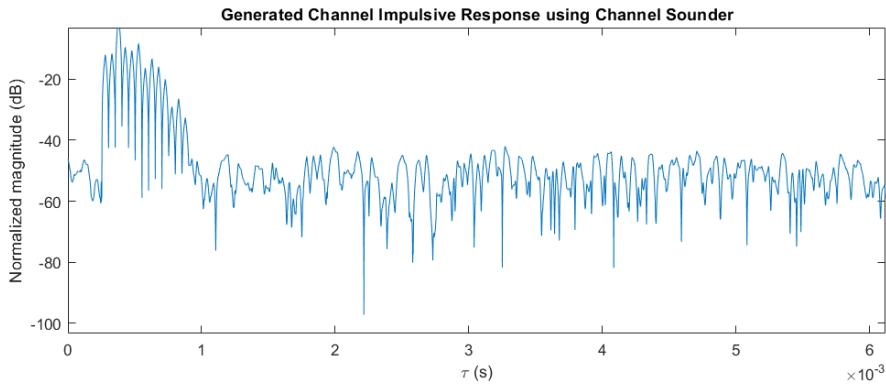
and the Rician fading channel. As depicted in Figure 4.20, it is possible to reduce the noise floor (i.e. increase the dynamic range) produced by the cross-correlation algorithm by sending more PN sequences in series. Indeed, the dynamic range is the ratio between the maximum amplitude value of the signal without distortion and the noise floor [69]. It is visible that the noise floor in the graph at the top is in the order of -40 dB , whereas the graph at the bottom is almost -55 dB . Moreover, the influence of the thermal noise has not a huge impact on the cross-correlation, due to the pseudo-stochastic property of the PN sequence.

Some limitations are discussed in this paragraph. Increasing the sequence length in a communication system can have implications on the quasi-stationarity condition. By increasing the sequence length L , the condition $T_{chip}L \ll T_{coh}$ may no longer hold, where T_{chip} is the duration of a single chip of the PN sequence and T_{coh} is the coherence time of the channel. This means that the channel may exhibit time-varying characteristics along the whole sequence.

Another factor impacting the performance of the system is the bandwidth. The time resolution is inversely proportional to the chip rate f_{chip} , with $T_{res} = 1/f_{chip}$. Hence, narrower bandwidth restricts the ability to resolve and identify secondary propagation paths.



(a)



(b)

Figure 4.20: Example of two Rician fading multipath channel simulations, considering one (a) and ten (b) PN sequences in series.

Additionally, the sequence length L affects the maximum multipath delay τ_{max} . A smaller sequence length leads to a decrease in the maximum multipath delay detectable, which can be calculated as $\tau_{max} = L/f_{chip}$. Consequently, the maximum path length d_{max} is determined by the product of the speed of light c and τ_{max} , assuming that the group velocity is negligible.

In summary, the sequence length, the number of sequences sent in series, the bandwidth and the delay are interconnected and influence the quasi-stationarity condition and the ability to detect secondary paths. Careful considerations of these factors are necessary to optimize system performance and accurately capture the channel characteristics.

4.7.3 Ionospheric Scintillation: the S_4 parameter

This Section delves into the results produced during the validation phase of the ionospheric scintillation implementation in the Matlab simulator. As already discussed in Section 4.6.6, ionospheric scintillation is an electromagnetic phenomenon caused by the presence of electron volumes with different densities. The interaction between the electromagnetic field and the ion clouds leads to a degradation of the received signal in both phase and amplitude.

The algorithm is based on Equation 2.5. As already mentioned in Section 4.7.2, one of the advantages of sending multiple times the same PN sequence is to improve the dynamic range. In the context of ionospheric scintillation, this method is used to increase the number of samples and converge the S_4 parameter.

The variable `N_sequ` corresponds to the number of sequences sent in series. Then, within the loop-for, the parameter S_4 is calculated iteratively, considering several windows to study the convergence of the parameter. One window corresponds to one complete PN sequence. For example, if the signal being received has ten sequences in series, the function computes the S_4 parameter from one to ten windows. Figure 4.21 shows the operation of the windows and Listing C.12 depicts the implemented algorithm in Matlab.

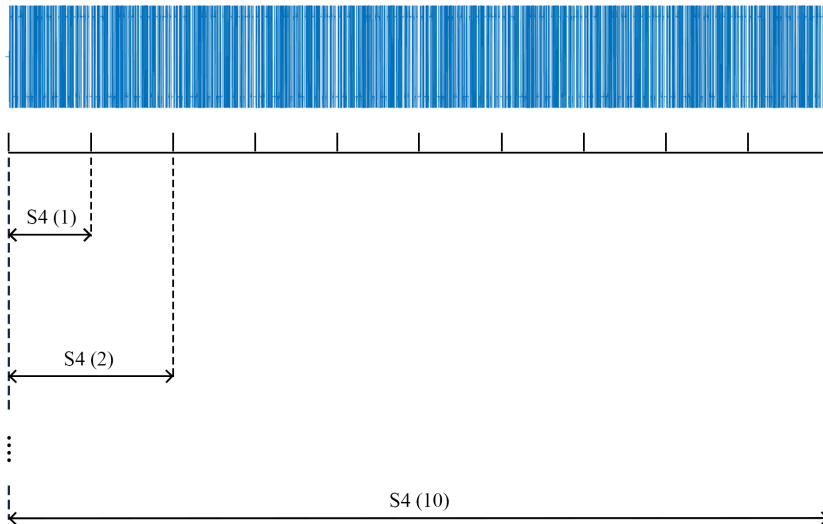


Figure 4.21: Visualization of the window method to compute the S_4 parameter. The pattern in blue represents the ten PN sequences that are sent in series.

Two important results are highlighted in Figures 4.22 and 4.23. The first figure shows the simulation of the ionospheric scintillation considering the Nakagami fading

channel and the zero-mean Gaussian distribution mentioned in Section 4.6.6. The **Input Signal** plot shows the reference signal, i.e. the transmitted PN sequence. The **Output Signal** plot shows how the signal is distorted due to the presence of ionospheric scintillation. The two graphs below show how the stochastic distributions of both peak-to-peak amplitude and phase shift are compliant with the theoretical distributions. Moreover, the graph **Cross-correlation** shows the cross-correlation between the transmitted signal and the received signal. Note that, even though the received signal is distorted, the channel sounding technique still manages to work, due to the pseudo-stochastic property of the PN sequence.

Figure 4.23 shows the result of five simulations. For each simulation, the m -parameter described in Equation 4.33 is changed, considering the values of S_4 given in the legend. Note how the estimated value of S_4 gradually converges as a function of the number of windows considered by the function in Listing C.12. Furthermore, for small values of S_4 , the value obtained tends to converge more slowly since the transmitted signal is also variable. Therefore, it is taken into account in the calculation of the ionospheric scintillation index. In fact, the ionospheric scintillation index is by definition the second moment of intensity. The issue lies on the direct proportionality between intensity and signal power, which, in turn, is determined by the square of the signal amplitude. Hence, the S_4 parameter corresponds to the fourth moment of the amplitude of the transmitted signal, and this explains the slow convergence.

As discussed by [26] and [70], the typical calculation of the S_4 parameter occurs over a one-minute period, in order to have a satisfactory convergence. This approach poses challenges when dealing with LEO satellites, as their dynamic nature prevents measurements from being conducted in a fixed area over an extended duration, in contrast to Global Navigation Satellite System (GNSS) satellites. Moreover, the ionospheric scintillation index considers all the effects present in the signal, making it difficult to isolate and differentiate individual entities within the channel. Notably, in scenarios featuring multipath effects where secondary paths exhibit significant amplitude, the S_4 parameter becomes heavily influenced by the multipath entities, consequently obscuring the presence of ionospheric scintillation.

4.7.4 Faraday rotation: the dual-frequency technique

Faraday rotation, as already defined in Section 2.1.2, is the electromagnetic phenomena caused by the presence of Earth's magnetic field and electron content in the ionosphere. The result is a rotation of the polarization plane of the transmitted signal along the propagation path. It is important to note that the angle of rotation FR depends on the frequency of the transmitted signal, as shown in Equation 2.4. Hence, the dual-frequency technique is considered for estimating the FR. This technique is

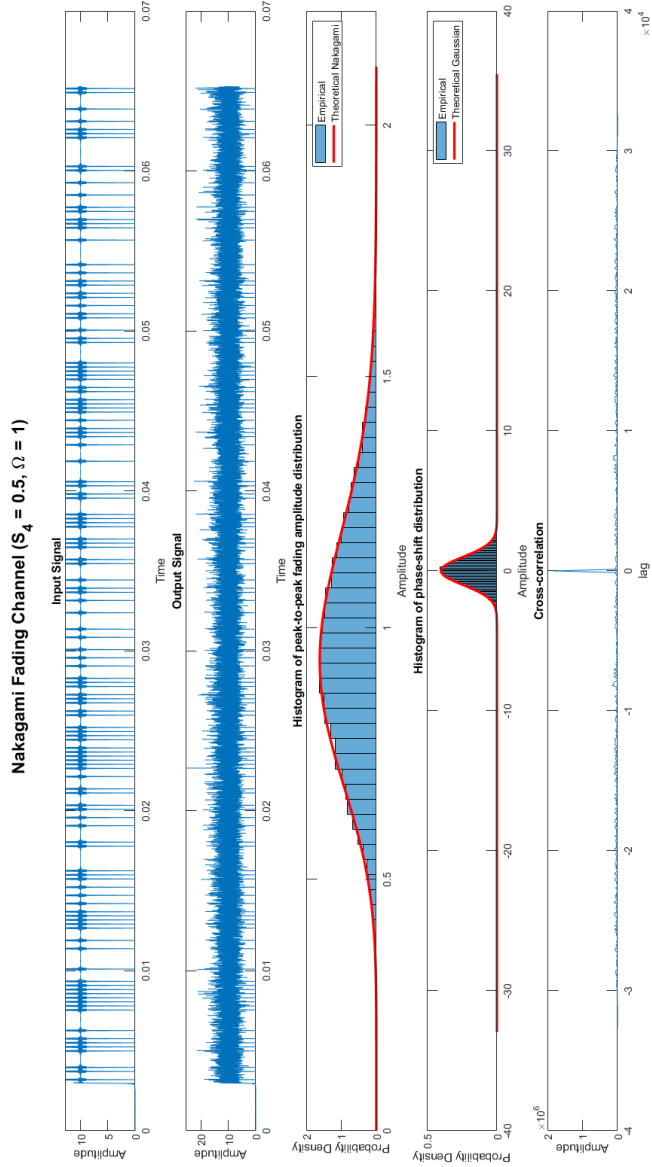


Figure 4.22: Simulation result of ionospheric scintillation.

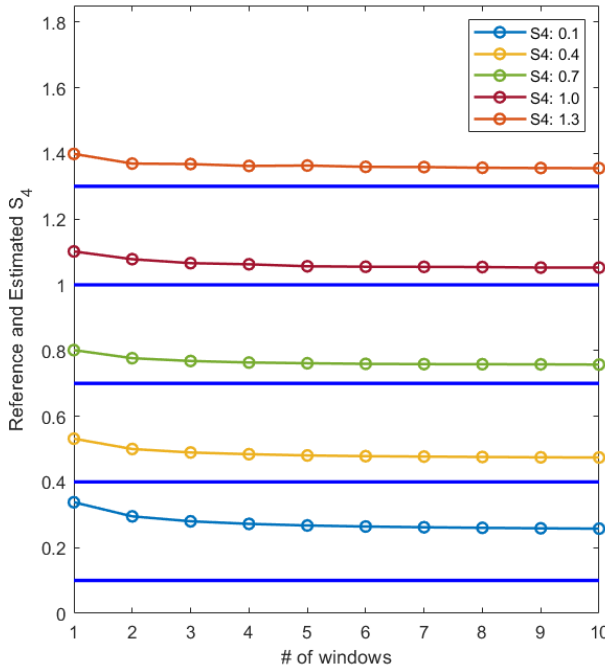


Figure 4.23: Windows method to compute the S_4 parameter. For this simulation, five different S_4 parameters are set and estimated.

applied when the receiver is capable of receiving multiple carrier frequencies [71].

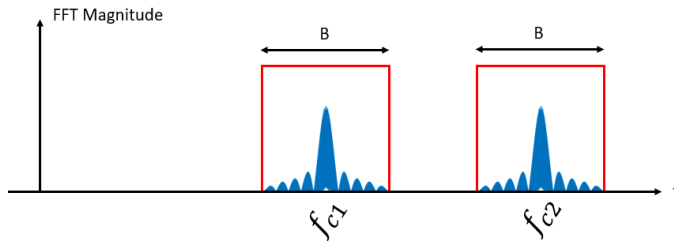


Figure 4.24: Diagram illustrating the operation of dual-frequency technique.

Let us consider having two carrier frequencies f_{c1} and f_{c2} as depicted in Figure 4.24. The same signal with bandwidth B is transmitted along the two carrier frequencies. Let us assume that the spacing between the two carrier frequencies is large enough to perceive the presence of Faraday rotation. Assuming that the antennas' pointing is known and compensated, the only deviation on the polarization

at the receiver is due to the Faraday rotation. By using Equations 2.4 and 4.30, the complete formula of PLF is shown in Equation 4.39, where B_{av} and TEC are considered constant and the frequency f is in GHz

$$PLF = \cos^2(FR) = \cos^2\left(2.36 \times 10^{-14} \frac{B_{av} TEC}{f^2}\right) \quad (4.39)$$

Given the MHz frequencies under examination and satisfying the condition $B/f_{ci} \ll 1$, for $i = 1, 2$, a reasonable assumption is a linear trend for the cosine square along the frequency axis. The utilized parameters are presented in Table 4.3, considering Figure 4.24 as a reference.

Table 4.3: Parameters considered for the dual-frequency technique.

Name	Symbol	Value
Signal bandwidth	B	500 kHz
Left-hand carrier frequency	f_{c1}	436.25 MHz
Right-hand carrier frequency	f_{c2}	437.75 MHz

Hence, one can approximate Equation 4.39 as given in 4.40.

$$\cos^2(FR) \approx b - a \cdot f^{(1)} \quad (4.40)$$

Let us define Y_1 and Y_2 as the peak magnitudes in the frequency domain of the transmitted signal along f_{c1} and f_{c2} , respectively. It is possible to assume that the peak magnitudes are at the center frequencies due to the nature of the PN sequence in the frequency domain (see Figure 4.24). Then, it is possible to write Equation 4.41, where X is the Fourier transform magnitude of the transmitted signal.

$$Y_i = Y(f = f_{ci}) = X \cdot \cos^2(FR_i), \quad i = 1, 2 \quad (4.41)$$

The system that must be solved is shown in 4.42.

⁽¹⁾this does not hold to any frequency. The designer has to look at the PLF trend in function of the used frequencies.

$$\begin{cases} \cos^2(FR_1) \approx b - a \cdot f_{c1} \approx Y_1/X \\ \cos^2(FR_2) \approx b - a \cdot f_{c2} \approx Y_2/X \end{cases} \rightarrow \begin{cases} a = \frac{Y_1 - Y_2}{f_{c2} - f_{c1}} \cdot \frac{1}{X} \\ b = \frac{Y_1}{X} + \frac{Y_1 - Y_2}{X} \cdot \frac{f_{c1}}{f_{c2} - f_{c1}} \end{cases} \quad (4.42)$$

To conclude, Equation 4.43 depicts the final version of the PLF.

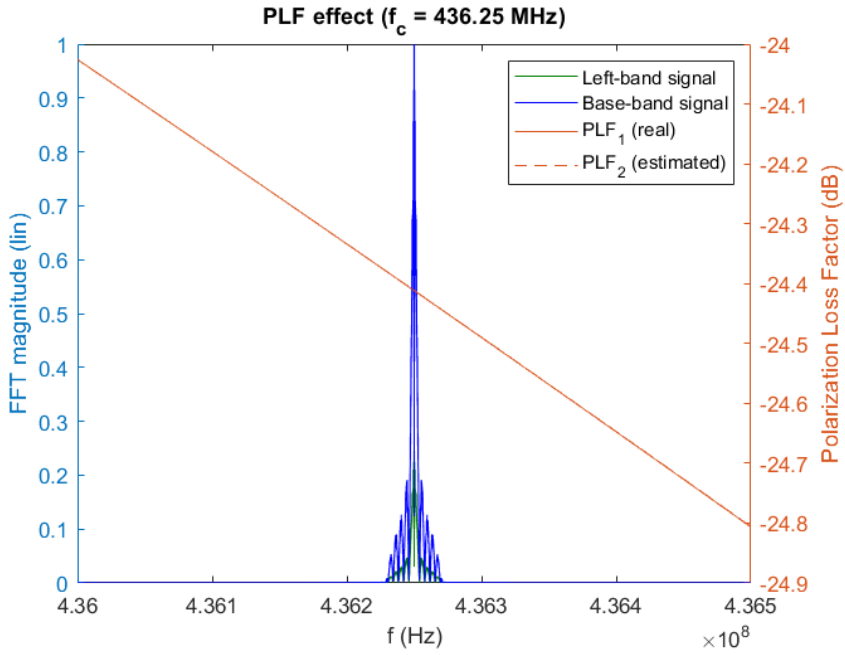
$$PLF = \cos^2(FR) = \frac{Y_1}{X} + \frac{Y_1 - Y_2}{X} \cdot \frac{f - f_{c1}}{f_{c2} - f_{c1}} \quad (4.43)$$

As a consequence, it is possible to estimate the PLF along the frequency by knowing Y_1 and Y_2 . It is worth noting that other attenuations are present inside the result if Y_1 and Y_2 are considered, such as, the ionospheric scintillation. If all attenuations are estimated, it is possible to isolate the PLF.

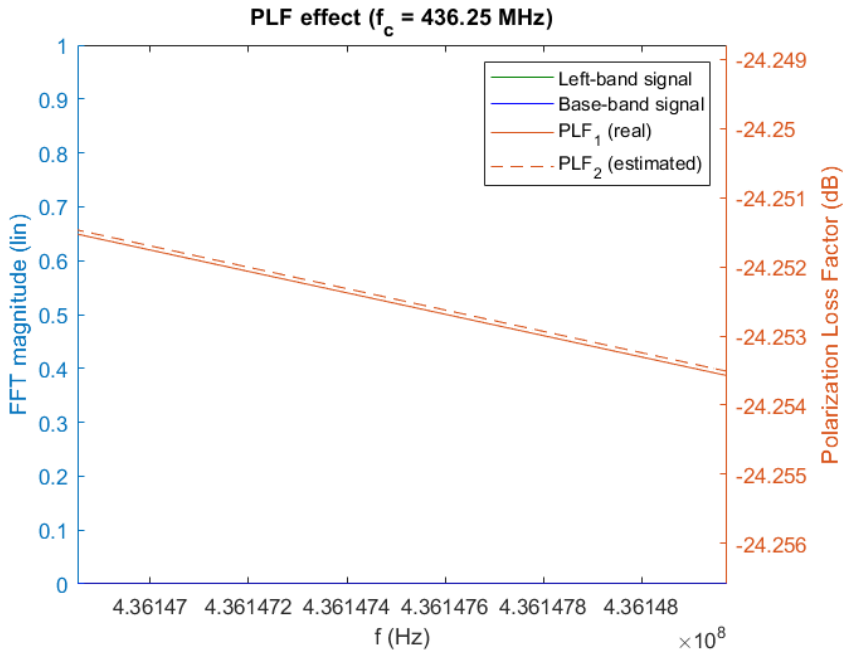
Figures 4.25 and 4.26 show a result by using Equation 4.43, i.e.:

- *Green pattern*: it represents the received signal affected by FR;
- *Blue pattern*: it represents the transmitted signal, without attenuation;
- *Continuous-orange pattern*: it represents the reference PLF pattern applied to the transmitted signal;
- *Dashed-orange pattern*: it represents the estimated PLF pattern.

Figures 4.25b and 4.26b show a close-up of the two graphs. Every simulation showed that the estimation error of PLF is in the order of -100 dB.

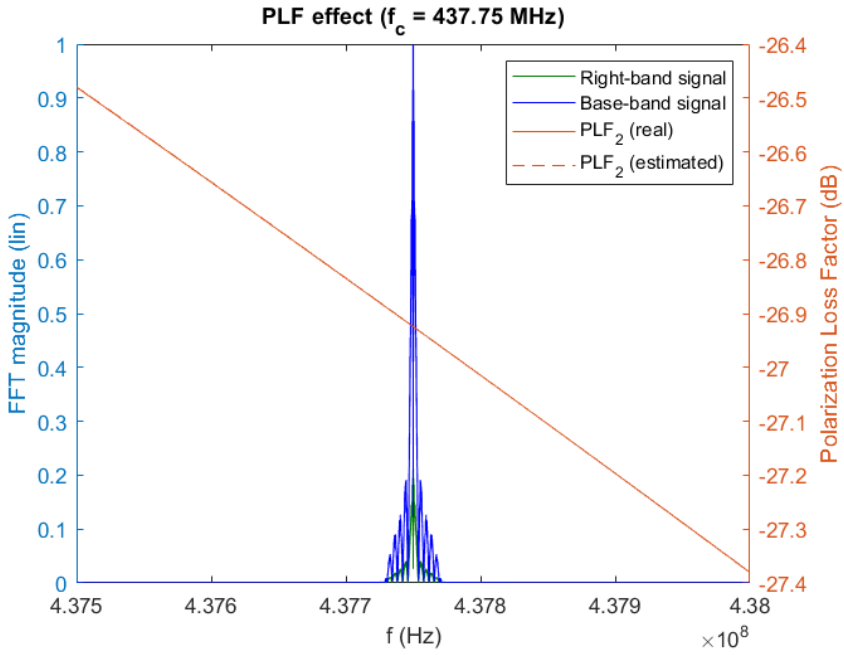


(a)

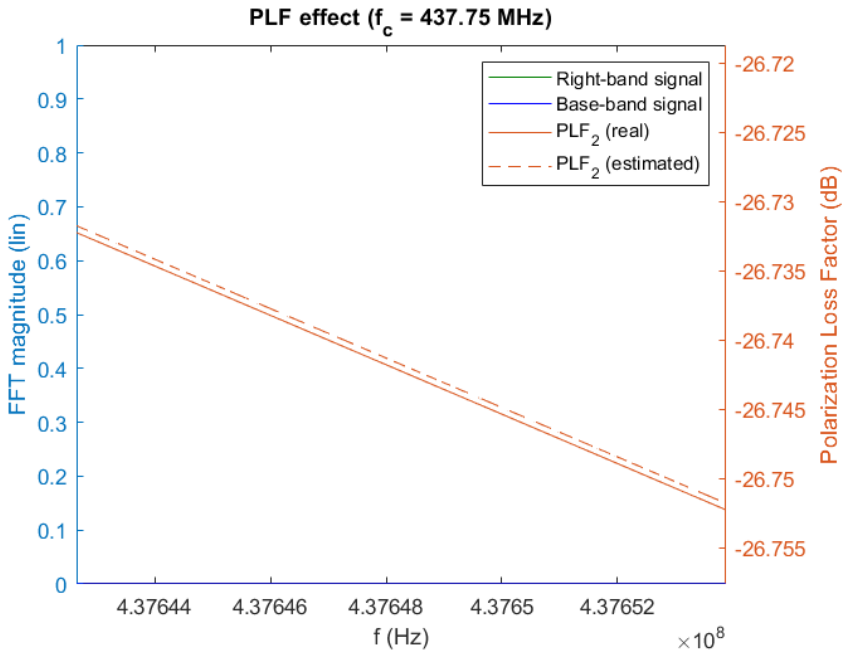


(b)

Figure 4.25: Simulation results of FR and use of dual-frequency technique, considering $f_{c2} = 436.25$ MHz.



(a)



(b)

Figure 4.26: Simulation results of FR and use of dual-frequency technique, considering $f_{c2} = 437.75$ MHz.

Chapter 5

Phase Two: SDR testbed

This Chapter provides a comprehensive overview of the Software Defined Radio (SDR) testbed. Calibration and characterisation procedures of the different entities in the testbed are also addressed. Finally, the application of the channel sounder through the Hardware-In-the-Loop (HIL) testing is covered. Procedures concerning communication configuration related to the testbed are covered in Appendix D.

5.1 Testbed setup

The high-level view of the SDR testbed is shown in Figure 5.1. The system can be divided into three main entities:

- **HYPISO FlatSat:** for the sake of simplicity, only the two main components are reported, i.e. the LidSat workstation and the Energy Power Supply (EPS). The LidSat is used to communicate with all the entities of the FlatSat via Controller Area Network (CAN)-bus. To send data, the Cubesat Space Protocol (CSP) is used. CAN0 is used to make the communication between the workstation and the EPS. The EPS is used to feed the TOTEM board.
- **External Computer:** a general purpose computer with an Ubuntu installation;
- **SDR testbed:** the core part of the SDR measurements. It is mainly composed of the TOTEM SDR, the Universal Software Radio Peripheral (USRP)-2901 and the R&S[®] FSV Signal and Spectrum Analyzer. The TOTEM SDR is used as a transmitter and the USRP-2901 as a receiver. A spectrum analyzer is included to verify the generated signal. In addition to a 3 dB splitter, a 30 dB attenuator is added to ensure that the maximum power level at the receiver can not be overtaken [59], [72].

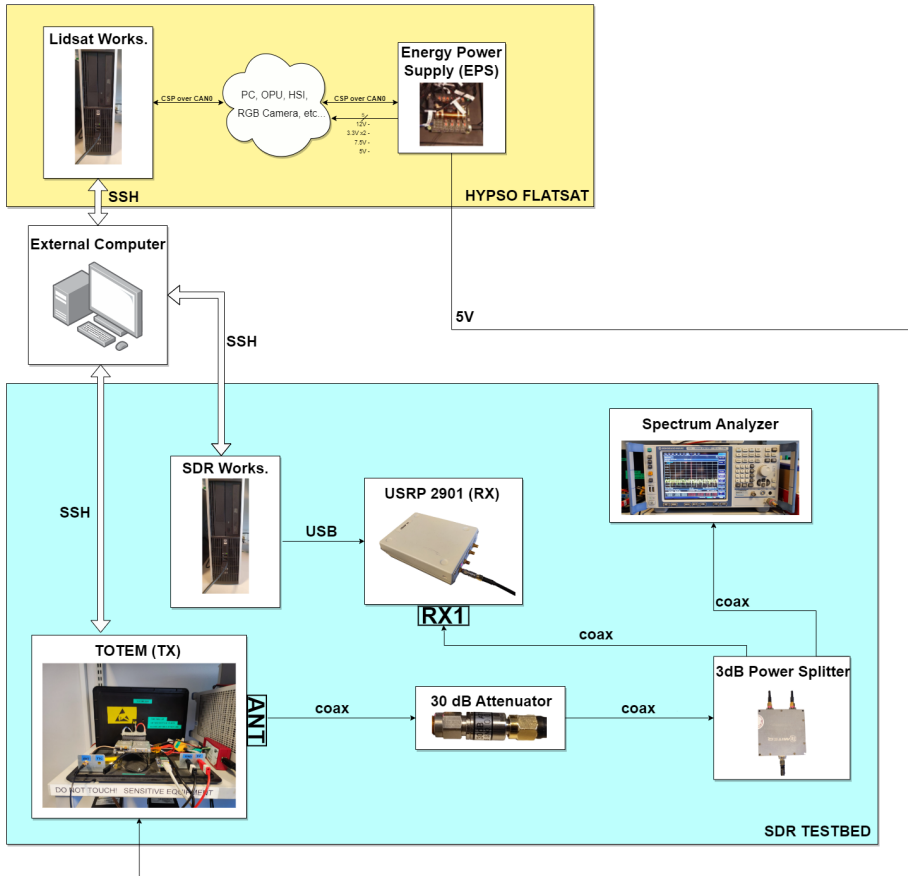


Figure 5.1: High-level view of the testbed.

5.2 Design and characterization of the communication lines

This Section discusses the design choices related to the communication lines between the TOTEM SDR and USRP-2901.

5.2.1 Design

The decision of the attenuator is discussed hereafter. Figure 5.2 shows the transmission chain between the TOTEM SDR and the USRP-2901. Equation 5.1 shows the link budget, where $P_{OUT,TOTEM,max}$ is the maximum transmittable power by TOTEM SDR and $P_{IN,USRP,max}$ is the maximum receivable power by the USRP-2901.

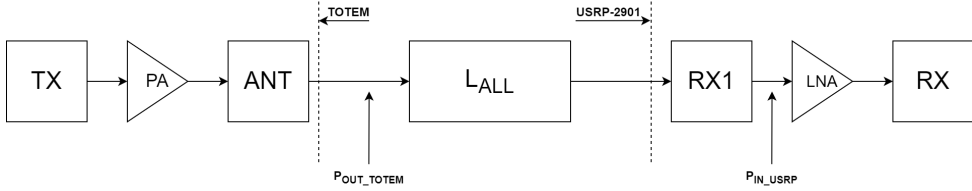


Figure 5.2: Transmission chain between TOTEM SDR and USRP-2901.

$$P_{IN,USR,P,max} = P_{OUT,TOTEM,max} - L_{ALL} \quad (5.1)$$

By using the data from Tables 3.1 and 3.3b, one can obtain the required attenuation L_{ALL} , i.e.:

$$L_{ALL} = P_{OUT,TOTEM,max} - P_{IN,USR,P,max} = 30 \text{ dBm} + 15 \text{ dBm} = 45 \text{ dB} \quad (5.2)$$

A 30 dB attenuator is selected to ensure an adequately strong input power at USRP-2901.

5.2.2 Characterization

The second step is to measure the frequency response of the communication line. In order to achieve this, we measure the S-matrix of the 3-port. The S-matrix [73], also called *scattering matrix*, is a useful mathematical tool which describes the behaviour of a N-port. An N-port is, nevertheless, a device or a network with two or multiple ports, called *terminals*. For the j -th terminal, we can define a forward-traveling wave a_j^+ and a backward-traveling wave a_j^- . These quantities represent the electromagnetic field intensity inside the N-port. Figure 5.3 shows an example of 4-port. The general formula that describes an N-port is depicted in Equation 5.3.

$$\vec{a}^- = \overline{\overline{S}} \cdot \vec{a}^+ \quad (5.3)$$

where $\overline{\overline{S}}$ represents the S-matrix. Each coefficient of the S-matrix has a meaning, i.e.:

- S_{ii} ($i : 1 \dots N$), N (number of terminals) represents the *reflection coefficient* of the i -th port. It indicates the fraction of incident power that is reflected at the same port;

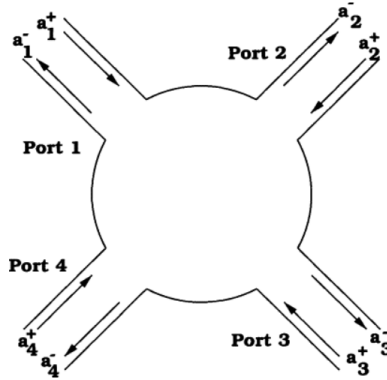


Figure 5.3: General representation of a 4-port. From [73]

- S_{ij} ($i, j : 1...N$), $i \neq j$, N (number of terminals) is the *transmission coefficient* between the j -th and the i -th ports. It represents the fraction of incident power to the j -th port that is transmitted to the i -th port.

In our system, the connection lines block is formed by:

- three coaxial cables;
- 30 dB attenuator;
- 3 dB power splitter.

The connection lines can be represented as a 3-port. This is visible in Figure 5.1, where port J1 is the ANT port of the TOTEM SDR, port J3 is the termination of the spectrum analyzer and port J2 is the RX1 port of the USRP-2901.

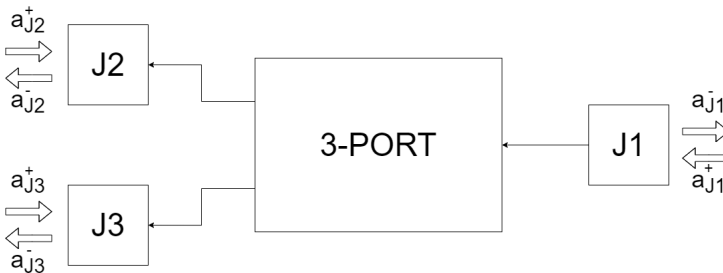


Figure 5.4: Representation of the connection lines of Figure 5.1.

The S-matrix of the aforementioned 3-port is shown in Equation 5.4.

$$\begin{bmatrix} a_{J1}^- \\ a_{J2}^- \\ a_{J3}^- \end{bmatrix} = \begin{bmatrix} S_{11} & S_{12} & S_{13} \\ S_{21} & S_{22} & S_{23} \\ S_{31} & S_{32} & S_{33} \end{bmatrix} \begin{bmatrix} a_{J1}^+ \\ a_{J2}^+ \\ a_{J3}^+ \end{bmatrix} \quad (5.4)$$

Figure 5.5 shows the S21 and S31 parameters for both J1-J2 and J1-J3 lines. Both values are measured in a bandwidth of 500 kHz with center frequency of 437 MHz. It can be seen that both terms are not constant along the frequency axis. This is due to the presence of thermal noise, which is, therefore, not relevant to the measurements. It is noticeable that the mean value of both patterns is constant to a fixed value along the frequency axis. Indeed, the mean values are -34.52 dB (fuchsia pattern) and -34.59 dB (green pattern) for S31 and S21 respectively. This is expected given the relatively small bandwidth. In conclusion, it is possible to set $L_{ALL} = 34.52$ dB. The only caution we have maintained is to limit generating more than 14 dBm in the transmission port, thus preventing overexcitation of the input port of the USRP-2901.

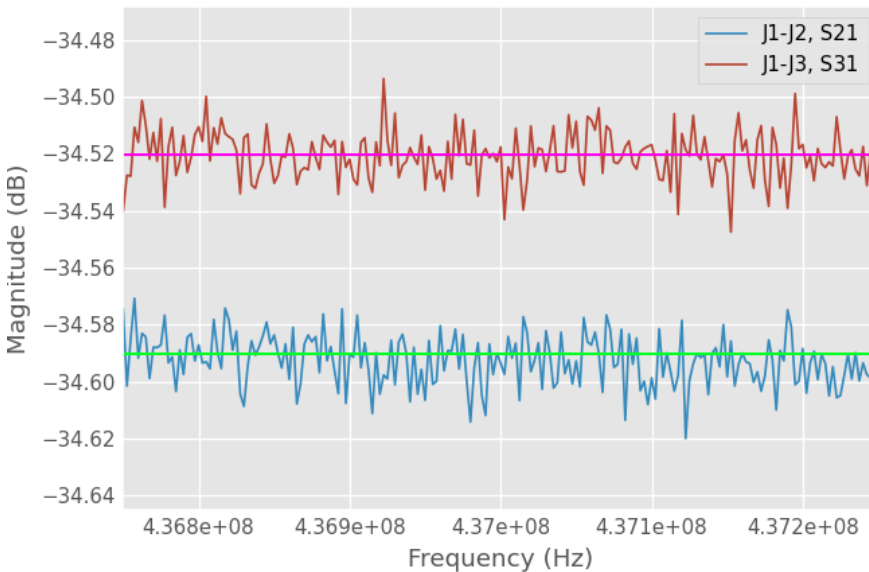


Figure 5.5: Measured S21 and S31 parameters for both lines J1-J2 and J1-J3. The fuchsia and green lines represent the average of both S31 and S21 respectively.

5.3 Software Defined Radio: Characterization and Calibration procedures

This Section covers all the aspects related to the calibration and characterization of the SDR testbed. As already depicted in Figure 5.1, the TOTEM SDR is used to emulate the satellite in orbit, whereas the USRP-2901 is used to emulate the ground station.

5.3.1 USRP-2901 as receiver

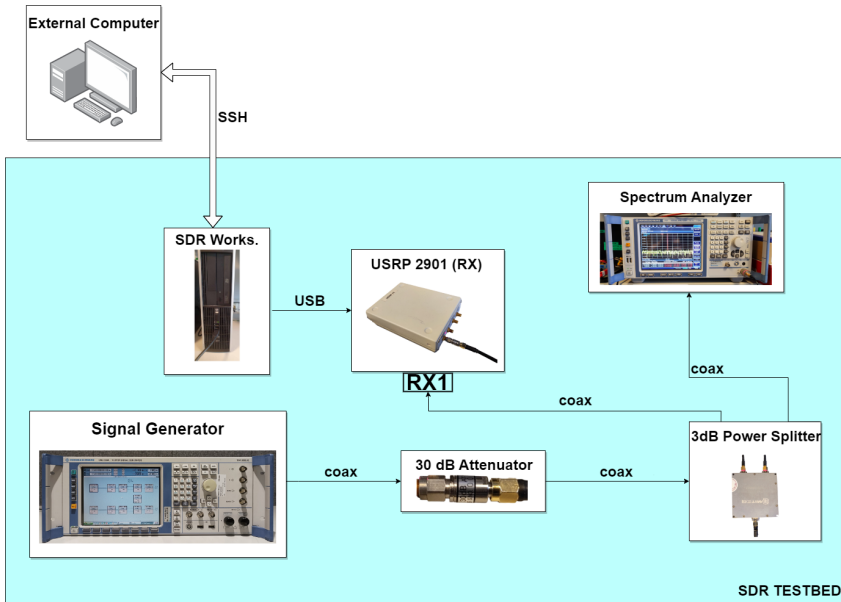


Figure 5.6: Characterization and calibration setup for the USRP-2901 as a receiver.

Since the USRP-2901 is intended to emulate the ground station, calibration and characterization operations are necessary to optimize its performance as a receiver. For this purpose, the R&S[®] SMU200A vector signal generator is used as a transmitter. Characterising means finding and analysing the features of the radio device. The observed measurements are introduced hereafter:

- *Gain Characterization:* the Low Noise Amplifier (LNA) response is measured in function of different input power and gain levels. By selecting a most suitable LNA gain value, we measure the frequency response of the gain device;
- *Local Oscillator (LO) Calibration:* in this phase, the LO frequency reference is compared to a known, stable reference signal. Then, we select the offset value to reduce the LO leakage as much as possible;

- *In-phase (I) and Quadrature (Q) Imbalance Calibration (or IQ Imbalance Calibration)*: we identify and correct possible imbalances between the I and Q channels in the SDR’s signal path by generating a single carrier;
- *Direct Current (DC) Offset Calibration*: lastly, we measure and possibly compensate for any DC offset in the baseband signal path.

First, we characterise the LNA of the SDR. In order to achieve this, the two GNU Radio applications `USRP_Characterization_CARRIER.grc` and `USRP_Characterization_CHIRP.grc` are implemented. These are shown in Figures 5.7 and 5.8, respectively.

The first step is to find the compression curve of the LNA using the GNU Radio application `USRP_Characterization_CARRIER.grc` shown in Figure 5.7. The application reads samples from the *USRP Source* block, performs the Fast Fourier Transform (FFT) using a Rectangular window and calculates the magnitude. Finally, the samples are saved in a binary file to be read by a Matlab code. Different parameters are defined inside the application. The most important is the number of bins per window for the FFT (`Nfft`) equal to 1024, the center frequency (`fc`), the LNA gain (`adc_gain`) and the number of FFT windows per measurement to be saved in a single file (`nwin`). The number on FFT windows is relevant since in the post-processing phase all the windows are overlapped and we compute the median to reduce the noise effect.

A single carrier with a frequency offset of 50 kHz and center frequency 437 MHz is generated. To mitigate the presence of the harmonic at the center frequency, introduced by the hardware’s local oscillator (LO) frequency, an offset is incorporated (see Figure 5.9). It is decided to study the compression effect for different LNA gains, i.e. 30, 40, 50, 60 and 70 dB.

Figure 5.10 shows the compression analysis. The plot shows the normalized received power at the SDR in function of different LNA gains (see legend at the top-left side of the figure). All the gains experience compression after a certain transmitted power level. A gain of 40 dB is determined to be the most suitable choice.

Given the results of the previous analysis, our next step involved characterising the frequency response of the LNA. In this phase, the GNU Radio application `USRP_Characterization_CHIRP.grc` is used and shown in Figure 5.8. The application generates a chirp signal with parameters shown in Table 5.1. The chirp time interval is depicted in Equation 5.5, where N_{STEPS} represents the number of frequencies that are selected along the band and Δf is the frequency step width.

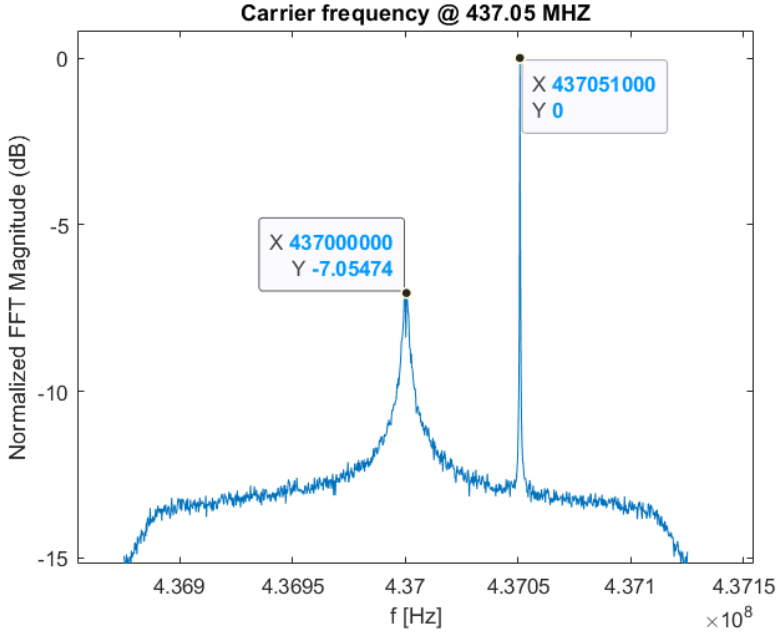


Figure 5.9: Carrier at 437.05 MHz read by USRP-2901, with center frequency of 437 MHz.

Table 5.1: Chirp signal setting.

Name	Symbol	Value	Unit
Center frequency	f_C	437	MHz
Bandwidth	B	500	kHz
Frequency step	Δf	1	kHz
Sweep time	Δt	10	ms

$$T_{chirp} = N_{STEPS} \cdot \Delta t = \frac{B}{\Delta f} \cdot \Delta t \quad (5.5)$$

To ensure that a single binary file contains sufficient samples to represent the entire frequency range covered by the chirp signal, first the number of FFT windows N_{STAB} is considered, where a single frequency of the chirp signal is stable. For example, if $N_{STAB} = 5$, this means that the GNU Radio application samples 5 FFT windows where the chirp signal has a fixed frequency and saves them inside the binary file. Assuming that N_{STAB} and T_{chirp} are known, the number of FFT windows N_{WIN} is computed as depicted in Equation 5.6, where T_{WIN} is the time

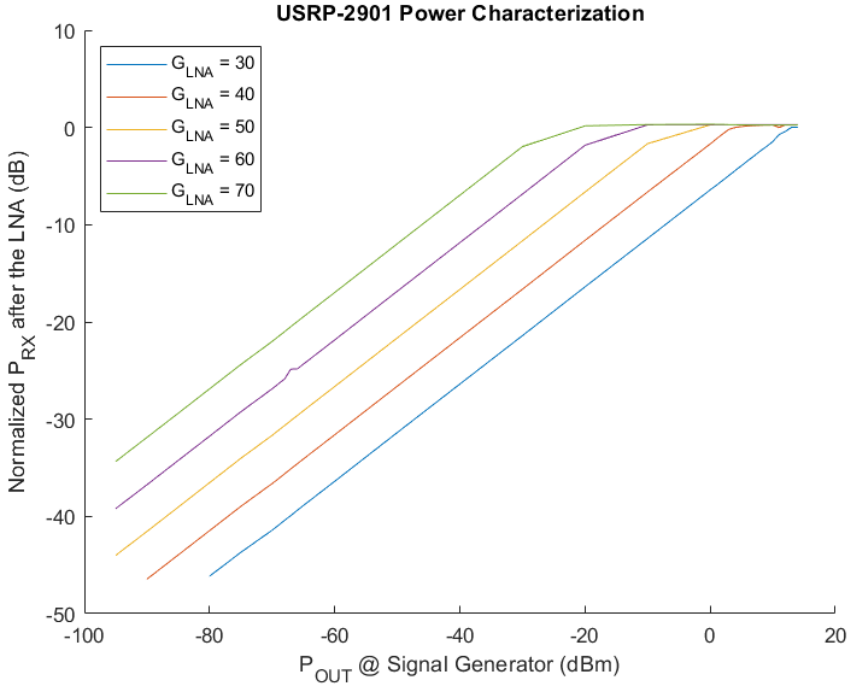


Figure 5.10: Relation between received power by USRP-2901 and transmitted power by the signal generator. A LNA gain value (dB) is assigned for each pattern.

interval of a single FFT window, f_s is the sample rate and $Nfft$ is the numbers of bins in a window.

$$\begin{aligned}
 T_{chirp} = T_{WIN} \cdot N_{STAB} \cdot N_{WIN} \rightarrow N_{WIN} &= \frac{T_{chirp}}{T_{WIN} \cdot N_{STAB}} \\
 &= \frac{B}{\Delta f} \cdot \frac{\Delta t}{T_{WIN} \cdot N_{STAB}} \\
 &= \frac{B}{\Delta f} \cdot \frac{\Delta t \cdot f_s}{Nfft \cdot N_{STAB}}
 \end{aligned} \tag{5.6}$$

By using the data as depicted in the list below:

- f_s : 500 KS/s;
- $Nfft$: 1024;
- Window: Rectangular;

– $N_{STAB} = 5$.

it is possible to obtain $N_{WIN} = 489$. In order to upload two chirp time intervals, N_{WIN} (`nwin`) is set to 1000, as shown in Figure 5.8.

The result is depicted in Figure 5.11. The plot shows frequency responses in function of different transmitted power levels by fixing the LNA gain at 40 dB. Each result shows an almost constant ripple. This is a normal behavior for digital and analogue filters, so any anomalies are detected. It can be seen that some results are overlapped (i.e. the results with transmitted power 5, 10 and 14 dBm) due to the compression behavior of the LNA.

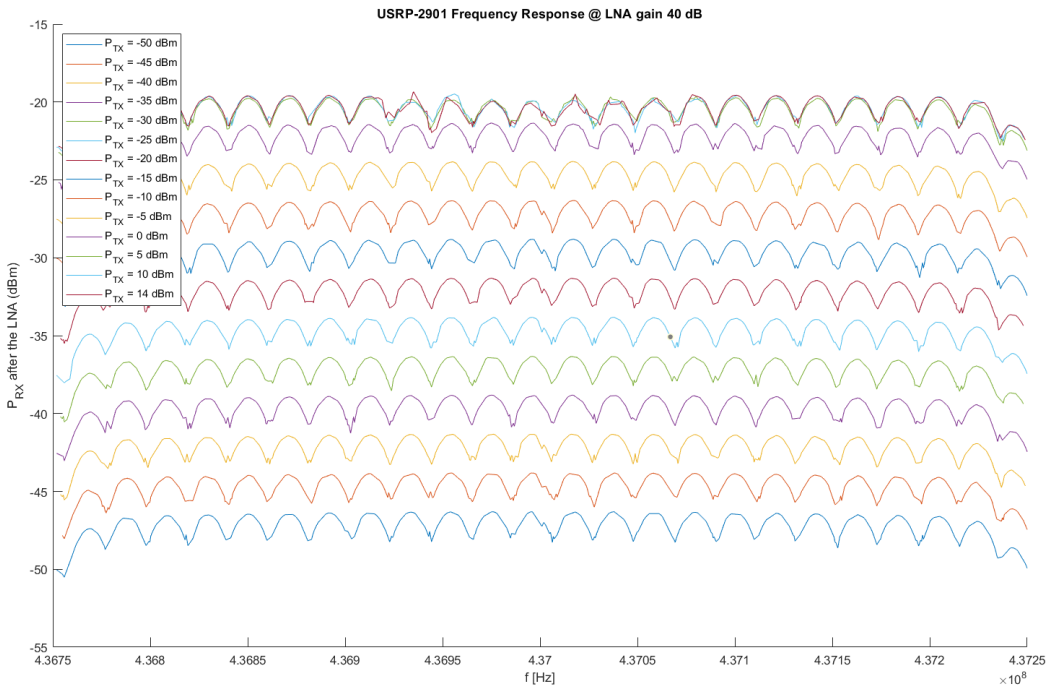


Figure 5.11: Frequency response of the LNA @ 40 dB.

Finally, we calibrate the IQ and DC offset by using the application `USRP_Calibration_RX.grc` as shown in Figure 5.12. In order to set the proper offset values, the system variables are defined in the following list:

– *IQ Imbalance*: the variables are `i_offset` and `q_offset`. The first one is

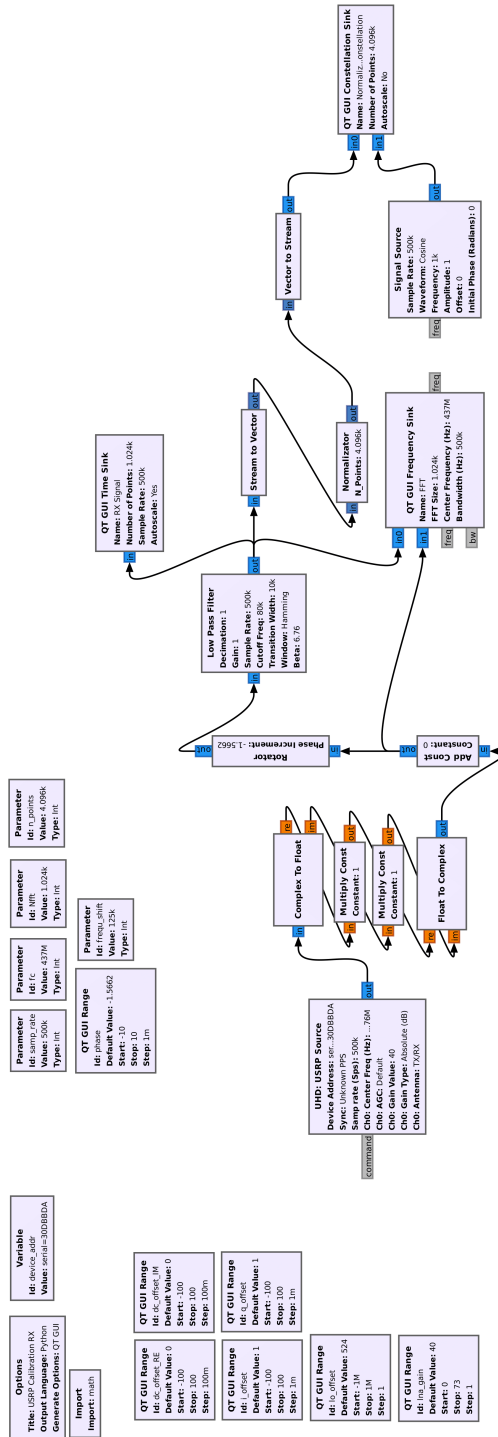


Figure 5.12: USRP_Calibration_RX.grc.

a constant multiplier to the in-phase line (i.e. the real part of the samples received by the *USRP Hardware Driver (UHD) USRP Source* block) and the second one is for the quadrature line (i.e. the imaginary part of the samples received by the *UHD USRP Source* block). Figure 5.13a shows an example of IQ imbalance by means of the visualization of a normalized constellation plot. In this case, the red pattern shows a perfect IQ balanced line, instead the blue pattern exhibits an ellipse, due to the fact that the in-phase line has a higher gain with respect to the quadrature line. By properly tuning the two gains, it is possible to obtain a perfect circle in the constellation plot;

- *DC Offset Calibration*: the variables are `dc_offset_RE` and `dc_offset_IM`. They are added to the incoming signal to remove an eventual DC misalignment. Figure 5.13b shows an example of DC offset not properly set. The result is a circle not centered in the constellation plot. In the reported case, it is evident that the quadrature line has a spurious DC component, causing a shift away from axes origin;
- *LO Calibration*: the variable is `lo_offset`. The variable is added to the center frequency set inside the *UHD USRP Source* block.

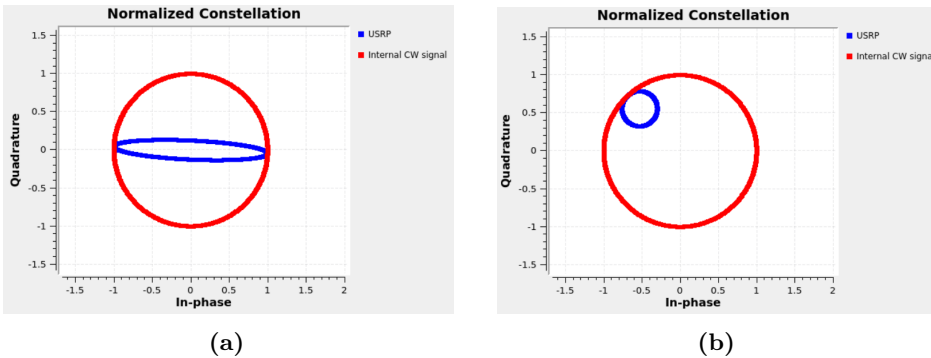


Figure 5.13: Example of IQ imbalance (a) and DC misalignment (b).

The results is discussed hereafter. Firstly, a LNA value of 40 dB is chosen as already discussed. A strong enough carrier at 437 MHz is generated by using the signal generator, as depicted in Figure 5.6. To avoid the interference at the center frequency, the USRP-2901 is shifted by -50 kHz, as shown in Figure 5.14. Finally, a LO offset of 524 Hz is found.

Secondly, DC and IQ are calibrated together. Thus, we focused on the normalized constellation. A single carrier at 437 MHz is generated as usual. In this case, `frequ_shift` is set to -125 kHz in order to have enough spacing between the generated carrier and the spurious entity (see Figure 5.14). Then, the *Rotator* block is used

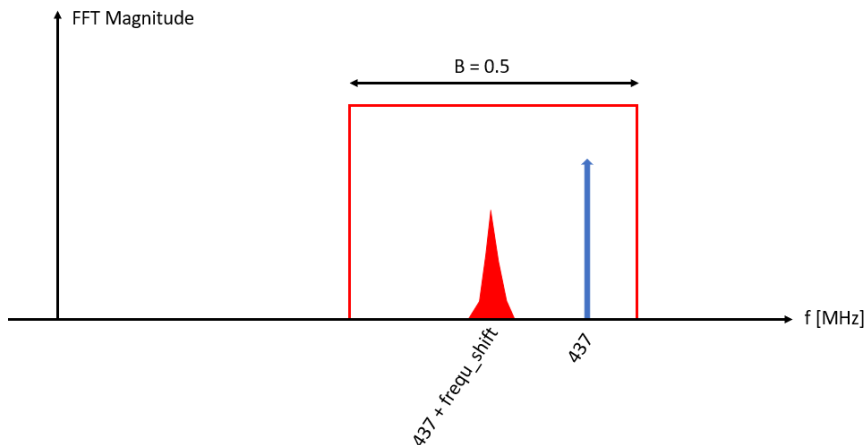


Figure 5.14: Visualization of the frequency setup for the LO calibration.

to phase-shift the baseband signal, leading to a frequency-shift at the center of the spectrum. Then, the inclusion of a *Low-Pass (LP) Filter* block proves advantageous in reducing the impact of spurious signals, isolating the generated carrier frequency. The parameters of the LP filter are shown in Table 5.2.

Table 5.2: LP filter parameters.

Name	Value	Unit
Decimation rate	1	-
Gain	1	-
Cutoff frequency	80	kHz
Transition width	10	kHz
Window type	Hamming	-

The necessity for a normalized constellation arises due to the requirement of overlapping the perfect circle (red pattern) generated by the *Signal Source* block with the real constellation (blue pattern), shown in Figure 5.13. The block generates a complex cosine function of 1 kHz and unitary amplitude. Since GNU Radio Companion does not provide a normalized constellation, it was necessary to implement a custom Python code inside the application. The block is called *Normalizator*, and it takes as input a vector of 4096 complex samples, i.e. the output of the *Stream to Vector* block, and computes the magnitude of each complex sample and finds the maximum value. Then, it divides the entire vector by the scalar value found previously and it forwards the result to the output port.

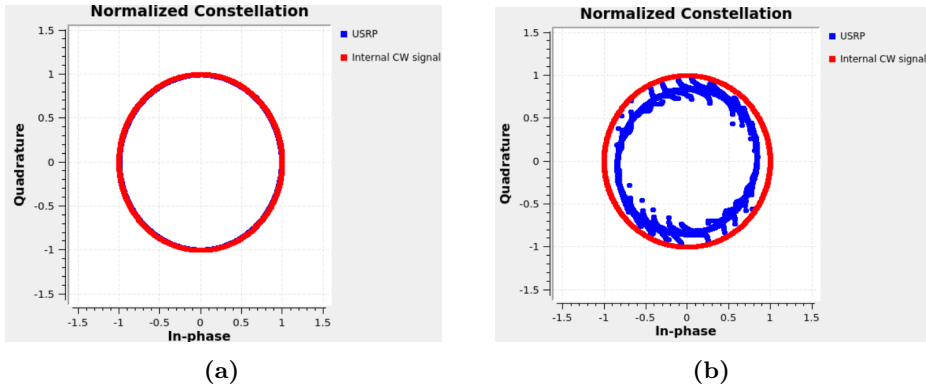


Figure 5.15: Constellation before (a) and after (b) 2 dBm of transmitted power.

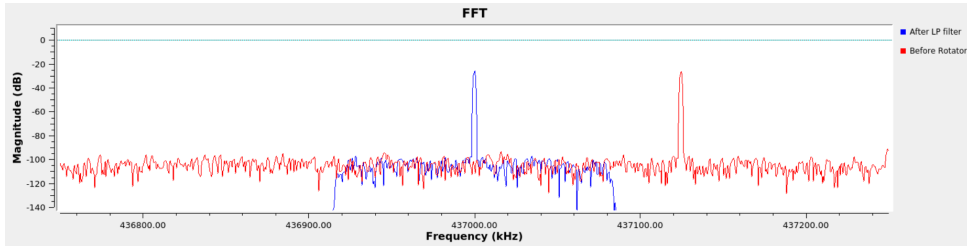


Figure 5.16: FFT magnitude of the baseband spectrum before the Rotator block and after the LP filter.

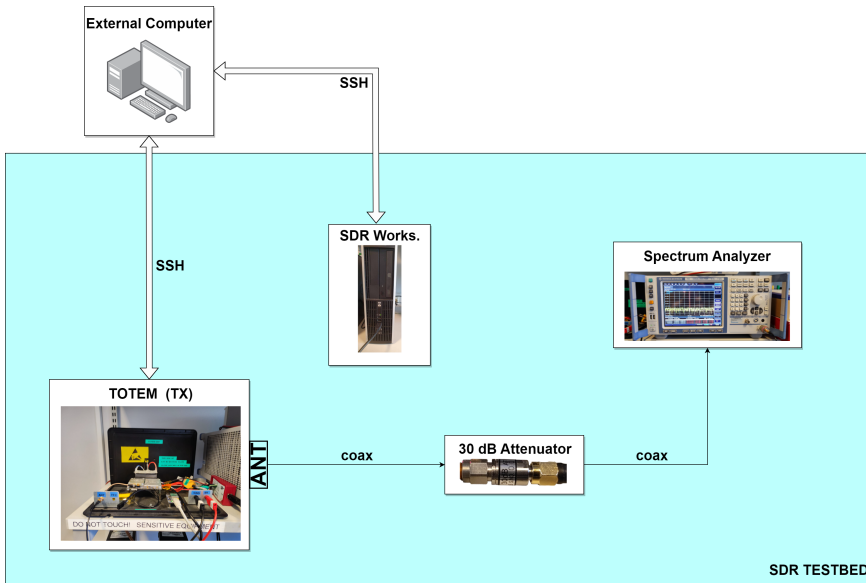
The results of this phase are shown in Figures 5.15 and 5.16. Figure 5.16 shows the frequency-shift and the LP filter effect (blue pattern). The result in the normalized constellation is depicted in Figure 5.15a. The first noticeable observation is the excellent isolation of the carrier frequency. This is an important aspect since the spurious entity can cause a degradation of the channel sounder system.

From Figure 5.15 one can notice that when the output power P_{OUT} from the signal generator exceeds 2 dBm, the points in the constellation are no longer distributed around the unitary circle, indicating that the LNA is no longer in its linearity region. It proves that when the output power is less than or equal to 2 dBm, the response is clear and well-calibrated, as already shown in Figures 5.10 and 5.11.

In conclusion, to avoid any compression of the received signal, it is necessary to set the LNA to 40 dB, and the maximum input power (P_{IN}) at the USRP-2901 should not exceed $P_{IN,compression} = P_{OUT,compression} - L_{ALL} = 2 - 34.52 = -32.52$ dBm. Table 5.3 summarizes the results obtained from this phase.

Table 5.3: Results from calibration and characterization procedures of the USRP-2901 as receiver, with LNA gain equal to 40 dB.

Name	Value	Unit
LO offset	524	Hz
IQ offset	$0 + j0$	-
DC offset	$0 + j0$	-
Compression point ($P_{IN,compression}$)	-32.52	dBm

**Figure 5.17:** Setup for the characterization and calibration of the TOTEM SDR as a transmitter.

5.3.2 TOTEM SDR as transmitter

This Section presents the procedure for calibrating and characterising TOTEM SDR as a transmitter. The calibration entities described in Section 5.3.1 are applicable to this phase as well. Figure 5.17 illustrates the setup designed for TOTEM SDR.

In the first place, the characterization of the Power Amplifier (PA) is performed, therefore finding the compression point. The application used for this characterization, named `TOTEM_Calibration_CARRIER_TX.grc`, is depicted in Figure 5.18. The application generates a simple complex cosine waveform centered at 437 MHz. The parameter `fc_offset_TX` is utilized to adjust the distance between the LO frequency and the generated carrier, as shown in Figure 5.14, where `freq_shift` and `fc_offset_TX` are equivalent.

The first step is to find the LO offset, ensuring that the generated signal is precisely centered at 437 MHz. A frequency offset of 640 Hz is identified, as depicted in Figure 5.18, where the parameter `lo_offset` represents the frequency shift applied.

Figure 5.19 shows the outcomes of this calibration step. The graph illustrates the relationship between the power received by the signal analyzer (see Figure 5.17) and the configured PA gain via the *Soapy Sink* block (see Figure 5.18). To accomplish this, the PA gain value is varied from 0 to 89 dB with an increment of 5 dB. It can be observed that the compression phase initiates at approximately 75 dB.

Figure 5.20 illustrates the outcomes following the calibration process for IQ balancing and DC offset. The results are obtained by visualizing the constellation diagram using the signal analyzer. Similar to the calibration process for USRP-2901, no modifications are required since the hardware is correctly calibrated. It is noteworthy how the distribution of points around the constellation changes from Figure 5.20a to Figure 5.20b. Indeed, the non-linearity is evident from Figure 5.20b when the PA gain overtakes 75 dB, consistent with the graph depicted in Figure 5.19.

As a concluding remark, it is important to observe the spectrum capture illustrated in Figure 5.21. As previously discussed, SDR devices tend to produce interference in the vicinity of the LO frequency, as explained in Section 5.3.1. Hence, to mitigate this issue, a decision is made to position the LO frequency at a significant distance away from the generated carrier frequency. It is noticeable that the intensity of interference exceeds the noise floor when the PA gain value reaches 15 dB. Moreover, the peak value of the interference is 35 dB lower than the peak of the generated carrier signal.

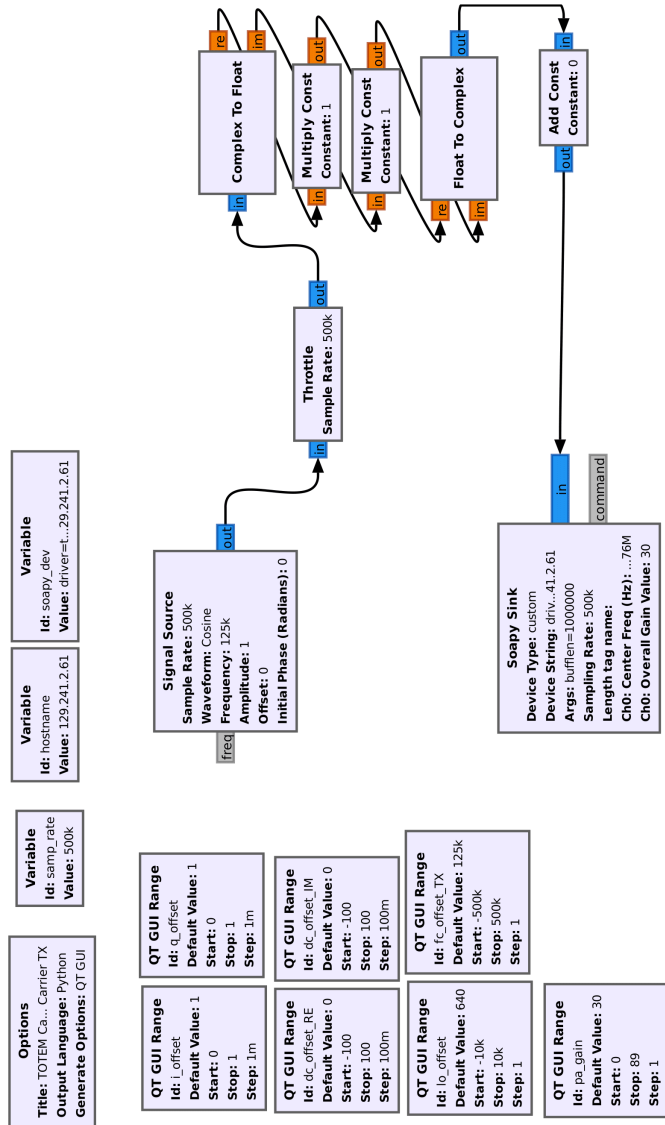


Figure 5.18: TOTEM_Calibration_CARRIER_TX.grc.

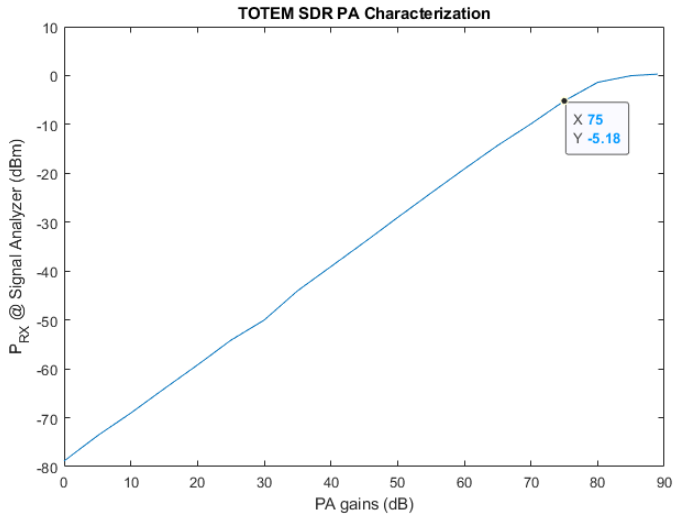


Figure 5.19: Relation between received power by the signal analyzer and transmitted power by TOTEM SDR.

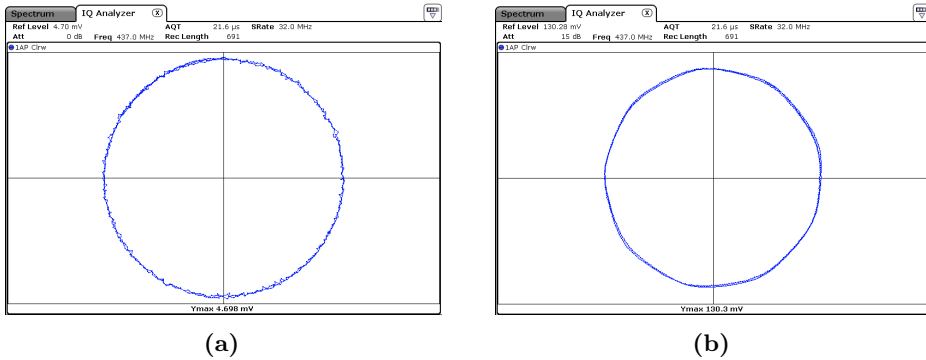


Figure 5.20: Constellation before (a) and after (b) PA gain equal to 75 dB.

5.4 Hardware-in-the-loop testing

This Section focuses on the utilization of the testbed setup depicted in Figure 5.1, where TOTEM SDR is used as transmitter. Specifically, it discusses the incorporation of back-to-back measurements into the final results, i.e. the use of the post-processing algorithms implemented in the Matlab simulator (see Section 4.7). As an additional analysis, the USRP-2901 is employed as transmitter instead of TOTEM SDR. A comprehensive performance comparison between the two setups is presented in Section 5.4.3.

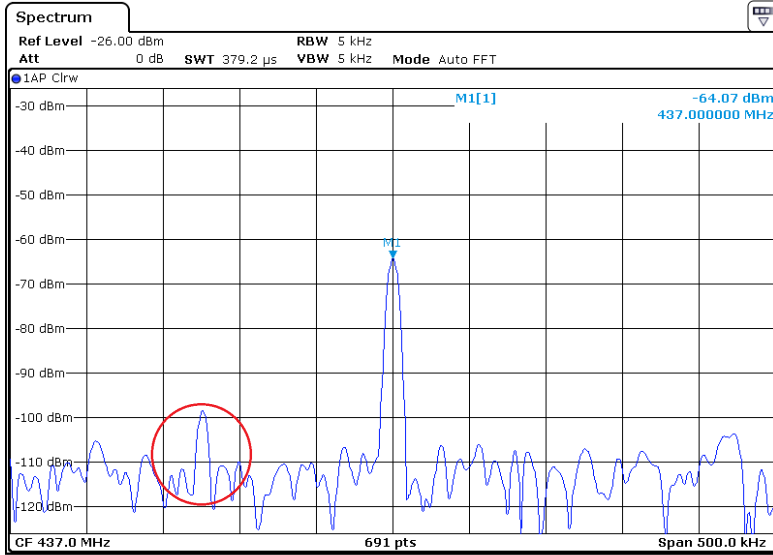


Figure 5.21: Interference due to the LO of TOTEM SDR captured by the signal analyzer. The PA gain is set to 15 dB.

5.4.1 Back-to-back measurement

Back-to-back measurements are employed to assess the filtering impact of the system components. In this approach, the transmitter and receiver are directly connected, ensuring no distortion from the transmission channel. Let $H_{RX}(f)$ and $H_{TX}(f)$ represent the frequency responses of the receiver and the transmitter (see Figure 5.22), respectively. The relationship in the frequency domain between the received signal $P_R(f, t)$ and the transmitted signal $P_T(f)$ can be derived as depicted in Equation 5.7, where $H(f, t)$ is the channel entity.

$$P_R(f, t) = H_{SYS}(f, t) \cdot P_T(f) = H_{RX}(f) \cdot H(f, t) \cdot H_{TX}(f) \cdot P_T(f) \quad (5.7)$$

It is possible to assume that the filtering effect of a direct connection between transmitter and receiver is $H(f, t) = 1$, without considering the thermal noise. Hence, the resulting system channel entity $H_{SYS}(f, t)$ is influenced by the transmitter and the receiver filters only, as depicted in Figure 5.22b.

5.4.2 HIL test with TOTEM SDR as a transmitter

This Section presents the results obtained from the HIL test conducted using the testbed setup depicted in Figure 5.1. The corresponding GNU Radio applications

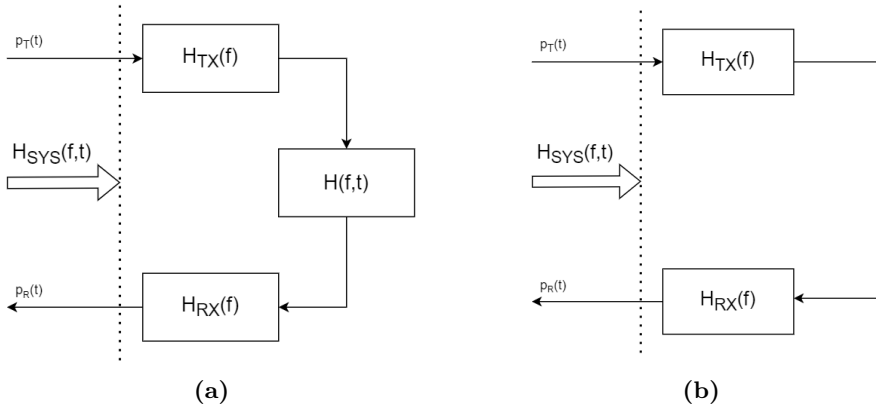


Figure 5.22: a) Example of a real channel and the equivalent filters of transmitter and receiver; b) Example of back-to-back measurement, where only the filtering entities of receiver and transmitter are considered part of the system.

utilized in this phase are illustrated in Figures 5.23 and 5.24.

The first application is designed for TOTEM SDR, based on the Pseudo-Noise (PN) sequence generator application, depicted in Figure 4.3, and the calibration application in Figure 5.18. For this experiment, the PN signal is centered to the carrier frequency $f_c = 437$ MHz (see parameter `fc`), with a LO frequency equal to $f_{LO} = f_c - f_{c,offset} + f_{LO,offset} = 436\,850\,640$ Hz (see parameters `fc_offset_TX` and `lo_offset_TX`). The application is designed to send ten PN sequences in series, in order to increase the dynamic range, as discussed in Section 4.7.2.

The second application is designed for USRP-2901, based on the calibration application in Figure 5.12. The purpose of the application is to collect the samples received by the *UHD: USRP Source* and load them into a binary file using *File Sink* block. Then, the binary file is passed the Matlab simulator for the post-processing phase.

Figure 5.25 shows the collected samples by the USRP-2901. The plot represents the PN sequence that is transmitted by the TOTEM SDR. As can be seen from the plot, the signal generated is different from the reference signal, represented by the green pattern. Two problems can be identified in the received signal:

1. Despite attempting to correct the LO leakage, it persists in the processed signal;
2. The presence of an interfering source is evident. This can be observed from Figure 5.25c, which displays the frequency domain representation of the received

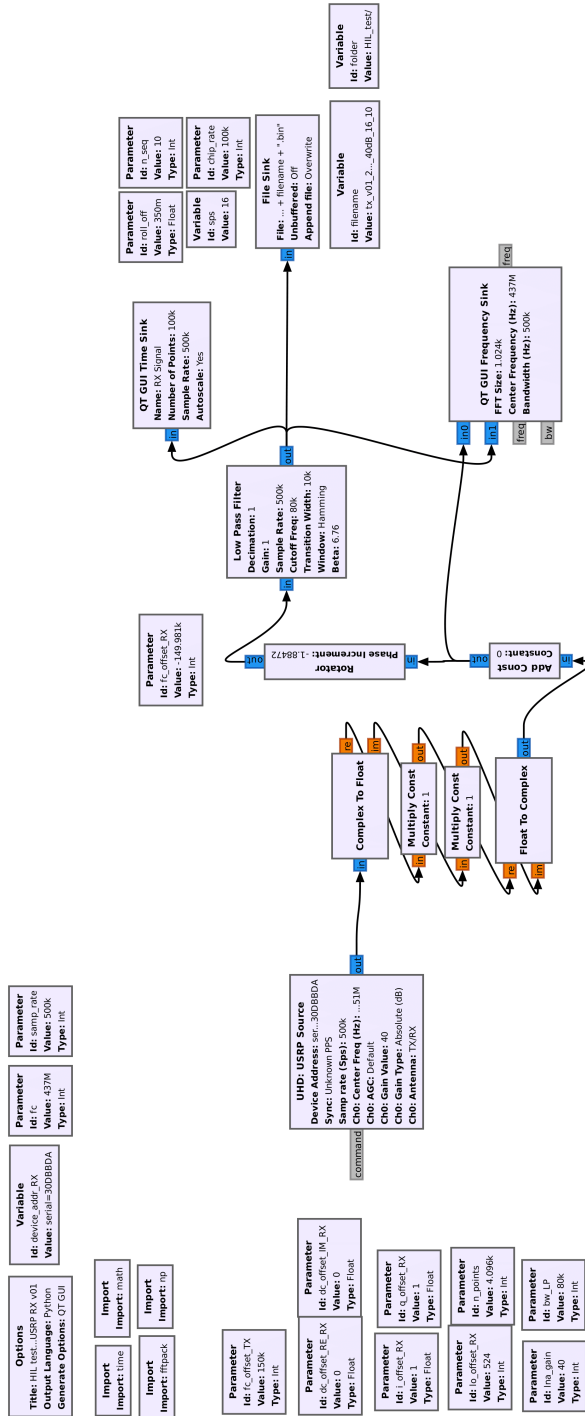


Figure 5.24: HIL_test_ChannelSounder_USRP_RX_v01.grc

signal. It is evident that the obtained pattern differs from Figure 2.11. Spikes within the spectrum are consistently present, contributing to the distortion of the received signal.

To validate the efficiency of the channel sounder, the Matlab simulator is employed for post-processing functions. To isolate the filtering effects caused by the SDR devices, all channel models are deactivated.

In order to mitigate the impact of leakage, the Doppler compensator described in Section 4.7.1 is utilized. As depicted in Figure 5.26, the signal envelope exhibits greater stability, indicating successful implementation of the frequency shift estimation and compensation.

Lastly, Figure 5.26c depicts the Channel Impulsive Response (CIR) obtained through the channel sounder algorithm described in Section 4.7.2. The result illustrates the effectiveness of the cross-correlation function, even in the presence of significant distortion in the received signal. It should be noted that the impulse is not precisely positioned at a delay time equal to zero, since there is a delay between the signal generation and the collection. Additionally, the noise floor remains relatively high (up to -30 dB), even with the use of ten PN sequences in series.

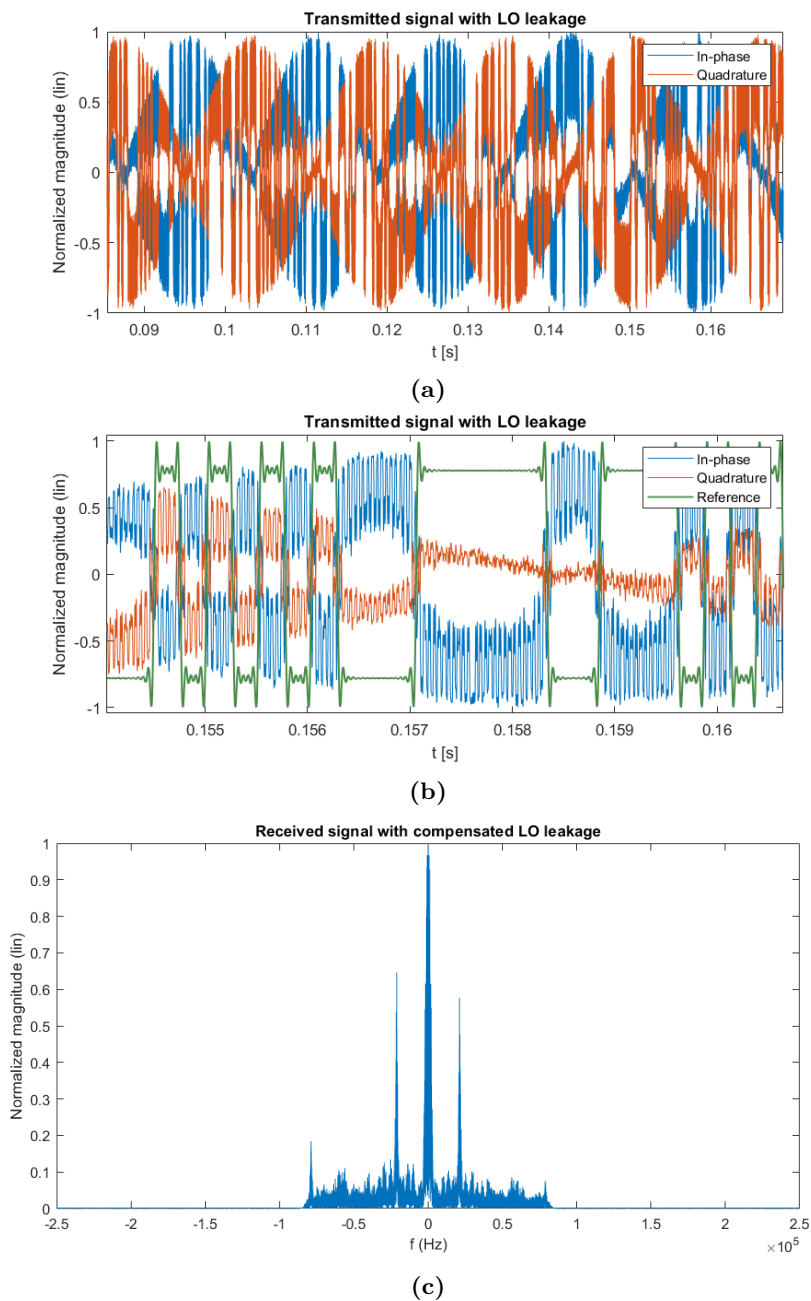


Figure 5.25: a)-b) Received samples by the USRP-2901. It is possible to notice 1) the presence of LO leakage and 2) a distortion with respect to the PN sequence generated by the GNU Radio application. Figure b) represents a close-up of figure a); c) Spectrum magnitude of the received signal.

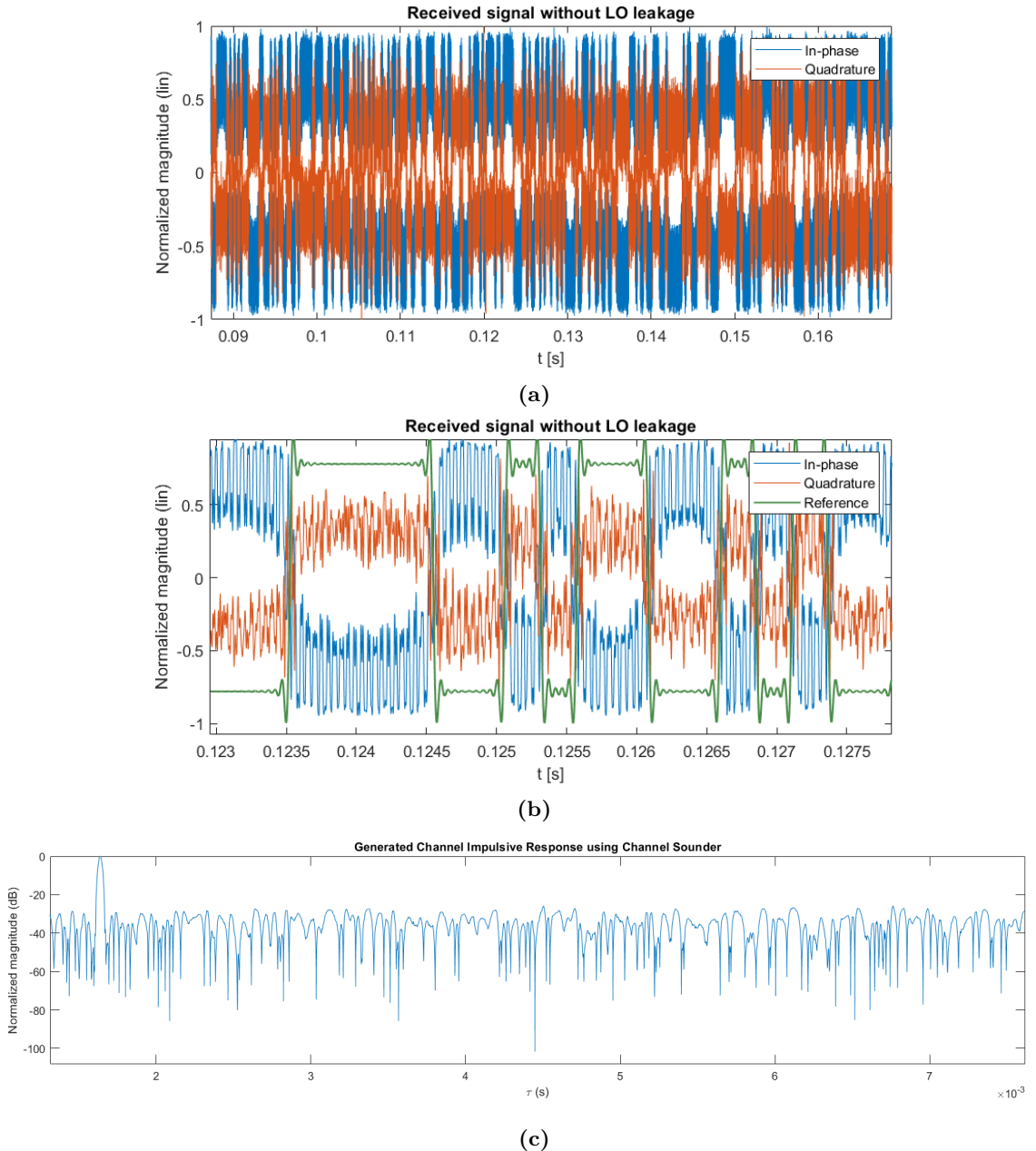


Figure 5.26: a)-b) Received sample by the USRP-2901 after the Doppler compensation algorithm. The envelope of the received signal is more stable, meaning that the LO leakage is fairly compensated, even though the distortion is still present. Figure b) represents a close-up of figure a); c) CIR obtained by using the HIL test and TOTEM SDR as transmitter.

5.4.3 HIL test with USRP-2901: comparison with TOTEM SDR

In this final step, the results obtained by implementing USRP-2901 as the transmitter instead of TOTEM SDR are discussed. The purpose of this phase is to compare the performance of the two devices in transmission. The procedures for calibration and characterising remain the same as those defined for TOTEM SDR in Section 5.3.2.

Figure 5.27 illustrates the collected PN sequence using the conventional receiver, both in time and frequency domain. It is evident that LO leakage persists, with a significant reduction in distortion compared to Figure 5.25. Notably, the received signal in the frequency domain, as shown in Figure 5.27c, closely resembles the theoretical pattern depicted in Figure 2.11.

After performing the already mentioned Doppler compensation algorithm to remove LO leakage, the result is shown in Figure 5.28. The envelope stability of the observed signal is consistent with the findings previously demonstrated in Figure 5.26. Additionally, Figure 5.28c reaffirms the effectiveness of the channel sounder algorithm in estimating the CIR. Notably, the noise floor of this case is significantly reduced, which is almost 20 dB lower compared to the TOTEM SDR solution (refer to Figure 5.26c for the previous case).

In conclusion, it can be stated that the USRP-2901 outperforms TOTEM SDR as a transmitter. However, it should be noted that further research is required to explore and improve the performance of TOTEM SDR. Additionally, it is important to highlight that unlike TOTEM SDR, the USRP-2901 is not standardized for space missions. In future studies, it is necessary to test the reported system using a more reliable and space-qualified SDR device, such as the Flight Model (FM) that is deployed on the HYPSON-2 satellite.

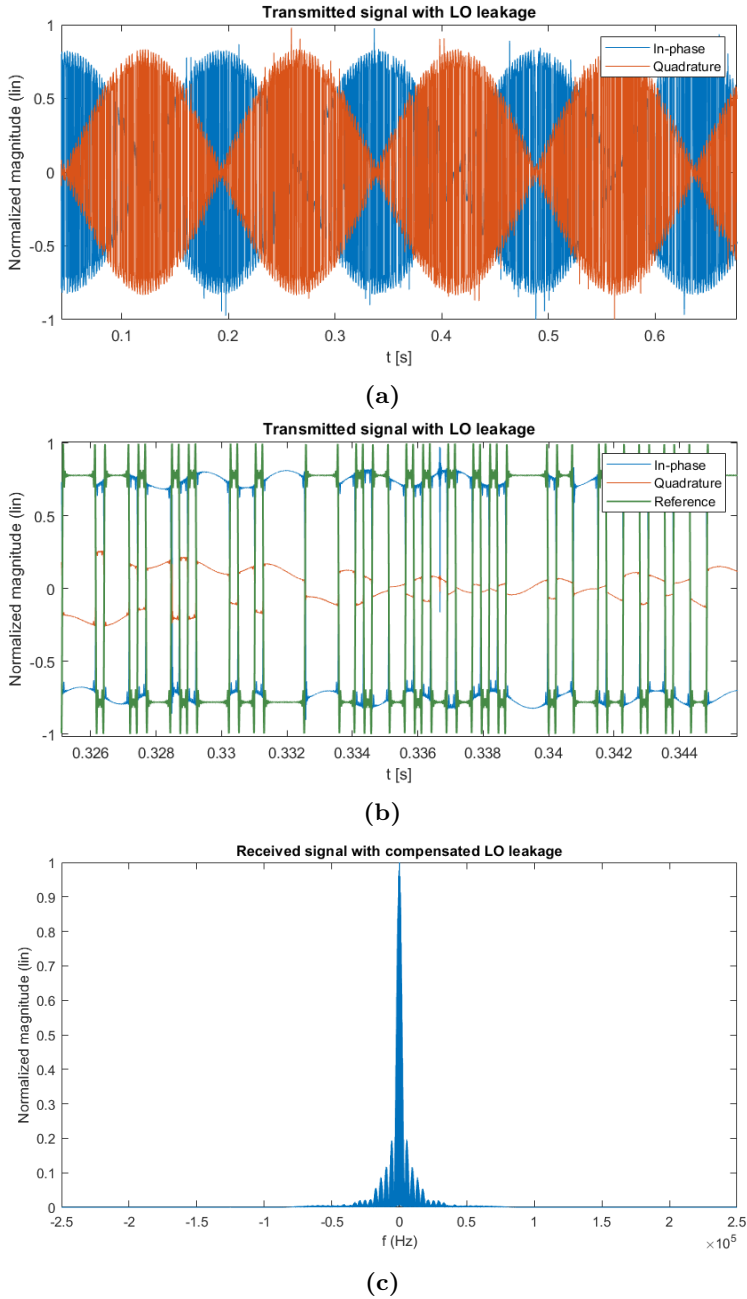


Figure 5.27: a)-b) Received samples by the USRP-2901. It is possible to notice the presence of LO leakage, but the shape of the PN sequence is visible. Figure b) represents a close-up of figure a); c) Spectrum magnitude of the received signal depicted in Figure 5.27.

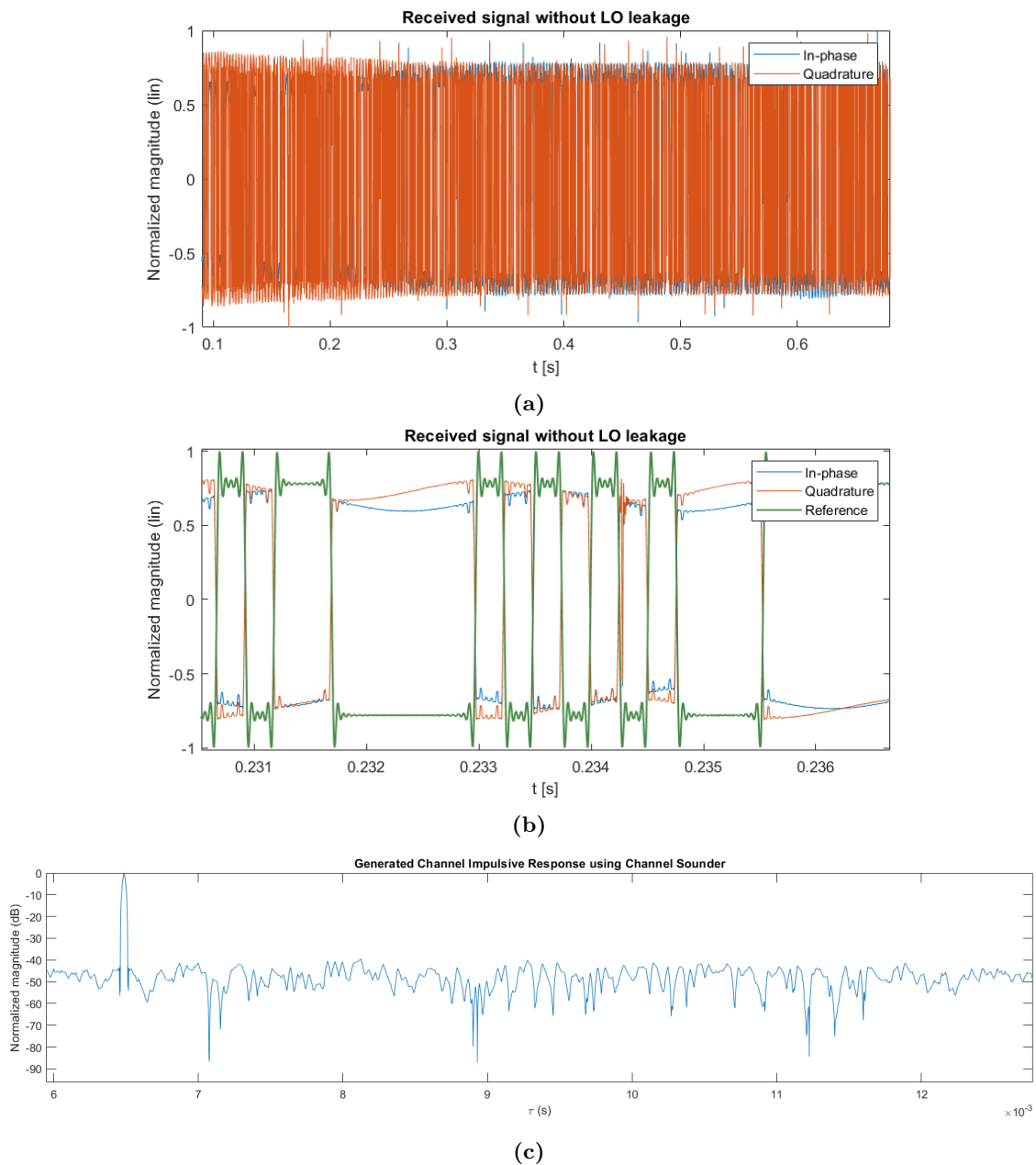


Figure 5.28: a)-b) Received sample by the USRP-2901 after the Doppler compensation algorithm. The reduction of LO leakage is evident, without the distortion observed in Figure 5.26. Figure b) represents a close-up of figure a); c) CIR obtained by using the HIL test and USRP-2901 as transmitter.

Chapter 6

Conclusion

This thesis focuses on the channel characterisation method of the Ultra High Frequency (UHF) downlink channel for Low Earth Orbit (LEO) satellites, specifically considering the influence of the ionosphere on the transmitted signal. A simulator is developed to study the behavior of the channel with respect to different channel entities, focusing on the ionospheric impact. The simulator's implementation is validated through rigorous testing and measurement of the different entities. First, the Doppler shift is estimated with a maximum deviation of 23.7256 Hz. This result is important to make efficient the channel sounding technique used to characterise the multipath effect. It has been observed that sending the same sequence multiple times in series enhances the dynamic range, and the thermal noise does not influence the cross-correlation function outcome due to the pseudo-stochastic property of the transmitted sequence. At the design stage, the choice of the Pseudo-Noise (PN) sequence length (L) and chip rate (f_{chip}) significantly impacts the channel sounder's performance, balancing the detection of slow echoes, temporal resolution and maintaining the quasi-stationarity property. Moreover, two methods are implemented to characterise ionospheric scintillation and Faraday rotation. The parameter S_4 is used for ionospheric scintillation estimation, taking into account the signal length. It is noticed how S_4 slowly converges in function of the length of the sent signal. Subsequently, a testbed is designed to validate the channel sounder by performing a Hardware-In-the-Loop (HIL) test, and methods for the calibration and characterisation of Software Defined Radio (SDR) devices are proposed. Two SDRs devices are implemented as transmitters in the testbed, i.e. TOTEM SDR and Universal Software Radio Peripheral (USRP)-2901. In both cases, the received signal has Local Oscillator (LO) leakage. In order to remove it, the Doppler compensator code is used. The algorithm estimates and compensates correctly the imbalance, proving the soundness of the implemented algorithm. The work concludes by comparing TOTEM SDR and USRP-2901 performance as transmitters, noting the latter's higher efficiency. Nevertheless, the implemented channel sounder performs as expected, successfully concluding the research conducted in this thesis.

6.1 Contribution

This Section discusses the significant contributions of this thesis.

The first major contribution is the development of a comprehensive Matlab simulator. The latter allows the simulation of various communication scenarios by incorporating the most important channel entities offered by the literature. This requirement does not fulfil the universality objective as stated. However, the entities have multiple degrees of freedom that can be defined in the design phase.

The second significant contribution is the creation of an adaptable SDR testbed. This testbed not only facilitates the validation of the proposed channel sounder but also enables the testing of various desired applications. It includes multiple configurations and GNU Radio applications, supporting the calibration and characterization of SDR devices.

Through the aforementioned artifacts, several promising results are achieved. The Matlab simulator accurately implemented all relevant channel entities and provided satisfactory validation outcomes. Real data usage further will enhance the simulator's effectiveness. Additionally, the testbed successfully validated the channel sounder, unexpectedly experiencing better performance of the USRP-2901 device over the TOTEM SDR.

Overall, the combination of the Matlab simulator, SDR testbed, and obtained results provide a valuable platform for researchers and designers. They will offer insights into communication system behavior and will help in selecting the most suitable SDR devices for future implementations in this field.

6.2 Future work

The accomplishments attained during the course of this thesis aim at contributing towards enhancing comprehension of the downlink channel characteristics for LEO satellites operating within the UHF band (in the subsequent Section, the analysis of potential future undertakings directly connected to the outcomes detailed in this thesis is detailed).

Firstly, a measurement campaign will be essential in order to validate the channel sounding technique in-orbit. This thesis provides the essential tools for comprehending the channel sounding technique and elucidates how the diverse radio applications, simulator, calibration and characterization procedures can be tailored to accommodate different equipment setups.

Precise satellite positioning information could be incorporated using Two-Line

Element (TLE) files, enabling the calculation of the exact distance between the satellite and the ground station. Indeed, instead of calculating the distance between satellite and ground station using the formula obtained, it is more versatile to use the TLE files.

Another valuable enhancement to the system will involve integrating the radiation patterns of both the ground station and the satellite antennas. By incorporating them and considering the alignment between the satellite and the ground station, a simulator can be developed to take into account the attenuation caused by antenna pointing. This ensures the simulator's universality by allowing it to be tailored to different setups and configurations.

A relevant consideration pertains to the characterization of the interference environment encountered at the ground station. Conducting a measurement campaign will become imperative to examine the extent to which the surrounding environment affects the operation of the ground station. It is of utmost importance to acquire temporal and statistical insights into the behavior of interference, facilitating the development of tailored systems that mitigate its impact on the received signal. The development of a universal method for characterizing ground station antennas proves to be fundamentally advantageous for reprocessing purposes, particularly when multiple ground stations are utilized.

The exploitation of multiple antennas will provide the opportunity to implement spatial diversity [74]. By conducting a comprehensive measurement campaign involving numerous ground stations across Norway, it will become feasible to collect data pertaining to the ionosphere from diverse spatial locations. This approach facilitates the creation of an enhanced mapping of the channel behavior in function of the space as well, enabling a more effective understanding of its characteristics and variations. Such an endeavour holds significant promise in advancing our knowledge of the ionospheric effects on the channel within a spatial context.

Moreover, a significant contribution will be made by the potential utilization of multiple ground stations, enabling a broader mapping of the ionosphere's interaction with the transmitted signal. This concept, also known as spatial diversity, finds application in various domains [75]–[77]. By employing multiple ground stations, a comprehensive understanding of the ionospheric effects can be attained, further enhancing the robustness and reliability of the communication system.

An additional aspect in characterizing the transmission channel is the estimation of the S_4 parameter discussed in Section 4.7.3. In this work, a conventional method for estimating this parameter has been proposed. However, achieving a satisfactory result in the estimation of the S_4 parameter is hampered by the presence of several intertwined channel entities and the inadequate sampling interval available for the

estimation process. As a result, there is a need to explore alternative approaches available in the literature that can be harnessed and tailored for this purpose. One such solution is the utilization of artificial neural networks or other machine learning techniques, as highlighted in prior research on ionospheric parameter estimation [26]. An alternative solution involves the utilization of the dual-frequency technique, as discussed in Section 4.7.4, wherein the same pseudo-noise sequence is transmitted across different frequency bands. This approach proves beneficial in augmenting the available samples for parameter estimation purposes. Incorporating and adapting these techniques will have the potential to enhance the accuracy of the S_4 parameter estimation in the transmission channel characterization.

References

- [1] M. B. Majed et al., «Channel characterization and path loss modeling in indoor environment at 4.5, 28, and 38 ghz for 5g cellular networks», Sep. 2018.
- [2] A. Mudonhi et al., «Mm-wave massive mimo channel sounding in industrial iot scenarios», Jul. 2022.
- [3] C. Loo et al., «Land mobile satellite channel measurements and modeling», 1998.
- [4] S. B. et al., «Hypso-1 cubesat: First images and in-orbit characterization», Jan. 2023.
- [5] M. E. Grøtte et al., «Ocean color hyperspectral remote sensing with high resolution and low latency—the hypso-1 cubesat mission», Jun. 2021.
- [6] *Cubesat 101: Basic concepts and processes for first-time cubesat developers*, Accessed: 16/04/2023, NASA, Oct. 2017. [Online]. Available: https://www.nasa.gov/sites/default/files/atoms/files/nasa_csli_cubesat_101_508.pdf.
- [7] E. Peral et al., «Raincube – a new paradigm to observe weather processes», Nov. 2019.
- [8] T. Pagano et al., «The cubesat infrared atmospheric sounder (ciras), pathfinder for the earth observing nanosatellite-infrared (eon-ir)», Feb. 2022.
- [9] V. di Tana et al., «Argomoon: There is a nano-eyewitness on the sls», Apr. 2019.
- [10] G. Quintana-Diaz et al., «In-orbit measurements and analysis of radio interference in the uhf amateur radio band from the lume-1 satellite», 2021.
- [11] G. Quintana-Diaz et al., «Detection of radio interference in the uhf amateur radio band with the serpens satellite», Oct. 2021.
- [12] S. Busch et al., «Uwe-3, in-orbit performance and lessons learned of a modular and flexible satellite bus for future pico-satellite formations», 2021.
- [13] «Nanoavionics launched three satellites, including one of the largest cubesats ever built, aboard spacex transporter-3 mission». [Online]. Available: <https://nanoavionics.com/news/nanoavionics-launched-three-satellites-including-one-of-the-largest-cubesats-ever-built-aboard-spacex-transporter-3-mission/> (last visited: Jun. 9, 2023).
- [14] «Faq: Climate change in the polar regions». [Online]. Available: https://scholar.google.com/scholar?as_ylo=2023%5C&q=arctic+global+warming%5C&hl=en%5C&as_sdt=0,5 (last visited: Apr. 24, 2023).

- [15] *Arctic connectivity working group 2021*, Arctic Economic Council, 2021. [Online]. Available: <https://arcticeconomiccouncil.com/wp-content/uploads/2021/05/aec-cwg-report-050721-6.pdf>.
- [16] T. H. Bolle, «Operationalizing testing setup used at ntnu smallsat lab», M.S. thesis, NTNU, Jun. 2022.
- [17] R. Birkeland et al., «Development of a multi-purpose sdr payload for the hypso-2 satellite», 2021.
- [18] *Recommendation itu-r p.531-14: Ionospheric propagation data and prediction methods required for the design of satellite networks and systems*, ITU-R, Aug. 2019. [Online]. Available: https://www.itu.int/dms_pubrec/itu-r/rec/p/R-REC-P.531-14-201908-I!!PDF-E.pdf.
- [19] S. K. Endresen, «A method for measuring temporal properties of uplink interference in satellite communication», M.S. thesis, NTNU, Jun. 2021.
- [20] «Reciprocity in wireless communication systems». [Online]. Available: <https://www.nt.uni-bremen.de/en/projects/reciprocity/> (last visited: Jun. 27, 2023).
- [21] M. Lin et al., «Detection of ionospheric scintillation based on xgboost model improved by smote-enn technique», Jul. 2021.
- [22] I. C. F. Müller-Wodarg, «Planetary upper atmospheres», Oct. 2005.
- [23] «The effects of earth's upper atmosphere on radio signals». [Online]. Available: <https://radiojove.gsfc.nasa.gov/education/materials/iono.htm> (last visited: Jun. 27, 2023).
- [24] A. A. Ferreira et al., «Investigation of ionospheric effects in the planning of the alfacrux uhf satellite communication system», 2022.
- [25] D. Bilitza, «International reference ionosphere: Recent developments», 1986.
- [26] A. Atabati et al., «Ionospheric scintillation prediction on s4 and roti parameters using artificial neural network and genetic algorithm», 2021.
- [27] V. E. Kunitsyn et al., «Ionospheric tec estimation with the signals of various geostationary navigational satellites», 2016.
- [28] C.B. Erol et al., «A new technique for tec estimation», 2002.
- [29] P.A. Wright et al., «Faraday rotation effects on l-band spaceborne sar data», 2003.
- [30] Y. Béniguel et al., «A global ionosphere scintillation propagation model for equatorial regions», 2011.
- [31] S. Priyadarshi, «A review of ionospheric scintillation models», 2015.
- [32] Y. H. Ho et al., «Global positioning system (gps) positioning errors modeling using global ionospheric scintillation model (gism)», 2011.
- [33] P. Hamel et al., «Kriging method combined with gism to generate ionospheric scintillation map», 2011.
- [34] W. Iftikhar et al., «Channel sounding», M.S. thesis, Halmstad University, Oct. 2008.
- [35] «Coherence bandwidth». [Online]. Available: <http://www.wirelesscommunication.nl/reference/chaptr03/cohbw/cohbw.htm> (last visited: Jul. 29, 2023).

- [36] R. J. Pirkl, «A sliding correlator channel sounder for ultra-wideband measurements», M.S. thesis, NTNU, Aug. 2007.
- [37] R. J. Pirkl et al., «Optimal sliding correlator channel sounder design», 2008.
- [38] «Galois fields and its properties». [Online]. Available: <https://www.geeksforgeeks.org/galois-fields-and-its-properties/> (last visited: Jun. 18, 2023).
- [39] M. Redeker et al., «Using glfsrs for pseudo-random memory bist», Oct. 2000.
- [40] J. Mathew et al., «Attack tolerant cryptographic hardware design by combining error correction and uniform switching activity», May 2013.
- [41] V. Dear et al., «Design of sliding correlator channel sounder for ionospheric channel probing based on software define radio», 2020.
- [42] G. Q.-D. et al., «Satellite uplink interference measurements in the 437 mhz uhf amateur radio band onboard lume-1», Jun. 2021.
- [43] «Docker overview». [Online]. Available: <https://docs.docker.com/get-started/overview/> (last visited: Apr. 18, 2023).
- [44] J. Tapparel et al., «An open-source lora physical layer prototype on gnu radio», 2020.
- [45] S. Xu et al., «Software-defined next-generation satellite networks: Architecture, challenges, and solutions», 2018.
- [46] G. Baldini et al., «Security aspects in software defined radio and cognitive radio networks: A survey and a way ahead», 2011.
- [47] R. Akeela et al., «Software-defined radios: Architecture, state-of-the-art, and challenges», 2018.
- [48] «Ops-sat». [Online]. Available: https://www.esa.int/Enabling_Support/Operations/OPS-SAT (last visited: Jun. 23, 2023).
- [49] «Gnu radio companion». [Online]. Available: <https://www.gnuradio.org/about/> (last visited: Apr. 24, 2023).
- [50] A. Bannour et al., «An sdn solution for a geo and leo satellite transceiver based on gnu radio companion», Dec. 2021.
- [51] A. Løfaldli et al., «Implementation of a software defined radio prototype ground station for cubesats», Apr. 2016.
- [52] D. W. Wangsa et al., «Tracking telemetry and command using software defined radio with nano-satellite parameters», Sep. 2019. [Online]. Available: <https://dx.doi.org/10.1088/1757-899X/620/1/012095>.
- [53] *Frontenduhf*, Issue: 2.0, Alén Space, Apr. 21, 2021.
- [54] *Totem - motherboard*, Issue: 1.1, Alén Space, Apr. 28, 2021.
- [55] *Ad9364 - rf agile transceiver*, Analog Devices, Jan. 1, 2016. [Online]. Available: <https://www.analog.com/media/en/technical-documentation/data-sheets/ad9364.pdf>.
- [56] «Soapysdr». [Online]. Available: <https://github.com/pothosware/SoapySDR/wiki#client-api> (last visited: Apr. 24, 2023).
- [57] D. Gutiérrez et al., «Measurement of 4g lte cells with sdr technology», Feb. 2020.

- [58] A. Ibanez et al., «5g broadcast sdr open source platforms», 2022.
- [59] *Usrcp-2901 specifications - national instruments - nubilightt*, Accessed: 23/02/2023, National Instruments, Jul. 13, 2017. [Online]. Available: <https://nubilight.nubicom.co.kr/upload/datasheet/374925c.pdf>.
- [60] B. L. E. Mendez, «Link budget for ntnu test satellite», M.S. thesis, NTNU, Jul. 2013.
- [61] G. Máral & M. Bousquet, *Satellite Communications Systems*. 2009.
- [62] J. D. Kraus, *Antennas*.
- [63] L. J. Ippolito, *Modeling and prediction of atmospheric propagation effects from satellite beacons*, Stanford Telecom, 1994.
- [64] K. Davies, *Ionospheric Radio*. 1990.
- [65] R. Galuscak et al., «Circular polarization and polarization losses»,
- [66] HYPISO Project Team, *Hypso-2 sdr antenna design repor*, SmallSat Lab, Aug. 29, 2022.
- [67] «Signals and systems: Properties of fourier transform». [Online]. Available: <https://www.philadelphia.edu.jo/academics/qhamarsheh/uploads/Lecture%5C%2017%5C%20Properties%5C%20of%5C%20Fourier%5C%20Transform.pdf> (last visited: Jun. 23, 2023).
- [68] «Convolution». [Online]. Available: <http://ecweb1.rutgers.edu/~gajic/solmanual/slides/chapter6C.pdf> (last visited: Jun. 23, 2023).
- [69] «Dynamic range». [Online]. Available: https://ccrma.stanford.edu/~jos/st/Dynamic_Range.html#:~:text=The%5C%20dynamic%5C%20range%5C%20of%5C%20a,noise%5C%20level'%5C%20in%5C%20dB. (last visited: Jun. 23, 2023).
- [70] J. M. Juan et al., «A method for scintillation characterization using geodetic receivers operating at 1 hz», 2017.
- [71] «Market understands value of dual frequency». [Online]. Available: <https://www.euspa.europa.eu/newsroom/news/market-understands-value-dual-frequency#:~:text=Dual%5C%20frequency%5C%20capability%5C%20means%5C%20that,can%5C%20be%5C%20used%5C%20as%5C%20backup.> (last visited: Jun. 23, 2023).
- [72] *Totem frontend-uhf datasheet*, Issue: 1, Alén Space, Oct. 8, 2018.
- [73] G.K. Gothard et al., *Time Domain Electromagnetics*. 1999.
- [74] «Antenna diversity basics». [Online]. Available: <https://www.rfwireless-world.com/Articles/Antenna-diversity-basics-and-diversity-types.html> (last visited: Jun. 26, 2023).
- [75] K. Zeng et al., «Exploiting multiple-antenna diversity for shared secret key generation in wireless networks», 2010.
- [76] *Using antenna diversity to create highly robust radio links*, Silicon Labs, 2009.
- [77] R. L. Mahany, «Network utilizing modified preambles that support antenna diversity», pat. US5748676A, 1995.

- [78] «Advanced electromagnetic ray tracing methods». [Online]. Available: <https://www.ee.cit.tum.de/hft/forschung/advanced-electromagnetic-ray-tracing-methods/advanced-electromagnetic-ray-tracing-methods/> (last visited: Jun. 18, 2023).
- [79] J. B. Schneider, *Understanding the Finite-Difference Time-Domain Method*. Dec. 2022.
- [80] D. Bykhovskiy, «Coherence time evaluation in indoor optical wireless communication channels», Sep. 2020.
- [81] C. A. Balanis, *Antenna theory: analysis and design (3rd edition)*. 2005.
- [82] «Solid angle». [Online]. Available: http://math_research.uct.ac.za/~siphelo/admin/interferometry/2%5C_Mathematical%5C_Groundwork/2%5C_12%5C_solid%5C_angle.html (last visited: Jun. 27, 2023).
- [83] A. Pal, «Low profile pattern reconfigurable square loop antenna», Feb. 2013.
- [84] M. M. Alani, *OSI Model*. Springer Nature, 2014.
- [85] «The cubesat space protocol». [Online]. Available: https://docs.kubos.com/1.2.0/apis/libcsp/csp_docs/overview.html (last visited: Apr. 17, 2023).
- [86] *Introduction to the controller area network (can)*, Revised May 2016, Texas Instruments, Aug. 2022.
- [87] *Rfc 4251: The secure shell (ssh) protocol architecture*, Accessed: 17/04/2023, Network Working Group, Jan. 2006. [Online]. Available: <https://www.rfc-editor.org/rfc/rfc4251>.
- [88] «The ssh protocol». [Online]. Available: <https://www.ssh.com/academy/ssh> (last visited: Jun. 23, 2023).
- [89] S. Bakken et al., «Software development and integration of a hyperspectral imaging payload for hypso-1», Feb. 2022.
- [90] HYPSONO Project Team, *2021-05-28 hypso - learning to use*, SmallSat Lab, Aug. 29, 2022.
- [91] «Run your image as a container». [Online]. Available: <https://docs.docker.com/language/golang/run-containers/#:-:text=Run%20in%20detached%20mode&text=Docker%20can%20run%20your%20container,you%20to%20the%20terminal%20prompt> (last visited: Jul. 5, 2023).
- [92] «Docker run». [Online]. Available: <https://docs.docker.com/engine/reference/commandline/run/#device> (last visited: Jun. 19, 2023).
- [93] «Volumes». [Online]. Available: <https://docs.docker.com/storage/volumes/> (last visited: Jun. 19, 2023).

Appendix

Fundamentals of Radio Propagation Modeling

This Chapter delves into various aspects concerning the transmission of the electromagnetic field in wireless communication. It explores fundamental concepts, such as the distinction between deterministic and stochastic transmission channels, the definition of the Channel Impulsive Response (CIR), and the concept of quasi-stationarity. Furthermore, it thoroughly examines the multiple effects present in the propagation channel that are relevant to this thesis.

A.1 Channel Modeling

In telecommunications, a communication channel is described as a pathway passed through by a signal generated by a transmitter, which at the end is collected by a receiver entity. Many different channel models have been defined for different environments (e.g. rural, urban, satellite-to-earth) and frequencies. A relevant set of entities that affects the signal quality is defined in this section.

Channel modeling involves the characterization of propagation channels to determine the extent of temporal “smearing” and spatial fading. There are two different types of channel modeling, which take vastly different approaches to understanding channel behavior. The first is the *deterministic* channel modeling [36], which is a theoretical approach that examines how exactly the electromagnetic energy travels from a transmitter to a receiver in a particular environment (see Figure A.1). The second is the *stochastic* channel modeling [36], which is an experimental approach that aims to produce a general description of the wireless channel for multiple environmental types.

To describe a channel, it is convenient to refer either to the CIR $h(\tau, t)$ [36] for the time domain, or $H(f, t)$ in the frequency domain. Depending on the channel, $h(\cdot)$ and $H(\cdot)$ can be stochastic processes or deterministic. Furthermore, time-dependency is a crucial factor to be considered in order to have the best communication link

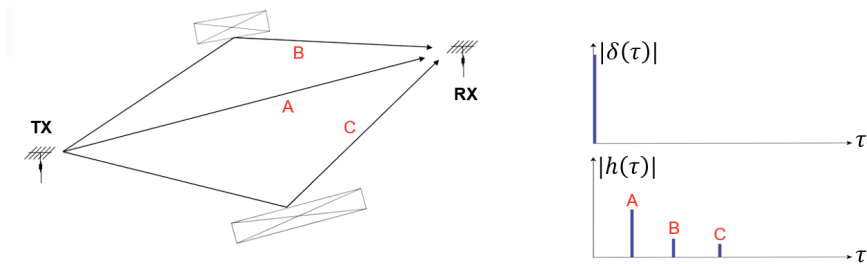


Figure A.1: Example of a deterministic channel model. The system is static and the transmitter generates a pulse signal at delay time $\tau = 0$ s (see right-up plot). Due to the reflection of the transmitted signal, the receiver perceives a set of pulses, defined by a certain delay and amplitude (see right-bottom plot)

quality. Time-variant channels are used to modify their stochastic properties over time, making the channel characterization process more challenging.

A.1.1 Deterministic channels

Deterministic channel modeling involves describing the wireless channel using the principles of electromagnetism and optics. This approach requires a 2-D or 3-D model of the physical environment, as well as information on major scatterers and their material composition. Once the location of the transmitter and receiver is determined, techniques for instance ray-tracing [78] or Finite-Difference Time-Domain (FDTD) [79] are utilized to analyze the exact pathways that electromagnetic energy follows as it travels from the transmitter to the receiver. Although computationally intensive, these methods can yield highly accurate results, making deterministic channel modeling particularly useful for studying the fundamental physics of radio propagation. An example of a widely used tool is the CST Studio Suite, which is based on the FDTD.

A.1.2 Stochastic channels

Stochastic channel modeling characterizes the wireless channel as a random process in terms of space, time, and frequency. This approach necessitates gathering a significant amount of measurement data to determine the behavior of the stochastic process through the use of probability density functions and power spectral densities. Stochastic channel models cannot produce an exact depiction of the wireless channel at a specific location. Instead, they offer an anticipated representation of the channel's behavior in a particular environment.

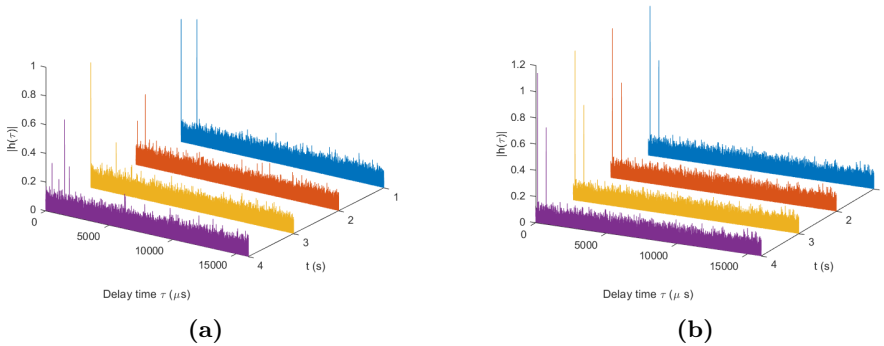


Figure A.2: An example of time-variant (a) and static (or time-invariant) channel (b).

A.1.3 The Quasi-Stationarity condition

Channels can be classified into further two categories: static and time-variant. A time-variant channel is a type of propagation channel in which the characteristics of the channel, for instance attenuation, distortion, and noise, change over time. An example of a time-variant channel is a satellite channel or a mobile channel. It is still possible that a time-variant channel can be interpreted as quasi-static. This is possible by considering the so-called coherence time T_{COH} . The coherence time [80] is a measure of the temporal stability of the wireless channel. In order to guarantee the quasi-stationarity condition, the signal time interval T_{TX} (i.e. the interval of time to transmit the signal) must respect the following relation:

$$T_{\text{TX}} \ll T_{\text{COH}} \quad (\text{A.1})$$

It is important to note that the coherence time is specific to each wireless channel and can vary depending on many factors, for example, the propagation environment, carrier frequency, and the speed of the mobile devices. Therefore, it is typically estimated through measurements or channel modeling based on the specific deployment scenario.

A.2 Antenna characterization

An antenna is a device or structure designed to transmit or receive electromagnetic waves. It is fundamental that during the design phase of the antenna for the spacecraft, all the parameters must be tuned in function of the propagation channel. Hereafter, the fundamental parameters are introduced.

A.2.1 Power flux density and Radiation intensity

The power flux density p [81] is defined as the ratio between the power that flows in an area unit, considering a unit of bandwidth. In order to understand the concept, an isotropic antenna is defined as a radiator capable to emit the same power P_0 in all directions, which is an ideal antenna and does not exist in reality. The antenna is positioned in the center of a sphere of surface $4\pi r^2$, where r is the radius of the sphere. The power flux density evaluated at the sphere shell is shown in Equation A.2.

$$p = \frac{P_0}{4\pi r^2} \quad (\text{W/m}^2) \tag{A.2}$$

Moreover, the radiation intensity of an isotropic source U_0 [81] is defined as the power propagated from an antenna per unit solid angle. A solid angle Ω is described as the ratio between a portion of area A and the square of its radius r^2 (see Figure A.3). In International System of Units (SI), Ω is measured in steradians sr . The mathematical derivation of the radiation intensity is given in Equation A.3.

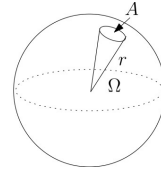


Figure A.3: Visualization of a solid angle. From [82].

$$U_0 = r^2 \cdot p = \frac{P_0}{4\pi} \quad (\text{W sr}^{-1}) \tag{A.3}$$

A.2.2 Gain

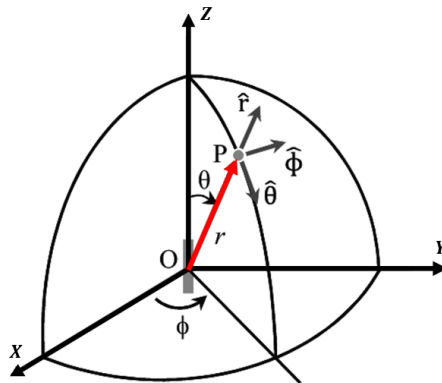


Figure A.4: Example of a dipole and spherical coordinates. Adapted from [83].

The gain of an antenna [81] is a fundamental parameter that characterizes its ability to direct or concentrate the radiated energy in a specific direction. It quantifies the efficiency of an antenna in converting the input power into radiated power in a particular direction. The gain is typically expressed in decibels (dB), which represent the radiation intensity U of the antenna in a given direction and the radiation intensity of an isotropic antenna U_0 .

Considering a certain antenna direction (θ, ϕ) in spherical coordinates (see Figure A.4), the gain is evaluated as follows:

$$G(\theta, \phi) = \frac{U(\theta, \phi)}{U_0} = \frac{U(\theta, \phi)}{P_0/4\pi} \tag{A.4}$$

Directivity [81] is another crucial aspect associated with antenna gain. It describes the ability of an antenna to concentrate or focus its radiated power towards a favourite direction, i.e. the direction of maximum transmissible power. A high directive antenna exhibits a narrow beamwidth, directing the majority of the energy in a specific direction (see Figure A.5). The directivity of an antenna is defined hereafter:

$$D = \frac{U_m}{U_0} = \frac{U(\theta_m, \phi_m)}{P_0/4\pi} \tag{A.5}$$

where (θ_m, ϕ_m) represents the direction in spherical coordinates of maximum power propagation and U_m is the maximum radiation intensity.

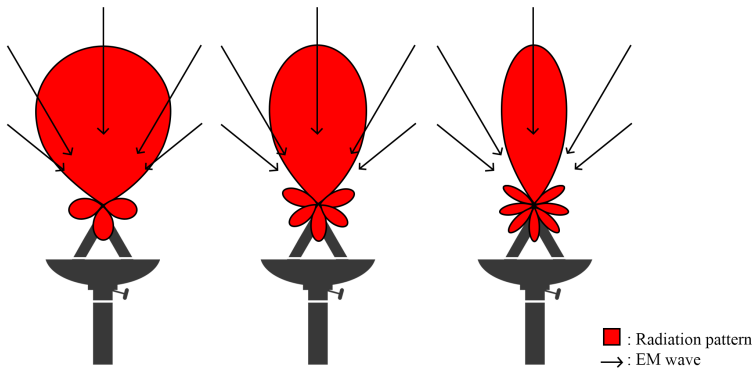


Figure A.5: Examples of different aperture lobes for the ground station and incident waves.

The radiation pattern of an antenna [81] visualizes how the radiated power is distributed in different directions. It represents the relative strength of the radiated

electromagnetic field as a function of direction. The radiation pattern is typically presented as a two-dimensional polar plot (see Figure A.6) or in spherical coordinates. It provides valuable insights into the coverage area, beamwidth, and directionality of an antenna's reception and transmission.

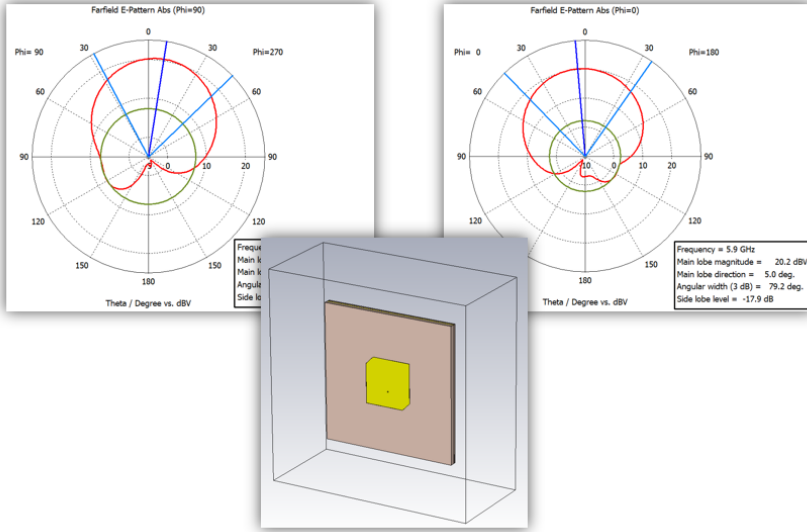


Figure A.6: Example of circularly polarized patch antenna radiation pattern. The simulation is performed with CST Studio Suite.

Due to the non-ideal nature of antennas, they are subject to losses caused by power dispersion in the materials. The parameter that measures these losses is called antenna efficiency η . The efficiency of an antenna refers to its ability to convert electrical power into radiated power. It represents the fraction of power applied to the antenna that is effectively radiated as electromagnetic waves. Efficiency is influenced by various factors, including the antenna design, material properties, and losses due to impedance mismatch, conductor resistance, dielectric losses, and environmental factors.

In order to define the antenna efficiency, it is important to introduce the aperture efficiency A_{eff} . The aperture efficiency is defined as the product between the antenna efficiency η and the physical area of the antenna aperture A :

$$A_{\text{eff}} = \eta \cdot A \quad (\text{A.6})$$

where the antenna efficiency usually ranges between 50% and 80%. Maximizing the power radiated by the transmitter through an increased η factor is crucial for a

good designer. The same applies to a receiving antenna.

A.3 Thermal noise

In communication systems, the presence of noise can significantly impact the quality and reliability of transmitted signals. The most common type is the thermal noise, also known as Additive White Gaussian Noise (AWGN). This Section explores the characteristics of thermal noise, its impact on communication systems and relevant concepts, for instance noise figure and Signal-to-Noise Ratio (SNR).

Thermal noise is generated by the thermal agitation of electrons within a conductor or resistive element. This phenomenon occurs in all electronic systems and is primarily influenced by the temperature of the system. As the temperature increases, the thermal noise power also increases.

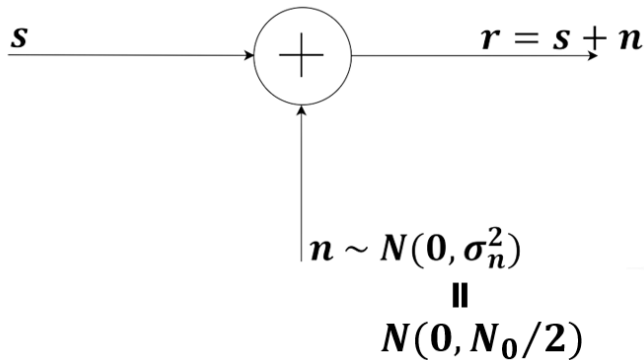


Figure A.7: AWGN.

Thermal noise possesses several key characteristics:

- *Additive*: the thermal noise is additive, meaning it can be superimposed on the desired signal without altering its characteristics. This property allows for straightforward mathematical analysis and enables the use of linear system theory;
- *White Noise*: the thermal noise is referred to as “white“ because it has a flat Power Spectral Density (PSD) across the entire frequency spectrum. This model implies that the noise power spectral density, indicated by the symbol N_0 , is evenly distributed across all frequencies;
- *Gaussian Distribution*: the thermal noise follows a Gaussian distribution, also known as a normal distribution. This means that the noise samples exhibit a

symmetrical bell-shaped curve, with the majority of samples clustered around the mean value.

A.3.1 Signal-to-Noise Ratio

The SNR is a crucial metric that determines the quality and reliability of a communication system. It represents the ratio of the power of a reference signal to the power of the thermal noise. A higher SNR signifies a stronger signal relative to the noise, resulting in improved system performance and enhanced reception of the transmitted information.

A.3.2 Noise Figure

The noise figure is a measure of the degradation of the SNR introduced by a particular component or system. It quantifies the additional noise the system contributed compared to an ideal noiseless system. A lower noise figure indicates better performance in terms of minimizing noise. By knowing the SNR at the input and output of a system, the noise factor can be easily obtained by the following formula:

$$NF = \frac{SNR_{in}}{SNR_{out}} \quad (\text{A.7})$$

A.4 Friis Transmission Equation

The *Friis Transmission Equation* (or simply *Friis formula*) [81] is a widely used equation in wireless communication systems to calculate the power received at a receiver antenna from a transmitter antenna. It takes into account the transmit power, antenna gains, and the distance between the transmitter and receiver. This Section provides an overview of the Friis formula and its significance in wireless communication.

The Friis formula calculates the received power P_R at the receiver antenna based on the following equation:

$$P_R = P_T + G_T + G_R - Loss_{FS} - L \quad (\text{dBm}) \quad (\text{A.8})$$

where:

- P_T is the transmitted power of by a radiator (i.e. the transmitter antenna);
- G_T is the gain of the transmitter antenna;

- G_T is the gain of the receiver antenna;
- $Loss_{FS}$ is the free-space path loss.
- L is the composite loss due to many factors, e.g. polarization mismatching, cable losses, connectors and atmospheric conditions.

The free-space path loss is expressed as follows:

$$Loss_{FS} = 20 \cdot \log \left(\frac{4\pi d}{\lambda} \right) \quad (dB) \quad (A.9)$$

where:

- λ is the wavelength of the signal.
- d is the distance between the transmitter and receiver.

Appendix **B**

Network Communication

In order to classify the different network protocols involved in the communication, a brief introduction to the so-called Open Systems Interconnection (OSI) model [84] is provided.

The OSI model, also known as the International Organization for Standardization (ISO)/OSI model, is a conceptual framework for understanding how different network protocols and technologies interact with each other. It was developed by the ISO in the 1979 and is still widely used.

The ISO/OSI model consists of seven layers (called OSI layers), responsible for a specific set of functions in the communication process (see table B.1). The layers are arranged in a hierarchical order, with each layer depending on the layer below for support and services. The first layer is the Physical layer, i.e. the closer layer to the transmission over a medium. The higher the layer position in the OSI model, the higher the abstraction level.

In table B.1 the OSI layers are shown with some examples of layer-specific functions.

Table B.1: ISO/OSI Model Layers.

#	Layer	Function
1	Physical	Transmission of data through a medium
2	Data Link	Framing, error detection and correction
3	Network	Addressing, routing
4	Transport	End-to-end communication, flow control
5	Session	Session management, synchronization
6	Presentation	Data representation, encryption, compression
7	Application	User-facing services

B.1 Cubesat Space Protocol

The Cubesat Space Protocol (CSP) [85] is a transport layer protocol that simplifies communication between embedded systems in smaller networks, like CubeSats. CSP has similar features to TCP/IP, but without the IP header overhead, allowing subsystems to offer services on the same network level without a master node. Each node has a unique CSP 32-bit address, facilitating communication between subsystems.

B.2 Controller Area Network

The Controller Area Network (CAN) [86] protocol is a serial communication protocol and standardized by ISO (standard: ISO-11898:2003). This protocol occupies both Physical and Data Link layers in the ISO model. CAN protocol is based on the Carrier-Sense Multiple-Access (CSMA) with Collision Detection and Arbitration on Message Priority (CD+AMP) mechanism. This means that each node on a bus must wait for a prescribed period of inactivity before attempting to send a message (CSMA). In case of collisions, they are resolved through a bit-wise arbitration based on a predetermined priority assigned to each message in the identifier field of the message (CD+AMP). Since every node on a bus takes part in this arbitration process, the CAN protocol provides a reliable and efficient means of communication between network devices.

B.3 Secure SHell

The Secure SHell (SSH) protocol [87] is a protocol for secure remote login, in order to assure data protection (in terms of privacy) towards insecure networks. It consists of three primary components. Firstly, the Transport Communication Protocol (TCP) ensures server authentication, confidentiality, and integrity, while also incorporating perfect forward secrecy. Secondly, the User Authentication Protocol validates the client's identity to the server. Lastly, the Connection Protocol is responsible for multiplexing the encrypted tunnel into multiple logical channels.

After establishing a secure transport layer connection, the client sends a service request, followed by another request upon successful user authentication. This facilitates the integration of new protocols alongside existing ones.

Furthermore, the connection protocol offers versatile channels that can serve various purposes. To this end, standard procedures are available for configuring secure interactive shell sessions, as well as forwarding (“tunneling”) arbitrary TCP/Internet Protocol (IP) ports and X11 connections. Figure B.1 shows an high-level view of

the SSH messages that are exchanged between client and server, in order to build a secure connection.

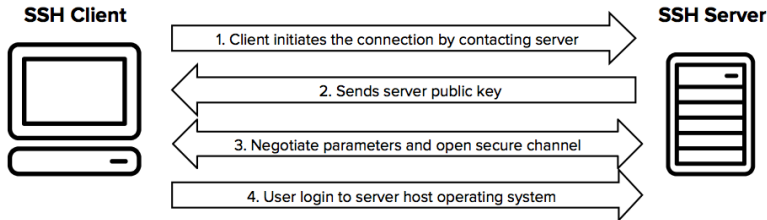


Figure B.1: High-level view of SSH message flow. From [88].

B.4 X11 Forwarding

X11 forwarding is a feature of the X Window System, a popular windowing system for Unix-like operating systems. It allows users to run graphical applications on a remote machine and display the application windows on their local machine.

When a user connects to a remote machine using SSH with X11 forwarding enabled, the graphical output of the application is sent to the user's local machine, where it is displayed using the local X11 server. This allows users to run graphical applications on remote servers, even if the remote machine does not have a graphical desktop environment installed.

Appendix

Matlab Simulator code

C.1 Transmitter entity

Below is shown the algorithm used to convert the binary file into a readable format for Matlab. Transmitter parameters such as Low Noise Amplifier (LNA) gain and Radio Frequency (RF) power value are included. See Section 4.5 for the description.

```
1 %% Read samples from binary file
2 ...
3
4 %% Apply PA gain value to the TX signal
5
6 TX_signal{1} = TX_signal_.*(db2mag(Prf_dBm)*db2mag(LNA_ampl_sat)*0.001)
   ; % for carrier frequency fc = fc_1
7 TX_signal{2} = TX_signal_.*(db2mag(Prf_dBm)*db2mag(LNA_ampl_sat)*0.001)
   ; % for carrier frequency fc = fc_2
```

Listing C.1: mainTX.m

C.2 Channel entities implementation

Main program used to handle each implemented channel entities. See Section 4.6 for the description.

```
1 % Compute satellite's speed
2 v_sat = sqrt(G_const*Me/(Re + h));
3
4 % for-loop for each the elevation angles
5 for elev = elev_ini:elev_step:elev_fin
6     i = (elev - elev_ini)/elev_step + 1;
7
8     % for-loop for each allocated carrier frequency
9     for k = 1:length(fcs)
10        [Y1,PLF1] = addFaradayRotation(TX_signal{k}, fcs(k), samp_rate,
11        TEC, Bav, sel_FR);
```

```

12     Y2 = addFreeSpaceLoss(Y1, fcs(k), elev, Re, h, c, sel_FSL);
13
14     Y3 = addDoppler(Y2, elev, elev_ini, phaseShift, v_sat, Re, h,
15     fcs(k), c, samp_rate, sel_D);
16
17     [Y4, real_cir{k,i}] = addStatMultipath(Y3, Gains, Delays,
18     n_tails, time_spacing, fDRichan, Kfact, samp_rate, c, Re, h, elev,
19     sel_M);
20
21     Y5 = addIonosphereScintillation(Y4, S4, Omega, Sigma, sel_IS);
22
23     Y6 = addNoise(Y5,SNR,sel_N);
24
25     RX_signal{k,i} = addAWGN(Y6,B,k_boltzman,Tsky_UHF,n,To,Ts,
26     L11_UHF,L12_UHF,NFlna_es,Glna_es,sel_AWGN);
27     end
28 end

```

Listing C.2: mainChannel.m

C.2.1 Thermal noise

Listing C.3 is used to add the amount thermal noise in function of the Signal-to-Noise Ratio (SNR) value passed inside the function. Listing C.4 shows the implementation of thermal noise in function of different parameters such as the bandwidth and the sky temperature. See Section 4.6.1 for the description of *addNoise.m* and *addAWGN.m*.

```

1 function Y = addNoise(X,SNR,sel)
2
3 if strcmp(sel,'on')
4     Pow_S = powerCalculator(X);
5     Pow_N = Pow_S/10.^((SNR)*0.1);
6
7     % Decision if complex noise is needed
8     if isreal(X)
9         N = sqrt(Pow_N)*randn(length(X),1);
10    else
11        N = sqrt(Pow_N/2)*(randn(length(X),1)+1i*randn(length(X),1));
12    end
13
14    N = N.'; % transpose
15
16    % Checking SNR
17    disp(['SNR passed = ',num2str(SNR),' dB']);
18    disp(['SNR calculated = ',num2str(snr(X,N)),' dB']);
19
20    % Output signal
21    Y = complex(X+N);
22 else
23    Y = X;
24 end

```



```
25
26 end
```

Listing C.3: addNoise.m

```
1 function Y = addAWGN(X,B,k_boltzman,Tsky_UHF,n,To,Ts,L11_UHF,L12_UHF,
2     NFlna_es,Glna_es,sel)
3 if strcmp(sel,'on')
4     % Antenna Noise Temperature
5     Ta_es_UHF = Tsky_UHF*n + To*2/3*(1-n) + Tsky_UHF*(1/3)*(1-n);
6
7     %% DOWNLINK (RX @ Ground Station)
8     Tm=(1.12*Ts)-50 ; % Enviroment Temperature [k]
9
10    %Composite temperature
11    Tcomp_es_UHF = Tm*(L11_UHF-1)+(Tm*(NFlna_es-1)/(1/L11_UHF))+(Tm*(
12    L12_UHF-1)/((1/L11_UHF)*Glna_es));
13
14    %System Temperature = Antenna temperature+Composite temperature
15    Tsys_DL_UHF = Ta_es_UHF + Tcomp_es_UHF;
16
17    %Compute noise power spectral density for DOWNLINK
18    N_0_DL_UHF = Tsys_DL_UHF * k_boltzman;
19
20    SNR_ev = mag2db(powerCalculator(X)/(N_0_DL_UHF * B));
21
22    Y = addNoise(X,SNR_ev,'on');
23 else
24     Y = X;
25 end
26 end
```

Listing C.4: addAWGN.m

C.2.2 Free-space path loss

The following code depicts the Matlab implementation present in the simulator for the generation of free-space path loss. See Section 4.6.2 for the description.

```
1 function [Y] = addFreeSpaceLoss(X,fc,e1,Re,h,c,sel)
2
3 if strcmp(sel,'on')
4     Beta = e1*pi/180 + asin((Re/(Re + h))*cos(e1*pi/180));
5
6     % Compute the distance between satellite and ground station
7     R = sqrt(Re^2 + (Re + h)^2 -2*Re*(Re + h)*sin(Beta));
8
9     % Compute the wavelength
10    lambda = c/fc;
11
```

```

12 % Free-space path loss
13 loss = (4*pi.*R./lambda).^2;
14 disp("Evaluated path-loss: " + string(mag2db(loss)) + " (dB)");
15
16 Y = X./loss;
17 else
18 Y = X;
19 end
20
21 end

```

Listing C.5: addFreeSpaceLoss.m

C.2.3 Doppler shift

The algorithm shows the code to generate the Doppler shift in function of different parameters, including carrier frequency and elevation angle. See Section 4.6.3 for the description.

```

1 function [Y] = addDoppler(X,el,el_min,phaseDev,v_tg,Re,h,fc,c,fs,sel)
2
3 if strcmp(sel,'on')
4     gamma_max = pi/2 - (deg2rad(el_min) + asin((Re/(Re + h))*cos(
5         deg2rad(el_min))));
6
7     % Compute the time instant of the satellite
8     t = ((Re + h)/v_tg) * (deg2rad(el) - deg2rad(el_min) + asin((Re/(Re
9         + h))*cos(deg2rad(el))) - asin((Re/(Re + h))*cos(deg2rad(el_min))
10        ));
11
12     omega = v_tg/(Re+h);
13
14     % Compute the Doppler shift
15     f_d = fc/c * (omega*Re*(Re + h)*sin(gamma_max - omega.*t))./(sqrt(
16         Re^2 + (Re + h)^2 -2*Re*(Re + h)*cos(gamma_max - omega.*t)));
17
18     % Apply the Doppler shift to the passed signal
19     Y = X.*exp(1i*(2*pi*f_d/fs*(0:length(X)-1) + deg2rad(phaseDev)));
20 else
21     Y=X;
22 end
23 end

```

Listing C.6: addDoppler.m

C.2.4 Multipath effect

The code is used to generate two distinct multipath effects: discrete and Rician-distributed. See Section 4.6.4 for the description.


```

44 %% CIR building
45 n_samples = length(X);
46 diracPulse = [1;zeros(n_samples-1,1)];
47
48 % Obtain the CIR by transmitting a Dirac delta over the channel
49 h = ricianChan(diracPulse);
50
51 Y = conv(X,h).';
52 else
53     Y=X;
54     h = zeros(1,round(max(delays)*fs) + 1);
55     h(1) = 1;
56 end
57
58 end

```

Listing C.7: addStatMultipath.m

C.2.5 Faraday rotation

The code is used to generate the Faraday rotation (FR), in function of the Total Electron Content (TEC) content, the sample rate, the carrier frequency and the average Earth's magnetic field. See Section 4.6.5 for the description.

```

1 function [Y,PLF] = addFaradayRotation(X,fc,fs,TEC,Bav, sel)
2
3 if strcmp(sel,'on')
4
5     [~,freq] = continuousFTsamples(X,1/fs);
6
7     const = 2.36e-14 * Bav * TEC;
8
9     theta = const ./ (((fc + freq)*1e-9).^2); % from Rec. ITU-R P
10    .531-14 (08/2019)
11
12    PLF = cos(theta).^2; % polarization loss factor for lin. pol.
13    antennas
14
15    [plf,~] = continuousIFTsamples(PLF, abs(freq(2) - freq(1)));
16
17    % Output signal
18    Y = conv(X,plf);
19 else
20     Y=X;
21     PLF=-1;
22 end

```

Listing C.8: addFaradayRotation.m

C.2.6 Ionospheric scintillation

Hereafter, the Matlab code used to generate ionospheric scintillation is depicted. The function takes several parameters as input to generate it, the most important of which is the value S_4 . See Section 4.6.6 for the description.

```

1 function [Y,h_ampl,h_phase] = addIonosphereScintillation(X, S4, Omega,
   Sigma, sel)
2
3 if strcmp(sel,'on')
4     h_ampl = nakagami_fading(length(X),1/S4^2,Omega); % m = (S4)^(-2)
   from Rec. ITU-R P.531-14
5     h_phase = exp(1i .* gaussian_phaseshift(length(X),Sigma));
6
7     h = h_ampl.*h_phase;
8
9     Y = X.*(h.');
```

```

10 else
11     Y=X;
12 end
13
14 end
15
16 % Gaussian zero-mean Channel Function
17 function h = gaussian_phaseshift(N,sigma)
18     h = random('normal', 0, sigma, [N 1]); % Generate random phase
   shift samples
19 end
20
21 % Nakagami Fading Channel Function
22 function h = nakagami_fading(N, m, Omega)
23     pd = makedist('Nakagami','mu',m,'omega',Omega);
24     h = random(pd,N,1);
25 end
```

Listing C.9: addIonosphereScintillation.m

C.3 Validation process implementation

In this Section, each Matlab code used for the validation process discussed in Section 4.7 is reported.

C.3.1 Doppler estimation and compensation

The code for estimating and compensating the Doppler shift is detailed hereafter. It implements a convolutional method as described in Section 4.7.1.

```

1 function [RX_signal_nofD, fD_shift] = dopplerEstComp(X,samp_rate)
2     [RX_FFT,f_RX] = continuousFTsamples(X,1/samp_rate);
3
```

```

4   conv_RRX = conv(RX_FFT,RX_FFT,'same'); % to use same x-axis of
RX_FFT (f_RX)
5   [~,max_id] = max(conv_RRX);
6   fD_shift = f_RX(max_id)/2;
7
8   RX_signal_nofD = X.*(exp(-1i*(2*pi*fD_shift/samp_rate*(0:length(X)
-1))));
9 end

```

Listing C.10: dopplerEstimation.m

C.3.2 Cross-correlation for the channel sounding technique

The following code is used to perform the cross-correlation for the channel sounder. The code needs only the received signal \mathbf{Y} and the reference signal `ref_signal`. See Section 4.7.2 for the description.

```

1 function [cir_equ,lag] = ChannelSounder(Y,ref_signal,Threshold)
2
3 [c_func, lag] = crossCorrelation(ref_signal,Y,'on');
4
5 c_func(c_func < Threshold) = 0;
6 cir_equ = c_func./max(c_func);
7
8 cir_equ = flip(cir_equ);
9 cir_equ = cir_equ(round(length(cir_equ)/2):end);
10 lag = lag(round(length(lag)/2):end);
11
12 end

```

Listing C.11: ChannelSounder.m

C.3.3 S_4 parameter computation

The algorithm is used to estimate the S_4 parameter. The function uses a window method to see the convergence of the estimated parameter. See Section 4.7.3 for the description.

```

1 function S4_obtained = S4_function(N,x)
2   S4_obtained = zeros(1,N);
3
4   % S4 parameter is computed with different windows (1 --> N)
5   for i=1:N
6     numerator = abs(mean((x(1:(32640*i)).*conj(x(1:(32640*i))))
.^2) - (mean(x(1:(32640*i)).*conj(x(1:(32640*i))))).^2);
7     denominator = (mean(x(1:(32640*i)).*conj(x(1:(32640*i))))).^2;
8     S4_obtained(i) = sqrt(numerator ./ denominator);
9   end
10 end

```

Listing C.12: S4_function.m

Appendix **D**

Connection configuration

In this Chapter, two main topics are covered: communication between users and Software Defined Radio (SDR)s and the Docker container implementation to create and test radio applications.

D.1 TOTEM SDR connection

In order to establish the connection between the user and TOTEM SDR, the Secure SHell (SSH) protocol is used.

Before proceeding to the connection, the SDR must be powered up by using the `hypso-cli`. `hypso-cli` is the Command Line Interface (CLI) made by the SmallSat Lab utilized for transmitting commands using Cubesat Space Protocol (CSP) packets. These commands are sent from the mission operator to the FlatSat bus and further directed to the payload subsystem [89]. `hypso-cli` resides inside LidSat, since it is the main workstation capable to communicate over Controller Area Network (CAN) bus. Figure D.1 shows how `hypso-cli` appears to the end user.

```
giacomo@lidsat:~$ cd HYPSO2/shortcuts/ && sudo ./hypso-cli
[sudo] password for giacomo:
Logging output to: 230619T071406_hypso-cli.log
Hostname:  smallsatlab
Model:     hypso-cli
Revision:  Oct 11 2022
Git commit: 9dc29a5-373-1.4.0-dirty
Git branch: master
Type list to see commands.
Type help <command> for specific help.
(hypso-cli-CAN)
```

Figure D.1: Bash output after running `hypso-cli`.

In order to power up the SDR, the following instruction is used:

```
(hypso-cli-CAN) shell remote oneshot 4 5 output 6 1 0
```

Listing D.1: Bash instruction to power up TOTEM SDR in FlatSat.

where:

- **Oneshot:** run the command and return to the *hypso-cli* interface;
- **4:** ID of Energy Power Supply (EPS) (see Figure D.2);
- **5:** timeout in seconds;
- **6:** the power line connected to the TOTEM SDR;
- **1:** to power up the SDR (0 to power down).

To verify that the TOTEM SDR is powered up, the CSP instruction depicted in Listing D.2 is used, where 13 is the ID of the TOTEM SDR in the CAN line (see Figure D.2).

```
(hypso-cli-CAN) csp ping 13
```

Listing D.2: Bash instruction to ping TOTEM SDR in FlatSat. The CSP protocol is used to interact with the device.

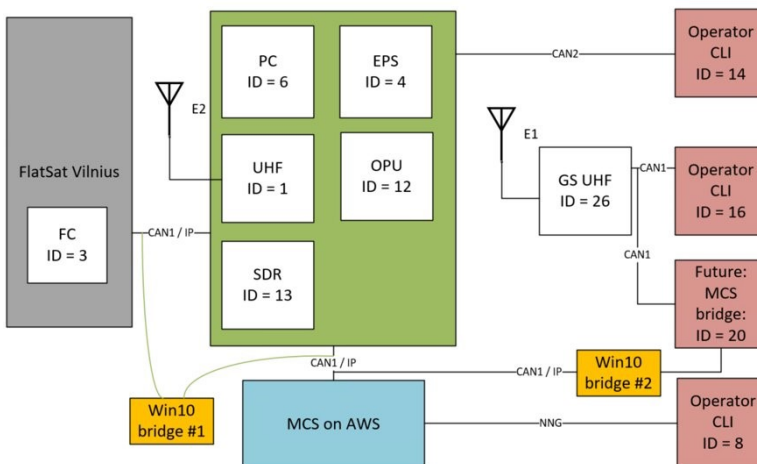


Figure D.2: Flatsat connection setup. From [90].

D.2 USRP-2901 connection

The Universal Software Radio Peripheral (USRP)-2901 is equipped with just a Universal Serial Bus (USB) interface, as mentioned in Section 3.3.2. Figure 5.1 shows how the USRP-2901 is deployed inside the testbed.

After establishing the SSH connection between user and workstation, it becomes necessary to determine the device address in order to communicate with the SDR, by running the following code:

```
uhd_find_devices
```

Listing D.3: Command line to find the device address of the USRP-2901.

An example of output is shown in Figure D.3.

```
root@gnuradio-totem:~# uhd_find_devices
[INFO] [UHD] linux; GNU C++ version 9.2.1 20200304; Boost_107100; UHD_3.15.0.0-2build5
-----
-- UHD Device 0
-----
Device Address:
  serial: 30DBBF9
  name: USRP_12
  product: B210
  type: b200
```

Figure D.3: Output example of `uhd_find_devices` instruction.

D.3 GNU Radio Companion Docker container

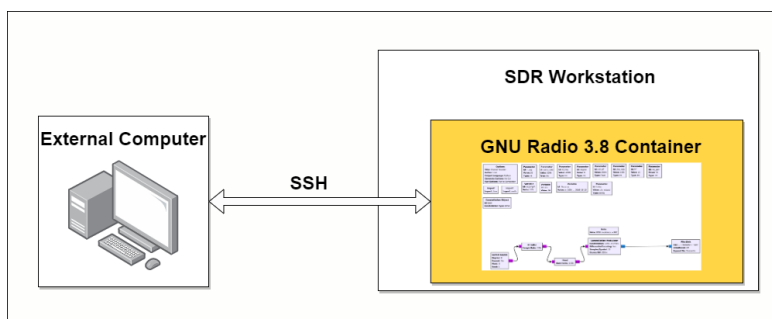


Figure D.4: High level connection scheme between the user and GNU Radio Companion.

GNU Radio Companion (see Section 3.3) is the software used to make radio applications for the SDRs of the testbed. A Docker container instance is created to run the software without minding the operative system on which it relies.

To ensure the successful execution of GNU Radio Companion 3.8 within the Docker container, Alén Space provides a Dockerfile that is crafted and tailored to meet the requirements set by the SmallSat Lab. Moreover, a shell script is created to build and run the Docker container.

D.3.1 Build and run of the Docker container

Figure D.4 depicts the logical connection between the user (identified as External Computer) and the container. The SDR workstation is used as Proxy server between the local machine and the container. The shell script responsible to build and run the Docker container is shown in D.4.

```

1 xhost +
2 docker run -d -p 2022:22 --rm -it --privileged \
3   --volume "$HOME/.Xauthority:/home/.Xauthority:rw"
4   \
5   --volume
6   "$(pwd)/docker/gr-workdir:/home/gnuradio/workdir/" \
7   --device /dev/dri:/dev/dri \
8   --device /dev/bus/usb:/dev/bus/usb \
9   --device /dev/ttyUSB0 \
10  --volume /dev/shm:/dev/shm \
11  --volume /tmp/.X11-unix:/tmp/.X11-unix:ro \
12  --volume /run/user/$(id -u)/pulse:/run/pulse:ro \
13  --volume /var/lib/dbus:/var/lib/dbus \
14  --volume /dev/snd:/dev/snd \
15  --env USER_UID=$(id -u) \
16  --env USER_GID=$(id -g) \
17  --env DISPLAY=unix$DISPLAY \
18  --hostname gnuradio-totem \
19  gnuradio-totem $@
20 ID_GNURADIO_DOCKER=$(docker container ls | grep
   'gnuradio-totem' | awk '{print $1}')
21 docker exec -it ${ID_GNURADIO_DOCKER} service ssh start

```

Listing D.4: Part of *gnuradio-docker_ubuntu.sh*.

Firstly, `xhost +` (line 1) command is used to grant permission to any remote client to display the Graphical User Interface (GUI) on the local X server. In this case, the local machine of the user is the aforementioned server. This is used to enable the X11 and show the graphical interface of GNU Radio Companion.

Line 2 is used to implement different features, including enabling the container in detached mode (`-d` [91]) and port mapping configuration (`-p 2022:22`: mapping between port 2022 of the workstation and 22 of the container). The rest of the instructions are used to allow the container accesses the hardware devices (`-device` [92]), to mount directories inside the container (`-volume` [93]) and stating the SSH service inside the container (line 20).

D.3.2 SDR workstation configuration

The second step is to configure the SDR workstation and the *config* file under the *.ssh/* folder. The configuration is shown in D.5.

```

1 Host gnuradio_container
2     Hostname localhost
3     Port 2022
4     user root
5     ForwardX11 yes
6     ForwardX11Trusted yes

```

Listing D.5: config file content in SDR workstation.

Each entry is explained hereafter:

- `Host gnuradio_container`: it indicates the name of the Docker container;
- `Hostname localhost`: it specifies the hostname or network address used to access the container;
- `Port 2022`: it indicates that port 2022 is being used to communicate with the container;
- `User root`: it specifies the user account;
- `ForwardX11 yes`: it enables X11 forwarding;
- `ForwardX11Trusted yes`: it sets the X11 forwarding to be trusted, indicating that the container is trusted to display its graphical user interface on the host machine.

D.3.3 Local machine configuration

The final step is to configure the local machine to enable the SSH connection with the container. First of all, a SSH key is created by running the usual instruction `ssh-keygen`. After that, the public key is included inside the *authorized_keys* file both in the SDR workstation and the container, by running the following instruction:

```
1 echo "<your_public_key_string>" >> ~/.ssh/authorized_keys
```

Listing D.6: Instruction to write the public key into the *authorized_keys* file.

Currently, establishing a SSH connection with an external computer from the container is not feasible. However, it is possible to gain access to the container by executing the following command, as shown in Listing D.7, within the SDR workstation. This code provides access to the Docker container in detached mode.

```
sudo docker exec -e DISPLAY=$DISPLAY -it $(sudo docker
  container ls | grep 'gnuradio-totem' | awk '{print
    $1}') /bin/bash
```

Listing D.7: Instruction to access the Docker container in detached mode without SSH.

Moreover, Listing D.8 shows the content of the *config* file in my local machine to set the aliases for both SSH workstation and the Docker container.

```
Host gara # shortcut to ssh SDR workstation
  HostName 129.241.2.62
  User gara
  IdentityFile ~/.ssh/<pub_key_id>
Host gnuradio_gara # proxy ssh to Docker container
  HostName 127.0.0.1
  User root
  IdentityFile ~/.ssh/<pub_key_id>
  Port 2022
ProxyJump gara # to proxy SDR workstation
```

Listing D.8: Example of config file in a local machine.

Finally, the instruction used to establish the connection with the Docker container via Proxy is depicted in Listing D.9, where *gnuradio_gara* is the SSH alias chosen for the local machine.

```
ssh -X gnuradio_gara
```

Listing D.9: Example of SSH connection to the Docker container with X11 forwarding enabled.



 **NTNU**

Norwegian University of
Science and Technology